

# Mechanics of Airflow in Human Inhalation

Alister J. Bates

Imperial College London

Department of Aeronautics

This thesis is submitted for the degree of Doctor of Philosophy

2014

# Abstract

The mechanics of airflow in the large airways during inspiration affects important physiological functions such as ventilation, olfaction, heat exchange and mass transfer. The behaviour of the airflow is important not only for healthcare applications including diagnosis, intervention planning and assessment, but for inhalation toxicology.

This research aims to further the understanding of human nasal physiology through computational modelling. Specifically, the effects of transient inhalation conditions on flow dynamics and transport were characterised and the changes in flow behaviour in response to certain pathologies quantified. The key findings can be summarised as follows:

Firstly, the time scales for airflow in the large airways have been identified and the initial flow patterns revealed. Three phases in the temporal behaviour of the flow were identified (flow initiation, quasi-equilibrium and decay). The duration of each phase differs depending on the quantity of interest.

Flow in the nose was characterised as transitional, whilst in parts of the descending airways it is turbulent, particularly in the faster moving regions around the jets which may occur in the pharynx, larynx and at the superior end of the trachea.

The bulk of the flow is biased to fill only certain regions of the airways, whilst other regions carry little flow, due to features upstream. Analysis of cross-sectional images provided by medical imaging does not necessarily provide a representative view of the area available to the flow.

Various scalar species were employed to represent the fate of nanoparticles and gaseous species within the airways. Only species with high diffusion rates exhibited significant absorption at the airway walls.

Airway pathologies often cause changes to the geometry of the airway. One such pathology, the goitre, was found to curve the trachea and in some cases cause constriction. Both these geometric changes were found to increase the pressure loss and energy required to drive flow through the trachea. Furthermore, the flow in pathological cases was more disturbed.

High resolution simulations have been used to address these topics and the scales simulated have been analysed in terms of the smallest features possible in the flow to determine their fidelity.

# Declaration

This is to certify that the work presented in this thesis has been carried out at Imperial College London and has not been previously submitted to any other university or technical institution for a degree or award. The thesis comprises only my original work. Due acknowledgement is specifically made where appropriate.

---

Alister Bates

## Copyright Declaration

The copyright of this thesis rests with the author and is made available under a Creative Commons Attribution Non-Commercial No Derivatives licence. Researchers are free to copy, distribute or transmit the thesis on the condition that they attribute it, that they do not use it for commercial purposes and that they do not alter, transform or build upon it. For any reuse or redistribution, researchers must make clear to others the licence terms of this work.

## Acknowledgements

The completion of this thesis and my PhD is due to the help and support of a number of colleagues, friends and family. Firstly, I would like to thank my supervisor, Professor Denis Doorly for his guidance throughout this work, as well as for helping me make the transition from industry to academia. Professor Bob Schroter has also provided invaluable advice, especially on physiology. Raul Cetto has performed the medical side of this work and given me much of my understanding of the airways. Collaboration with him has been invaluable throughout this work and he has also sourced and segmented most of the geometries considered here. Andrew Comerford provided much insight and advice, especially on the section of this work concerning tracheas. Some of the research presented here has been done as part of a collaboration with the Barcelona Supercomputing Center and I would particularly like to thank Alberto Gambaruto, Hadrien Calmet and Guillaume Houzeaux for their assistance and suggestions throughout that work. My parents and sister have provided much advice on dealing with the tribulations of obtaining a PhD and finally, I must thank Claire, who has put up with me throughout.

This research was funded by EPSRC doctoral training award EP/P505550/1.

# Contents

<b>1</b>	<b>Introduction</b>	<b>15</b>
1.1	Functions of the Airways . . . . .	15
1.2	Airway Anatomy . . . . .	15
1.3	Previous Investigations . . . . .	19
1.3.1	Flow in the Nasal Cavities . . . . .	19
1.3.2	Flow in the Descending Airways . . . . .	20
1.3.3	Modelling and Quantifying Transient Effects . . . . .	22
1.3.4	Modelling the Inhalation of Nanoparticles . . . . .	25
1.4	Motivation . . . . .	28
1.5	Journal and Conference Papers . . . . .	29
<b>2</b>	<b>Methods</b>	<b>31</b>
2.1	Geometry Capture . . . . .	31
2.2	Meshing . . . . .	32
2.3	Numerical Simulation . . . . .	33
2.4	Particle Motion . . . . .	36
2.5	Boundary conditions applied to the simulations . . . . .	36
2.5.1	Flow inlets and outlets . . . . .	36
2.5.2	Flow-wall interactions . . . . .	37
2.5.3	Particle-wall interactions . . . . .	37
2.6	Flow Metrics . . . . .	38
2.6.1	Temporal Means and Variances . . . . .	38
2.6.2	Non-dimensional Numbers . . . . .	39
2.6.3	Vorticity, Wall Shear Stress and Turbulence Intensity . . . . .	41
2.6.4	Utilised Area . . . . .	42
2.6.5	Energy Flux . . . . .	42

2.6.6	Scalar Quantities . . . . .	43
2.6.7	Vortex Identification . . . . .	43
2.6.8	Turbulent Quantities and Spectra . . . . .	44
2.7	Geometric Analysis . . . . .	46
<b>3</b>	<b>Convergence and Accuracy Evaluation</b>	<b>51</b>
3.1	Converging the Simulation . . . . .	51
3.1.1	Residuals . . . . .	51
3.1.2	Spatial and Temporal Resolution . . . . .	52
3.2	Quantifying the Captured Scales . . . . .	56
3.3	Validation of Simulations by Experimental Comparison . . . . .	60
<b>4</b>	<b>Dynamics of a Rapid Inhalation</b>	<b>63</b>
4.1	Specific Anatomy . . . . .	63
4.2	Boundary Conditions . . . . .	65
4.3	Mesh Analysis . . . . .	67
4.4	Flow Development . . . . .	69
4.5	Flow Metrics . . . . .	72
4.6	Patterns of Flow: Nasal Flow Division . . . . .	75
4.7	Patterns of Flow: Unsteadiness and Turbulence . . . . .	78
4.8	Reduced Resolution Simulation . . . . .	91
4.9	Summary . . . . .	91
<b>5</b>	<b>Transport in a Rapid Inhalation</b>	<b>93</b>
5.1	Transport by the Flow of a Low Diffusion Inhaled Scalar . . . . .	94
5.2	The Effect of Diffusivity and Absorption on Scalar Transport . . . . .	101
5.3	Absorption at the Wall . . . . .	111
5.4	Summary . . . . .	118

<b>6</b>	<b>Characterisation of Airflow in Pathological Tracheas</b>	<b>120</b>
6.1	Specific Geometry Capture . . . . .	120
6.2	Geometry Analysis . . . . .	121
6.3	Flow Patterns . . . . .	126
6.4	Flow Metrics . . . . .	134
6.5	Turbulence & Unsteadiness . . . . .	139
6.6	Summary . . . . .	142
<b>7</b>	<b>Conclusions</b>	<b>145</b>
	<b>References</b>	<b>150</b>
<b>A</b>	<b>Geometric Values of Considered Airways</b>	<b>161</b>
<b>B</b>	<b>The Utilised Area Ratios of Analytic Flows</b>	<b>161</b>
<b>C</b>	<b>Resolution of Scalar Boundary Layers</b>	<b>163</b>

# List of Figures

1.1	Anatomy of the nasal cavity. . . . .	16
1.2	Anatomy of the descending airways. . . . .	18
2.1	Example segmentation of a trachea, larynx and pharynx. . . . .	32
2.2	The utilised area. . . . .	42
2.3	The ranges of an idealised turbulent spectrum. . . . .	45
2.4	Stages in intersecting a plane with an STL surface. . . . .	48
2.5	Slices through an airway geometry. . . . .	48
2.6	One slice through a trachea, compared to the original CT image. . . . .	49
3.1	Comparison of results from different solution resolutions and modelling. . . . .	53
3.2	Comparison of mean and the variance of velocity. . . . .	55
3.3	Comparison of fluctuating velocity spectra. . . . .	56
3.4	Viscous dissipation rates and Kolmogorov length scales. . . . .	57
3.5	Details of the “production” mesh structure. . . . .	58
3.6	Vorticity in the pharynx at five instants. . . . .	59
3.7	Photograph of a rapid prototyped trachea with pressure taps. . . . .	61
3.8	Comparison of experimental and CFD simulated pressure loss. . . . .	62
4.1	Segmented airway anatomy. . . . .	63
4.2	Geometry used for sniff study with area variation and planes marked. . . . .	65
4.3	Positions of sagittal planes. . . . .	66
4.4	Comparison of inlet boundary conditions. . . . .	67
4.5	Instantaneous and cumulative volumetric flow. . . . .	68
4.6	Cross-sections through mesh. . . . .	69
4.7	Division of volumetric flow rate between nostrils. . . . .	70
4.8	Velocity contours at succeeding instants. . . . .	71
4.9	Volume renderings of instantaneous velocity field. . . . .	72

4.10	Pressure loss and resistance during a sniff. . . . .	73
4.11	Energy fluxes through planes during a sniff. . . . .	74
4.12	The total energy loss between each pair of consecutive planes over the duration of the sniff. . . . .	75
4.13	Mass flow distribution between different regions. . . . .	77
4.14	Area distribution of regions used to analyse mass flow. . . . .	77
4.15	Point velocity signals. . . . .	78
4.16	Mean and fluctuating velocities in the nose. . . . .	79
4.17	Structures of $\lambda_2$ in both nasal cavities. . . . .	80
4.18	Mean and fluctuating velocities on sagittal planes in the nose and axial planes in supraglottic region. . . . .	81
4.19	Mean and fluctuating velocities on sagittal planes in the pharynx and larynx. . . . .	82
4.20	Vorticity in the nose, pharynx and larynx. . . . .	84
4.21	Volume renderings of instantaneous $\lambda_2$ and velocity. . . . .	85
4.22	Instantaneous vorticity and velocity perturbations in the pharynx and larynx. . . . .	86
4.23	Fluctuating velocity components. . . . .	87
4.24	Mean of the magnitude of velocity and the mean of the fluctuating magnitude of velocity. . . . .	87
4.25	Spectra of fluctuating velocity. . . . .	89
4.26	Surface of spectra. . . . .	90
4.27	Low frequency region of spectra. . . . .	90
5.1	Initial scalar distribution. . . . .	94
5.2	Concentration of scalar inhaled through the nostrils. . . . .	95
5.3	Scalar distribution at successive instants. . . . .	96
5.4	Distribution of scalar species on lower axial plane. . . . .	97
5.5	Instantaneous scalar distribution in the nose. . . . .	98

5.6	Volume renderings of scalar concentration. . . . .	99
5.7	Scalar flux through planes. . . . .	100
5.8	Upper regions of the nasal cavities. . . . .	101
5.9	Scalar build up and decay in upper region of the nose. . . . .	102
5.10	Comparison of scalar flux through planes. . . . .	104
5.11	Comparison of scalar fluxes through the nostril and the carina. . . . .	105
5.12	Comparison of cumulative scalar flux through planes. . . . .	106
5.13	Proportion of scalar absorbed in each region. . . . .	107
5.14	Volumetric saturation of the superior part of the nasal cavity. . . . .	108
5.15	Instantaneous contours of scalar flux normal to the upper axial plane. . . . .	109
5.16	Comparison of scalar fluxes and mechanisms. . . . .	110
5.17	The flux of scalar D through the nasal wall. . . . .	112
5.18	The flux of scalar C through the nasal wall. . . . .	113
5.19	Wall shear stress on the nasal wall. . . . .	114
5.20	Concentration profiles of scalars A-D and the velocity profile in the nose. . . . .	115
5.21	Concentration profiles of scalars A-D and the velocity profile in the glottis. . . . .	116
5.22	Surface fluxes of scalars C and D at the airway wall. . . . .	117
6.1	Sagittal and coronal views of tracheal geometries. . . . .	122
6.2	Frenet normal vectors along the centrelines. . . . .	124
6.3	Area variation along the tracheas. . . . .	125
6.4	Cross-sectional roundness along the length of the tracheas. . . . .	126
6.5	Volume renderings of mean and instantaneous velocities. . . . .	129
6.6	Cross sectional mean Reynolds and Dean numbers. . . . .	130
6.7	Contours of static pressure and velocity on cross-sections through geometry B. . . . .	131
6.8	Contours of static pressure and velocity on cross-sections through geometry E. . . . .	133

6.9	Utilised area ratios along the lengths of tracheas A, B and E . . . . .	134
6.10	Energy flux through the tracheas. . . . .	136
6.11	Pressure losses through the tracheas. . . . .	137
6.12	Total pressure loss along the length of the trachea. . . . .	139
6.13	Volume renderings of the variance of velocity. . . . .	141
6.14	Structures of $\lambda_2$ in geometries A, B and E. . . . .	142
C.1	Section of the images shown in figure 5.16. . . . .	163

## List of Tables

3.1	Simulation parameters used in convergence study. . . . .	53
3.2	Comparison of pressure loss ( $\Delta P$ ) values for the seven simulations listed in table 3.1 and shown in figure 3.1. . . . .	54
3.3	Refinement statistics between the finest mesh simulated, a showing comparison between mesh length scales and the time step and the smallest features in the flow. . . . .	58
4.1	Velocity and turbulence values on planes. . . . .	83
5.1	Properties of considered scalar species. . . . .	103
6.1	Mean and extreme geometric statistics for the considered tracheal geometries. . . . .	123
6.2	Constriction length percentages. . . . .	127
6.3	Exponents of pressure flow relationships for all geometries on which simulations were performed. . . . .	136
6.4	Tracheal resistances. . . . .	137
A.1	Geometric values for a large airway anatomy. . . . .	161
B.1	Comparison of utilised area ratios for several analytical flow profiles. . .	162

# List of Abbreviations and Symbols

3D - 3 dimensional

$\alpha$  - Womersley number

CCM - Computational continuum mechanics

COPD - Chronic obstructive pulmonary disease

CFD - Computational fluid dynamics

CT - Computed tomography

De - Dean number

DNS - Direct numerical simulation

ENT - Ear, nose and throat

LES - Large eddy simulation

MRI - Magnetic resonance imaging

Pe - Péclet number

RANS - Reynolds averaged Navier-Stokes

Re - Reynolds number

SAVR - Surface area to volume ratio

Sc - Schmidt number

St - Strouhal number

Stk - Stokes number

STL - Stereolithography (file format)

UA - Utilised area

VMTK - Vascular modelling toolkit (software)

# 1 Introduction

The purpose of this chapter is to introduce the anatomy and physiological functions of the human body which are investigated. Firstly, an overview of the physiology of the large airways (the nose to the carina) is presented, to highlight the functions of interest in an inhalation. The anatomy of the nose and descending airways (pharynxes, larynx and trachea) is briefly described, focussing on the anatomical references used throughout this thesis when describing the locations of features in the flow.

The current state of the art of modelling and describing air flow in the nasal cavities and the descending airways is presented, with specific focus on transient and particle laden simulations and experiments. This literature review leads to the motivations for the current work.

## 1.1 Functions of the Airways

The human airways' primary function is to act as the conduits for breathing. The nose is the primary respiratory opening to the environment, however it has a similar resistance to flow as the mouth [16, 119]. The nose performs several additional functions to protect the delicate respiratory organs downstream; the air is warmed to body temperature, humidified to over 90% [50, 96] and almost all inhaled particles from the size of flies to 5  $\mu\text{m}$  are filtered out, whilst 50% of those between 2 and 4  $\mu\text{m}$  are removed [121]. Furthermore, the air is sampled for olfaction, providing information about the outside environment.

The pattern of inhalation and exhalation changes with the various requirements of the above functions. As the respiratory rate increases, so the flow rate of air to be carried, heated, humidified, filtered and sampled goes up, whilst breath profiles for olfaction are short and fluctuating [91].

## 1.2 Airway Anatomy

The nasal airways open to the outside air at the downward facing nostrils and turn the inrushing air through 180° to enter the descending airway at the nasopharynx. After the external nostrils, the air traverses a small vestibule before reaching the second constriction; the nasal valve, often assumed to be the narrowest section of the airways

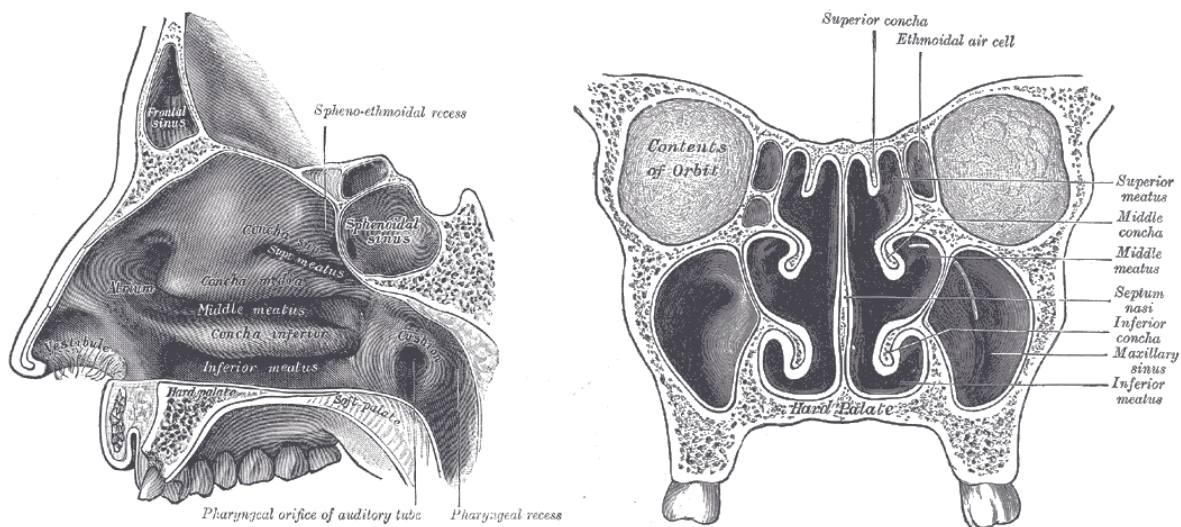


Figure 1.1: Anatomy of the nasal cavity. Sagittal (left) and coronal (right) views of the nasal cavity highlighting the protruding structures known as “turbinates” or “concha” as labelled in the image and the passageways around them, known as meatus. Images taken from Gray’s Anatomy [62], plates 855 and 859 (Copyright expired).

[49, 88]. The nose remains divided into two cavities by the septum which ends at the nasopharynx. Three structures protrude into the nasal airspace on each side; the superior, middle and inferior turbinates. These are largely comprised of mucosal tissue, which is erectile in nature and allows the calibre of the nasal airway to vary. This variation is performed regularly in healthy humans, about 80% of whom alternately congest their nasal cavities, altering which side of the nose is more patent throughout the day [27]. This process is known as the nasal cycle.

Mucosal tissue lines much of the nose, allowing some degree of erectile behaviour throughout. Secretory cells provide the serous fluid to humidify the air, whilst the underlying capillary beds provide a heat flux to the region. Olfactory receptors are most densely located in the superior regions of the nasal cavity, although are found throughout the nose [34].

The descending airways (figure 1.2) consist of the pharynx, larynx, trachea and bronchi before entering the smaller airways which are outside the scope of this work. The pharynx itself can be further divided into the nasopharynx at the back of the nose, the oropharynx posterior to the mouth and the laryngopharynx. This latter section includes the hypopharynx where the airway and digestive paths diverge.

In the pharynx, the airway lumen can be affected by the surrounding soft tissue, as

many of the structures are non-rigid. The soft palate, back of the tongue, epiglottis and vocal chords in the larynx can all change position, affecting airway patency [83], whilst the position of the head in relation to the body will also change the airway's shape.

The trachea is formed of rings of cartilage, of which only the first is a complete ring, whilst subsequent ones are open at the back. The posterior section in the opening of these C-shaped rings is made up of fibrous tissue which is non-rigid.

Various pathologies can affect the functions of the airways, increasing the work necessary to breathe, or to limit the air conditioning capabilities, leading to lower airway damage. Of particular interest to the current study are those conditions that cause breathing difficulties through changes to the airway geometry that alter the physics of the flow. Retrosternal goitres are an example of such a pathology: goitres are enlargements of the thyroid gland which can press on the airways, extrinsically compressing them. Other forms of airway narrowing or stenoses are termed intrinsic and may be caused by inflammation or granulation of the tracheal lining.

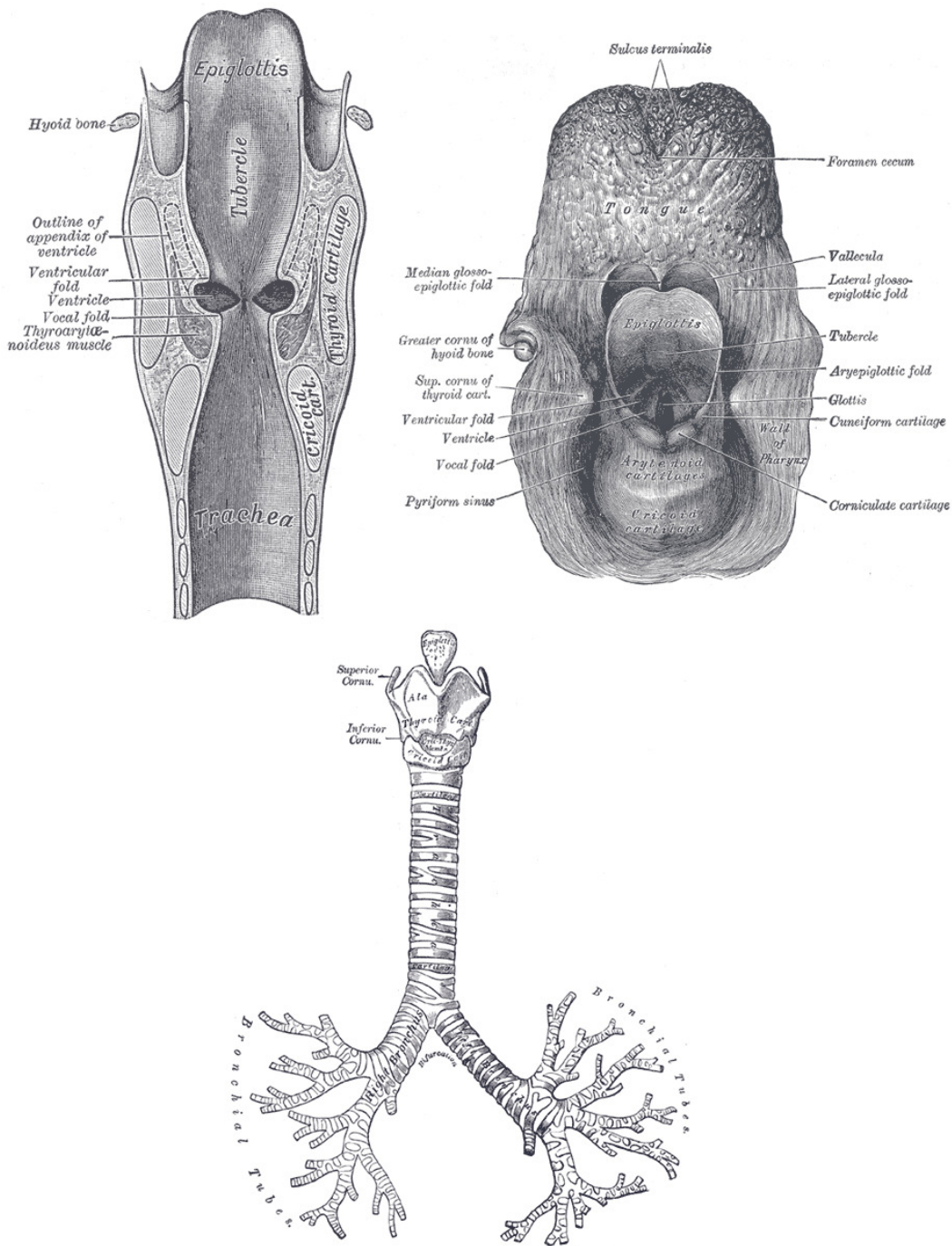


Figure 1.2: Anatomy of the descending airways. Top left: Coronal cross section through the larynx, highlighting the constriction at the glottis before expansion into the trachea. Top right: structures present in the laryngopharyngeal region, including the back of the tongue and epiglottis. Bottom: The outside of the pharynx, trachea and early bronchial branches. Images taken from Gray's Anatomy [62], plates 954, 955 and 961 (Copyright expired).

## 1.3 Previous Investigations

An overview of computational fluid dynamics simulation in the human airways is provided by Tu et al. [115], with a focus on particle deposition. All stages of the process from medical imaging and segmentation to numerical methods and boundary conditions are briefly covered. A further overview of the process can be found in Bailie et al. [2], who found CFD simulations of respiratory flow to provide clinically useful insight in cases of nasal obstruction.

The following sections explore the current state of the art in respiratory airflow modelling, focusing on four areas of particular relevance to this work; flow in the nasal cavities, flow in the descending airways, the modelling of unsteadiness and the transport of nanoparticles within the airways.

### 1.3.1 Flow in the Nasal Cavities

Although healthy human airways are broadly similar, regional patterns of flow differ according to subject geometry, as shown in many studies [132, 63, 128], though the complex anatomy makes exploring the relation using analytic descriptions [32] difficult. The temporal dynamics also affect the flow behaviour, as shown for example by the experimental studies of Chung and Kim [14].

Previous studies have been constrained by the available technology, limiting airflow models to steady flow [52, 53], or to allow only slow temporal variations [103]. Subsequent improvements in computing and imaging facilitated study of flow initiation in a unilateral nasal model [24], with continuous PIV measurements obtained at an effective rate of 15,000 frames per second validating direct numerical simulations (DNS). In the latter study, the development of a prominent flow recirculation in the anterior portion of the nasal cavity was mapped as was the instability of the shear layer at the margins of the jet issuing from the nasal valve. However that work only explored the initiation phase in detail and considered a unilateral model.

Ishikawa et al. [45] simulated a sniff flow rate of around  $800 \text{ mls}^{-1}$  in one nasal cavity, but simulations were performed at a relatively coarse numerical resolution, whilst the main focus of their analysis concerned flow in the olfactory groove.

The distribution of flow into various regions in the nasal airways is of considerable interest, in both normal breathing and in sniffing. This question has been investigated

by both Zhu et al. [132] and Segal et al. [101] who performed steady-state simulations at lower breathing rates, representing restful breathing rather than sniffing. Higher nasal velocities have been modelled previously [126] achieving speeds 50% higher than those considered as moderately elevated, which will be the focus of this study. Zachow et al. [126] reported that for steady breathing rate simulations, 3.5 million mesh elements are required for converged pressure loss predictions, but this must be viewed in the context of flow modelling assumptions that do not resolve the detailed unsteady internal dynamics, namely the spontaneous fluctuations associated with transitional or turbulent flow. Until relatively recently, these features were modelled by Reynolds averaged Navier Stokes (RANS) approaches. For example Ghahramani et al. [37] investigated turbulent intensities and their effect on particle deposition in an extensive airway model ranging from the nostrils to above the carina at flow rates comparable to the peak flow rates used in this study. Further studies [31, 54] of particle deposition reported 4 million cells as necessary for mesh independent results. However small scale fluctuations would not be sufficiently resolved at this refinement level, nor are effects of accelerating and decelerating flows covered in steady simulations.

The dynamics of spontaneous flow instability were investigated by Lin et al. [63], who reported simulations of a realistic oral geometry. Large scale flow features were resolved, whilst a comparison between an under-resolved DNS simulation and a large eddy simulation (LES) turbulence model was found to have a relative L1 norm (sum of absolute differences in a volume as a percentage of the total) of turbulent kinetic energy (TKE) of 13.6%. This highlights the need for simulations at higher resolutions to serve as reference studies.

Zhang and Kleinstreuer [127] and Pollard et al. [89] investigated the flow in a highly idealised oral airway model. The former study detailed the turbulent kinetic energy at flow rates of 10 and 30 l min<sup>-1</sup>. High values of turbulent kinetic energy were found in the region below the epiglottis. Various computational models of turbulence were compared with experimental results, concluding that high resolution simulations are desirable.

### 1.3.2 Flow in the Descending Airways

From a fluid dynamics perspective, airflow in the human trachea is of particular interest as it is the largest conduit in the respiratory tract and hence the region where

many interesting fluid mechanical phenomena occur. During inspiration, flow enters the trachea as a jet through a constriction known as the glottis. The flow downstream in the trachea is characterised by breakdown and impingement of the jet, turbulence and secondary flow vortices due to the curvature of the vessel. Typical flow structures have been widely reported in the literature [64, 11, 70, 17] for healthy tracheas. However, the trachea can be affected by a number of pathologies that further influence the flow environment causing constriction, deviation or a combination of both, primarily brought about by constriction of this conduit (e.g. goitres).

Goitres are enlargements of the thyroid gland, which in certain cases can extrinsically compress the trachea, causing it to displace or deform. This can lead to symptoms such as difficulty swallowing, coughing and shortness of breath or an inability to breathe at higher flow rates. The decision to operate to remove goitres is based on a number of patient parameters, including analysis of CT images. The quantification of the effect of compressive goitres can assist surgeons in cases where there is a considerable anaesthetic risk. At present, one method of quantifying the effect is 1D measurements (e.g diameter in a CT slice) of the tracheal anatomy [108]. However these measurements assume that breathing difficulties are related to constriction percentage. Although clearly an important measure, from a fluid mechanics perspective there are other geometric factors to consider e.g. distortion and curvature. Additional diagnostic complications arise when patients suffer also from lower lung pathology, masking the influence of the compressive goitre. Improved fundamental understanding of the relationship between the different geometrical consequences of goitre, their effects on the flow structures and the impact these have on patient symptoms, such as increased work of breathing, would be useful to clinicians. Not only could the immediate effects of the goitre be calculated, but also certain criteria established to predict when critical values of narrowing or distortion are reached, to aid the decision of whether or when to operate.

Previously, a number of studies have investigated the influence of different pathologies on tracheal flow mechanics [6, 71, 75]. Brouns et al. [6] simulated the influence of tracheal stenosis in an idealised tracheal geometry. The stenosis was axisymmetric and positioned in the sub-glottic region. Their results indicated that for an idealised stenosis the relationship between pressure and flow (a power law) deviates only in severely constricted cases (60% and 85% luminal area reduction). Mimouni-Benabu et al. [75] investigated steady flow fluid mechanics in a single healthy and eight constricted infant tracheas with a congenital stenosis; a rare constrictive abnormality existing at birth.

They focused on pressure as a clinical index and concluded that pressure drop is a good indicator for surgery based on retrospective clinical data. It was suggested that the area reduction caused by the stenosis is potentially more important than the length of the constriction. Although this study presented a reasonable number of cases there were some notable drawbacks that could potentially influence their analysis. Firstly, as alluded to by the authors their geometries were obtained from CT data with a coarse slice thickness; hence the reconstructed geometries do not accurately represent the *in vivo* environment. Secondly, they do not consider the glottal region, which is a major controller of tracheal fluid mechanics. Previously, Lin et al. [64], Choi et al. [11] and Pollard et al. [89] have demonstrated that the upper airways need to be considered for an accurate description of the fluid mechanics in the trachea. This is primarily because the glottal jet (which forms due to the glottal constriction) influences turbulent flow structures in the trachea. As to how much of the upper airways must be considered, Choi et al. [11] reported that truncation at the mid-laryngopharynx level provides a good description of tracheal flow mechanics (when compared to the whole upper airways), whilst truncation immediately above the glottis provides satisfactory results. Saksono et al. [95] reported that the whole nasal cavity should be included whilst Bates et al. [4] show the narrowest section may not be at the glottis and that the most constricted section upstream of the trachea dominates.

Although the previous studies of pathological airways provide insight, few details have been provided about the underlying geometric variations (e.g. curvature, area reduction) and their influence on breathing mechanics. To provide an in-depth fluid mechanical analysis of extrinsically constricted airways five tracheal geometries were studied: one normal and four pathological cases. The normal case provides a reference, comparable with the studies of a number of healthy tracheal geometries in literature [64, 11, 70, 66] to compare with the pathological cases. Experimental and numerical simulations of an idealised healthy extra-thoracic airway demonstrated reasonable agreement [40, 3]. Some deviation was observed, but can potentially be attributed to limits on mesh resolution.

### 1.3.3 Modelling and Quantifying Transient Effects

The unsteady aspect of airflow is less explored than steady flow, since the timescale of a breath is sufficiently long during quiet, restful breathing that flow inertia does not excessively dominate viscous forces. By contrast, for high frequency ventilation of the

trachea [111, 12] this is certainly not the case. However, this is an artificial condition, completely different from that of the normal breathing regime. Nevertheless even for normal breathing cycles, differences between quasi-steady and unsteady simulations have been observed. For example, Hörschler et al. [42] found significant hysteresis in the pressure-flow relationship in accordance with the low frequency flow variation during the breathing cycle.

Many previous studies have neglected unsteadiness, performing either steady [19, 28, 31, 37, 54, 110, 117, 118, 124, 129] or quasi-steady [9, 10, 132] simulations. The justification for steady simulations are often based on Strouhal ( $St$ ) or Womersley ( $\alpha$ ) (defined later, equations 2.27 and 2.26) number arguments, for example:

“For a typical diameter of the real nasal airway ( $d \simeq 0.5$  cm), breathing frequency of  $2 \text{ s}^{-1}$ , and the average velocity of  $5.4 \text{ m/s}$  for the medium nasal airflow rate,  $St$  and  $\alpha$  for nasal airflow are estimated to be 0.01 and 4.5 respectively. Although the value of Womersley suggests that unsteadiness may be of some importance, the low value of  $St$  suggests that it is not.”  
Hahn et al. [39]

Subramaniam et al. [109] gives similar reasons for steady simulation, suggesting steady state simulations are acceptable when the Strouhal number is less than one, whilst Keyhani et al. [52] reports that steady simulations are sufficient at Strouhal numbers less than 0.2. The values reported are for steady breathing, but assume the governing frequencies are related to the breathing rate. Rapid acceleration of the flow during inhalation increases the frequency content of the flow waveform and thus the value of  $\alpha$ . Experimental data on the rate of inspiratory flow development has more recently become available. Using high frequency response hot wire instrumentation, Rennie et al. [91] found the time taken for flow to build up to a level equivalent to that in restful breathing to be 130 ms on average in normal inspiration. This was shortened to 90 ms in sniffing, and was found to be as brief as 20 ms in a rapid inhalation.

In addition to the timescales associated with flow build up, there are intrinsic timescales associated with the natural unsteadiness of flow beyond a critical Reynolds number. The critical Reynolds number for instability is greatly reduced from that associated with a channel flow in the presence of large scale separations - one need only contrast the flow past a cylinder with that in a tube. Several studies [52, 128] report large separated flow

regions within the nasal cavities, but do not report the stability of the associated shear layers, nor the effects of any instability.

Modelling unsteady shear layers with RANS type approaches has some uncertainties, but at this stage it is unclear the level of error associated with approximating the dynamics in this way. The current evidence suggests that considering steady flows and for relatively less sensitive measures such as pressure loss and velocity contours, the errors may not be too severe. For example, Nithiarasu et al. [81] compared steady state pressure losses and velocity contours in an idealised oral airway to the quasi-steady experimental results of Heenan et al. [41] and found them to have similar pressure - flow relationships, with a difference in pressure loss of approximately 10% at 30 lmin<sup>-1</sup>. Kimbell et al. [55] suggested that pathological nasal geometries can also be analysed using steady state analysis, but this requires justification. Care must also be taken with regard to the flow regime being studied. At low steady flow rates, experimental results suggest that laminar flow predominates in the nasal airways. Kelly et al. [51] analysed planar velocity profiles in the nose obtained from PIV (particle image velocimetry) experiments at a steady flow rate of 125 mls<sup>-1</sup>. Little change was seen between mean and instantaneous contours, except in regions with high velocity gradients, suggesting steady flow at this very low flow rate, similar to that observed in the experimental visualisations of Doorly et al. [24].

Mylavarapu et al. [76] compared experimental results with various CFD approaches, including steady state RANS and unsteady LES models. The steady RANS results were closest to those found experimentally (20% error compared to 30% for unsteady LES), however the authors report their mesh resolution contained only 550,000 cells and speculate the LES method required a finer grid.

Ishikawa et al. [45] analysed flow patterns in both steady breathing, which is approximated using a sine wave with a rest-phase inserted between inspiration and expiration and a sniff. They report changes in stream line position in the upper nasal cavity in inspiration and expiration, that was not reproducible in steady simulations. They further report that sniffing allows odourants to spread over a larger surface area than in steady breathing. Ishikawa et al. [44] report unsteady simulations make little difference to vortices at relatively coarse mesh resolutions.

Nanoparticle deposition (discussed in section 1.3.4) in a sine wave breathing profile was investigated by Shi et al. [103]. They reported a Strouhal number of 0.2, an order of magnitude higher than that given elsewhere, but still below the steady-limit of 1

given by Pedley et al. [85]. Similar flow patterns were observed in the acceleration and deceleration phases of inhalation, supporting arguments for steady simulation.

Hörschler et al. [42] and Spence et al. [107] investigated the steady state assumption computationally and using PIV respectively. Both found relationships between transient and steady simulations to break down at low Reynolds number. Hörschler et al. [42] quantifies this breakdown point as  $Re < 1500$  and the discrepancy increases if the flow rate is increasing, as acceleration effects are neglected in steady state analysis. Girardin et al. [38] reports regions of turbulence in the nose, which can only be fully captured with unsteady modelling.

In the descending airways, Cui and Gutheil [20] found significant differences between time averaged results and instantaneous flow patterns, despite their highly simplified oral geometry. The secondary flow patterns were not adequately captured in steady simulations nor were the mixing characteristics, meaning steady simulations cannot accurately predict particle motion.

Lee et al. [61] compared a simulation of an experimentally derived breathing cycle with steady state simulations, focussing on velocity profiles, wall shear stress and thermal effects. Significant differences were found in all measures in both inspiration and expiration, although the discrepancies were somewhat larger in expiration. During inspiration, velocity profiles in the larynx were particularly different and contours of pressure less smooth. Xu et al. [125] compared steady and unsteady pressures both experimentally and with CFD and found peak pressures somewhat higher in unsteady flows for the same flow rate. The discrepancy represents the pressure required to accelerate the flow. These studies highlights the importance of understanding the differences in steady and unsteady simulations. This finding was also made by Naftali et al. [77] who found higher instantaneous velocities in unsteady simulations than would be expected from the steady state case, although the pressure loss was similar.

#### 1.3.4 Modelling the Inhalation of Nanoparticles

There are two main methodologies for modelling particle deposition in CFD simulations. The first is Lagrangian, where each particle is modelled individually and is hence computationally expensive. This approach offers an advantage in facilitating incorporation of all necessary force terms to be applied to the particles. The second method is Eulerian, where the particles are modelled as a scalar species advected with the flow.

Further dynamics, such as Brownian motion are modelled with a diffusion coefficient, however inertial effects are neglected. Longest and Xi [67] compared Lagrangian and Eulerian methods of calculating particle deposition in various simplified lower airway geometries. In high deposition regions, the results from the two methods agreed when the Stokes number (equation 2.31) was less than  $5 \times 10^{-5}$ , the same order of magnitude as that found by Cohen and Asgharian [15] ( $1 \times 10^{-5}$ ). In the former study, this correlated to a particle diameter of 120 nm for their geometry and flow conditions. In regions of low particle concentration, it was not computationally possible to model sufficient particle numbers to achieve an accurate deposition map, meaning for small particles, the Eulerian approach is preferable, particularly in transient simulations [67]. In nasal aerosol delivery, this Stokes number limit translates to a particle size of 90 nm during restful breathing and 50 nm in moderate exertion [122]. For particles as large as 400 nm, Longest and Oldham [65] found that the Eulerian approach accurately matched experimental results for total deposition, but localised deposition results could vary by as much as an order of magnitude. A lower bound on particle sizes that may be accurately modelled by Eulerian methods is proposed by Longest and Xi [68] who found that for particles smaller than approximately 12 nm, the Eulerian model underestimated deposition in an oral airway geometry, due to a lack of slip correction factor in the Eulerian model. However, this result was not found in all geometries and may instead be due to the resolution of boundary layers in the simulation. Within this particle size range (specifically 14 - 52 nm), Krause et al. [59] found Eulerian computations to match experimental results in an idealised oral geometry. The differences found were thought to be due to the RANS turbulence modelling approach utilised, as the flow field differed more from PIV results than comparative LES results. Deposition was found to be more localised with smaller particles, whilst larger particles were more dispersed.

Kolanjiyil and Kleinstreuer [58] found gravitational effects on nanoparticle deposition in the airway to be negligible (less than 1% difference in the ratio between particles deposited on a surface and the inlet mass flux of particles). It was also reported that particle transport history affected deposition maps, suggesting the importance of transient simulations. Shi et al. [103] found that nanoparticle deposition in cyclic breathing profiles can be approximated by steady simulations with a steady Reynolds number between the peak and mean values of the transient simulation. However, it is unclear whether their methodology allows for the high deposition rates found between inhalation and exhalation or the effects of rebreathing. Zhao et al. [130] compared models of

sniffing using laminar simulations and  $k - \omega$  and Spalart-Allmaras turbulence models and found little difference in particulate absorption between the models.

The effects of turbulence on particle deposition were found to be highest in the nasal vestibule and larynx in inhalation [122] and larynx and pharynx during exhalation [123]. Furthermore, the latter study demonstrates that particle deposition is more dependent on flow rate than particle size and also shows the importance of realistic over idealised geometry in predicting deposition patterns.

Inthavong et al. [43] used a Lagrangian modelling approach and found high deposition, 72%, for small nanoparticles (1 nm) in a nasal geometry, but this reduced to 18% for 10 nm particles, this value remained relatively constant for particles up to 150 nm. Ge et al. [35] used a similar approach and found that smaller particles are predominantly absorbed in the anterior nose, whereas larger particles travel further. Furthermore, low flow rates were intuitively found to increase the effects of diffusion. Both these studies only considered particles in steady flows.

Tang and Guo [112] found that flow solutions based on RANS turbulence models lead to overestimates of particle deposition, with more accurate results obtained using LES approaches. This effect was exacerbated as particle size became smaller, towards those considered in this study.

Larger particles (5  $\mu\text{m}$ ) are considered by Sandeau et al. [97]. At this size, the majority of particles are deposited in the region of the epiglottis as their inertia is considerably larger than that of nanoparticles. Therefore Si et al. [104] considered therapeutic particle delivery from a device within the nose rather than at the nostril. This method significantly improved delivery to the olfactory epithelium. Karakosta et al. [48] found significant differences between transient and steady simulations, and particularly the time at which particles are “released”. They also found that a much finer mesh resolution is required to converge particle deposition results compared to variables such as velocity. This highlights the need for high resolution, transient studies.

Kolanjiyil and Kleinstreuer [57] demonstrated the importance of deposition studies finding that 99% of nanoparticles inhaled to alveolar level remain 24 hours later, which in the case of toxic particles can have significant effects on health.

## 1.4 Motivation

This work focuses on three aspects of inhalation. Firstly, the temporal aspects of airflow have not been fully explored. Air undergoes rapid acceleration during breathing manoeuvres such as sniffing. The way in which the flow develops and how long patterns take to emerge has not been established. Furthermore, the effects of the transient inflow conditions on the turbulent properties of the flow have not been characterised. Chapter 4 discusses a high resolution study of a sniff and quantifies the relevant time scales, unsteadiness and turbulence parameters.

Many previous studies have investigated particle deposition in the airways, as it has great applicability for therapeutic drug delivery and studies into toxic particle inhalation. Again, the temporal aspects have not been quantified: how quickly do particles permeate through the airways and how does this compare with estimates based on the flow rate and airway volume? Addressing these questions relies on detailed knowledge of how air drawn into the nose traverses the airways; these questions are investigated in chapter 5. The effects of diffusion and absorption are also characterised with focus on four types of particle representing the extremes of variations in the above parameters.

Chapter 6 investigates flow in the descending airways, particularly from the glottis to the carina. This is the region in which many interesting fluid dynamics phenomena occur, including confined jets, turbulent structures and strong secondary flows. This chapter considers flow during the established phase of inspiration, guided by the temporal dynamics explored in the earlier part of the thesis. It also shows how the methodologies introduced throughout this work can be used to characterise the effects of pathologies which result in geometric changes. The pathology of interest for this part is the compressive goitre, the consequences of which for tracheal airflow are investigated.

Simulations discussed in all three chapters have been performed at high spatial and temporal resolution, approaching the requirements for fully resolved DNS. A detailed explanation of the methods used in this work is provided in chapter 2. The entire modelling process is covered; geometry creation from medical images, surface preparation, meshing the airspaces, numerical simulation and analysing the results. Various metrics, discussed in chapter 3, have been employed to quantify how well resolved these simulations are. Apart from the primary use of the computational methodology, namely to explore the physics of the unsteady flows, it is hoped that the results of these large simulations can serve as a reference against which more affordable simulations may be

compared. The results from chapters 4 and 5 are compared both to low resolution simulations and a quasi-steady simulation, neglecting the effects of the flow establishment phase, whilst chapter 6 compares these results to reduced fidelity LES simulations.

The fundamental aim of this work is to characterise airflow in human inhalation in order to aid clinical decision making. This aim is achieved through detailed simulation and analysis of airflow during inhalation to determine the mechanics involved. Identifying the anatomical features (both in normal cases and those with pathologies) which govern flow patterns highlights which regions will be the most affected by surgical interventions. It may also help identify which patients would benefit from surgery, for example by determining if an airway obstruction is likely to severely reduce flow to a particular regions. An example of such a tool is the introduction of ‘utilised area’ as a metric, which is used to characterise which regions of the airways carry the bulk of the flow. This measure is intended to help clinicians considering surgical procedures to see which regions of the airway would benefit from intervention, as opposed to consideration of the entire airway cross section.

## 1.5 Journal and Conference Papers

The following journal and conference papers and presentations have arisen from the material presented in this thesis.

- A.J. Bates, R. Cetto, H. Calmet, A.M. Gambaruto, N.S. Tolley, G. Houzeaux, R.C. Schroter, D.J. Doorly. Dynamics of airflow in a short inhalation. *Journal of the Royal Society Interface*. 12(102):20140880, 2015.
- B. Eguzkitza, G. Houzeaux, H. Calmet, M. Vázquez, B. Soni, S. Aliabadi, A.J. Bates, D.J. Doorly. A gluing method for non-matching meshes. *Procedia Engineering*. 61:258-263, 2013.
- A.J. Bates, R. Cetto, D.J. Doorly and A.M. Gambaruto. Flow dynamics of inspiration. *11th World Congress on Computational Mechanics*. 2014.
- A.J. Bates, R. Cetto, N. Tolley, R.C. Schroter, D.J. Doorly. Airflow Dynamics in a Short Inhalation. *Proceedings of the 5th International Conference on Computational Methods*. 2014.

- A.J. Bates, H. Calmet, R. Cetto, D.J. Doorly, G. Houzeaux, R. de la Cruz, M. Vázquez and A.M. Gambaruto. Modelling a sniff in extensive human airways: Aspects of physiology and fluid mechanics. *Congress on Numerical Methods in Engineering 2013 Proceedings*. 2013.
- R. Cetto, A. J. Bates, A. P. Comerford, G. Madani, D. J. Doorly, N. S. Tolley. Computational simulations of airflow in tracheal compression due to retrosternal goitre. *Hamlyn Symposium on Medical Robotics*. 2014.

## 2 Methods

Performing and analysing biomedical computational fluid dynamics simulations involves several steps, which are presented in this chapter. Firstly, realistic, patient-specific geometries have to be created to match the *in vivo* anatomy of the subject. These geometries are extracted from medical images made up of many voxels, hence the extracted surfaces require smoothing to achieve surfaces which appear similar to those seen *in vivo* (viewed for example, via a nasal endoscopy.) The volume enclosed by the surface then has to be divided into a mesh of small cells, in which the governing equations of fluid flow can be solved. The methods by which these equations are solved is discussed, along with the boundary conditions necessary to replicate *in vivo* conditions. Further equations for modelling particle motion are presented. Finally, a number of metrics to characterise the resulting flow are defined, allowing comparison with other flows and analysis of aspects of the flow such as turbulence.

### 2.1 Geometry Capture

All considered geometries are derived from medical imaging. Two modalities are used, computed tomography (CT) and magnetic resonance imaging (MRI). Both result in a 3D image matrix covering the anatomic region of interest, with the intensity of each constituent voxel related to the density of the tissue in that part of the field of view. Voxel sizes tend to be non-isometric, with planes taken in a specific orientation. In-plane voxel size is often smaller than the slice thickness and distance between planes. CT scans involve the subject being exposed to significant levels of radiation, whereas MRI causes no damage and hence is obtainable for normal subjects. The modalities differ in their responses to different tissues. MRI is more sensitive to soft tissue, and hence the mucosa lining the airways [13]. Therefore, the same airway scanned in both modalities may appear more patent in the CT image.

Once the image cube has been created, those voxels which represent the airway must be selected. This step is performed by ear, nose and throat surgeons. Several segmentation techniques were investigated, with the commercial code Mimics 15 (Materialise, Leuven, Belgium) found to produce accurate surfaces most quickly. The software uses simple thresholding and contiguous region selection to delineate the airway, which is then manually edited where necessary.

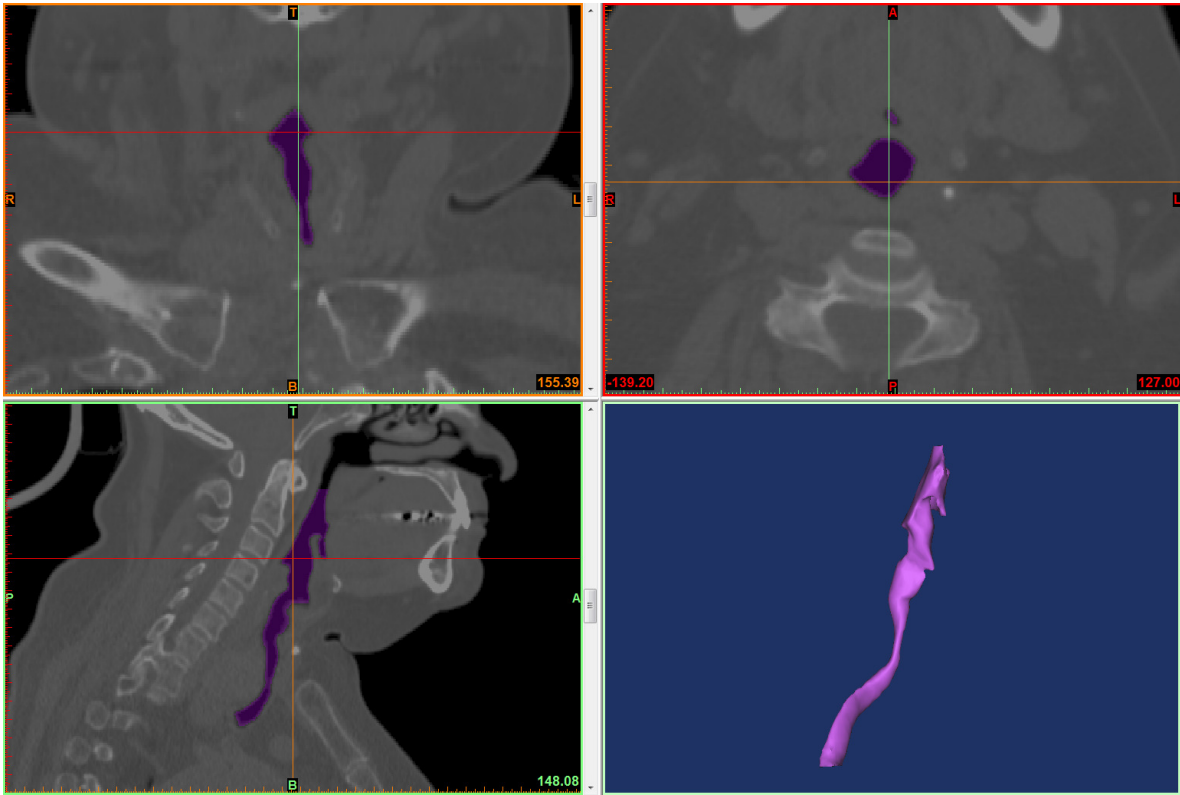


Figure 2.1: Example segmentation of a trachea, larynx and pharynx from a CT image. Clockwise from bottom left: sagittal, coronal, axial and 3D rendering of segmented surface. The image is a screenshot from the Mimics software package, created by R. Cetto and used with permission.

3D surfaces are created at the edges of the delineated region and smoothed using bilaplacian smoothing in MeshLab (Visual Computing Lab - ISTI - CNR). This technique is performed using the method proposed by Taubin [113], which does not allow volumetric shrinking but also does not enhance low frequency surface features [82]. Taubin smoothing uses two scale factors similar to the one used in Laplacian smoothing, but with opposite signs. To achieve bilaplacian smoothing, the two scale factors are applied with the same absolute values, but maintaining the opposite signs [82].

## 2.2 Meshing

The airspaces were meshed using Star-CCM+ 8.04.007-r8 (CD-adapco, Melville, NY, USA). The mesh elements were polyhedral in the bulk of the geometry with prismatic layers lining the walls. The choice of mesh element is significant as comparisons between

polyhedral and tetrahedral meshes have shown that polyhedrons can resolve the flow to the same resolution as a tetrahedral grid with up to five times as many elements [86].

Prismatic layers are used along the boundary walls as the gradients of quantities such as velocity and temperature are often highest at the wall. The height of the prism cells is controlled to ensure accurate calculation of these gradients, as is their growth rate from the first wall layer to their interface with the bulk elements.

Specific details of the mesh used for each simulation is given in the relevant chapter.

## 2.3 Numerical Simulation

Star-CCM+ 8.04.007-r8 (CD-adapco, Melville, NY, USA) was used to perform the numerical simulations. A detailed reference for the solver can be found in the software’s documentation [8], but a brief overview is provided here.

The Navier-Stokes equations are solved using a segregated approach, suitable for incompressible or mildly compressible problems. The formulation uses a colocated variable arrangement and a Rhie and Chow-type [92] pressure velocity coupling combined with a SIMPLE-type algorithm [8] (semi-implicit method for pressure- linked methods).

The continuity equation for an incompressible fluid is

$$\nabla \cdot \mathbf{u} = 0 \tag{2.1}$$

expressed in strong form, where  $\mathbf{u}$  is the velocity. The momentum equation is

$$\rho \left( \frac{\partial \mathbf{u}}{\partial t} + \mathbf{u} \cdot \nabla \mathbf{u} \right) = -\nabla p + \mu \nabla^2 \mathbf{u} \tag{2.2}$$

where  $\rho$  the density,  $p$  is the pressure and  $\mu$  is the dynamic viscosity. As a finite volume approach is to be used to solve these equations, it is convenient to express these equations in integral form. For continuity, application of Gauss’ divergence theory gives

$$\oint_A \mathbf{u} \cdot d\mathbf{a} = 0 \tag{2.3}$$

where  $\mathbf{a}$  is a vector representing the surface of a cell, whilst the integral form of the momentum equation is

$$\frac{\partial}{\partial t} \int_V \rho \mathbf{u} dV + \oint_A \rho \mathbf{u} \otimes \mathbf{u} \cdot d\mathbf{a} = - \oint_A p \mathbf{I} \cdot d\mathbf{a} + \oint_A \mathbf{T} \cdot d\mathbf{a} \quad (2.4)$$

where  $t$  is time,  $V$  is the cell volume,  $\rho$  is the density,  $\mathbf{I}$  is the identity matrix,  $\mathbf{T}$  is the viscous stress tensor. The terms in equations 2.2 and 2.4 represent, from left to right, the rate of change, the convective flux, the pressure gradient, and the viscous flux terms.

The continuous form of the transport equation of a scalar,  $\phi$  (as an example) is

$$\frac{\partial \rho \phi}{\partial t} + \nabla \cdot (\rho \mathbf{u} \phi) = \nabla \cdot (D \nabla \phi) \quad (2.5)$$

where  $D$  is the diffusion coefficient. In integral form (again due to the finite volume approach utilised in solving the equations) this can be expressed as

$$\frac{d}{dt} \int_V \rho \phi dV + \oint_A \rho \phi \mathbf{u} \cdot d\mathbf{a} = \oint_A D \nabla \phi \cdot d\mathbf{a} \quad (2.6)$$

whilst, finally in discretised form, suitable for applying to a mesh element, it is

$$\frac{d}{dt} (\rho \phi V) + \sum_f [\rho \phi (\mathbf{u} \cdot \mathbf{a})]_f = \sum_f (D \nabla \phi \cdot \mathbf{a})_f \quad (2.7)$$

where  $f$  represents the faces of the mesh element in question. From left to right, the terms in equation 2.6 are the transient term, the convective flux, and the diffusive flux.

The transient term in equation 2.7 is solved by a second order discretisation scheme, whilst the convection term is discretised as follows,

$$[\rho \phi (\mathbf{u} \cdot \mathbf{a})]_f = \dot{m}_f \phi_f \quad (2.8)$$

with  $\dot{m}_f$  representing the mass flow rate at the cell face. It is computed using a bounded central-differencing approach for simulations using LES and a second-order upwind scheme otherwise. An implicit unsteady approach is used, meaning each time step consists of several inner iterations to converge the solution for that instant in time. The outer temporal discretisation is controlled by setting the time step. The particular settings used for each simulation are discussed in the relevant section for that simulation's resolution.

In this study two different solution methodologies are utilised; DNS and LES. For the former, attempts were made to resolve all scales, whilst for the latter, the model is used to represent the effect of unresolved scales. The filtered form of the incompressible Navier-stokes equations, with the subgrid-scale tensor modelled using Boussinesq's hypothesis, reads

$$\frac{\partial}{\partial t} \bar{\mathbf{u}} + \bar{\mathbf{u}} \cdot \nabla \bar{\mathbf{u}} = -\frac{1}{\rho} \nabla \bar{p} + \nabla \cdot \left( (\nu + \nu_t) (\nabla \bar{\mathbf{u}} + \nabla \bar{\mathbf{u}}^T) \right) \quad (2.9)$$

$$\nabla \cdot \bar{\mathbf{u}} = 0, \quad (2.10)$$

where  $\bar{\mathbf{u}}$  is the velocity,  $\bar{p}$  the modified pressure (where the isotropic part of the subgrid-scale tensor is added to the filtered pressure),  $\nu$  the kinematic viscosity and  $\nu_t$  the eddy viscosity. The eddy viscosity model chosen for the present study is the WALE model [80]. This model provides more accurate modelling of the eddy viscosity in the near wall region and is given by

$$\nu_t = \Delta_w^2 S_w \quad (2.11)$$

where  $\Delta_w$  is the length scale (local grid filter) based on element volume,  $V$ , given by

$$\Delta_w = C_w V^{\frac{1}{3}} \quad (2.12)$$

with  $C_w$  equal to 0.544. The deformation parameter  $S_w$  is defined by

$$S_w = \frac{\mathbf{S}_d : \mathbf{S}_d^{\frac{3}{2}}}{\mathbf{S}_d : \mathbf{S}_d^{\frac{5}{4}} + \bar{\mathbf{S}} : \bar{\mathbf{S}}^{\frac{5}{2}}} \quad (2.13)$$

where  $\mathbf{S}_d$  is a traceless tensor related to the square of the velocity gradient tensor given by

$$\mathbf{S}_d = \left[ \nabla \bar{\mathbf{u}} \cdot \nabla \bar{\mathbf{u}} + (\nabla \bar{\mathbf{u}} \cdot \nabla \bar{\mathbf{u}})^T \right] - \frac{1}{3} \text{tr}(\nabla \bar{\mathbf{u}} \cdot \nabla \bar{\mathbf{u}}) \mathbf{I} \quad (2.14)$$

and  $\bar{\mathbf{S}}$  the rate-of-strain tensor (resolved scale) given by

$$\bar{\mathbf{S}} = \frac{1}{2} (\nabla \bar{\mathbf{u}} + \nabla \bar{\mathbf{u}}^T) \quad (2.15)$$

The simulations in this work use incompressible flow throughout the airways: nowhere is the flow fast enough for compressibility to become apparent. The maximum Mach number (defined as the ratio of flow speed to the speed of sound in that fluid) found in these studies is 0.088 which is less than the value of 0.3 commonly used as the point when compressibility effects becomes significant.

## 2.4 Particle Motion

This study will only consider nanoparticles. These are small and light enough that their inertia is negligible and their motion is due to advection by the flow and diffusion. Therefore, they can be modelled as scalar species with the transport equation 2.5, with their diffusion set by the user. As the velocity at the wall must be zero, there can be no absorption without diffusion. The Saffman lift force, (that due to the velocity gradient across the particle) is neglected here as the size of the particles means these velocity gradients will be small. Zheng and Silber-Li [131] show that this force dominates in the range  $2 < \frac{z}{2r} < 6$ , where  $z$  is the distance to the wall and  $r$  is the particle radius. For a 10 nm particle, this gives a range of  $4 \times 10^{-8}$  m to  $1.2 \times 10^{-7}$  m, which is smaller than the first layer of prism cells used in this study.

## 2.5 Boundary conditions applied to the simulations

For simulations to achieve physiologically realistic results, the boundary conditions of the simulation have represent the *in vivo* conditions on all anatomical surfaces. Non-realistic surfaces are necessary at the inlet and outlet of the domain to close the volume to be simulated and in cases where the inlet is outside of the airways, to limit the domain to be simulated. The boundary conditions control the flow of air into and out of the domain, the interactions between the walls of the domain (both anatomical and artificial) and the interactions between particles and the walls.

### 2.5.1 Flow inlets and outlets

All simulations in this work use a specified velocity or mass flow at the inlet, unless otherwise stated. The velocity will be directly applied to all cell faces on the boundary, with a direction inwards and normal to the faces. For the pressure inlets used in certain

cases, the inlet total pressure is directly specified, and the inlet face velocity is calculated from the total and static temperatures, which in turn are obtained from the total and static pressures.

All simulations use pressure outlets, where the static pressure is specified by the user. All simulations have their inlets and outlets located sufficiently far from the region of interest so that the flow there is not affected and to ensure well posed boundary conditions. These locations are described in detail for each case in the relevant sections.

### 2.5.2 Flow-wall interactions

All walls are modelled with no slip conditions, the effects of ciliated flow movements are neglected as they are small [100] compared to the bulk flow. These may be relevant in studies of clearance times of sinuses, for example, but these details are not considered here. All walls are considered to be rigid, as imposed motion or fluid structure interaction simulations are beyond the scope of this work. Fodil et al. [30] demonstrated that there is no significant change in area until higher nasal pressure drops ( $>100$  Pa) than are considered here.

### 2.5.3 Particle-wall interactions

Scalar species are modelled either as non absorbing, in which case, for a scalar  $\phi$  the boundary condition is set so that the gradient in the normal direction away from the wall is equal to zero

$$D\nabla\phi \cdot \mathbf{n}_w = 0 \quad (2.16)$$

where the subscript  $w$  denotes a value taken at the wall, and  $\mathbf{n}_w$  is the normal vector at the surface. Alternatively, the concentration at the wall is 0 and the scalar is entirely absorbed

$$\phi_w = 0 \quad (2.17)$$

This absorption boundary condition assumes the mucosa can absorb infinite scalar at each time step and does not become saturated, therefore simulating absorption characteristics in this way may result in higher absorption than would be the case *in vivo*.

No scalar is absorbed in certain regions, therefore even scalars which are absorbed within the airways will have regions which are set to not absorb, using equation 2.16. The face and all non-anatomic wall surfaces are set to be non-absorbing. Within the nose, the nasal vestibule is lined with a tissue which is more similar to exterior epidermis than the mucosal airway lining, so absorbs very little. Therefore, the absorbing boundary condition 2.17 is only used posterior to the nasal valve. In reality, the transition between the tissue types is gradual, however this transition is not modelled and an abrupt change is seen. This will result in higher than expected absorption in the region where the boundary layer changes, however this is not expected to have significant downstream affects, as the increased absorption in this small region is likely to be similar to the total absorption that would have occurred had the transition region been modelled.

## 2.6 Flow Metrics

### 2.6.1 Temporal Means and Variances

In this study, averaging operations are utilised to interpret turbulent quantities. For a specific flow variable  $f$  the time average,  $\bar{f}$ , is defined by,

$$\bar{f} = \frac{1}{T} \int_t^{t+T} f(x, y, z, t) dt, \quad (2.18)$$

where  $T$  is the time period over which the variable is sampled, this value is given in each section where it is used. Numerically this procedure is defined by

$$\overline{f(x, y, z, t)} = \frac{1}{N} \sum_{i=0}^N f_i(x, y, z, t), \quad (2.19)$$

where  $N$  indicates the number of samples taken over the period  $T$ . Turbulent fluctuations ( $f'$ ) are represented by the instantaneous deviation from this mean value defined by

$$f'(x, y, z, t) = f(x, y, z, t) - \overline{f(x, y, z, t)}. \quad (2.20)$$

Using equation 2.20 the variance of these fluctuations is defined by

$$\begin{aligned} \text{Var}(f') &= \overline{f'(x, y, z, t)^2} \\ &= \overline{f(x, y, z, t)^2} - (\overline{f(x, y, z, t)})^2 \end{aligned} \quad (2.21)$$

Numerically equation 2.21 can be expressed by

$$\text{Var}(f') = \frac{1}{N-1} \left[ \sum_{i=1}^N f_i^2 - \frac{1}{N} \left( \sum_{i=1}^N f_i \right)^2 \right] \quad (2.22)$$

which represents the square of the root mean square value  $f'_{rms}$ , which is commonly quoted in literature. The variance of velocity is used to reveal regions of significant fluctuations in the velocity field, and is calculated using equation 2.22, setting the fluctuating velocity as the variable of interest. The variance of velocity is linearly related to the turbulent kinetic energy by a ratio of  $\frac{2}{\rho}$ , where  $\rho$  is the density of air.

### 2.6.2 Non-dimensional Numbers

The hydraulic diameter,  $d_H$ , of a cross-section through an arbitrary conduit such as the airway is given by

$$d_H = \frac{4A}{P} \quad (2.23)$$

which is a representative length scale for the section. Here,  $A$  is the area and  $P$  the perimeter of a cross-section)

The mean cross sectional Reynolds number,  $Re$  was calculated using the formula

$$Re = \frac{\rho \bar{U} d_H}{\mu} \quad (2.24)$$

where  $\rho$  is the fluid density,  $\bar{U}$  the surface mean of the temporal mean of the normal velocity across each plane, calculated as defined in equation 2.18, setting the velocity as the variable of interest,  $\mu$  is the dynamic viscosity of the fluid and

Likewise, the Dean number,  $De$  was defined as

$$De = Re \left( \frac{d_H \kappa}{2} \right)^{\frac{1}{2}} \quad (2.25)$$

where  $\kappa$  is the local curvature (the inverse of the radius of curvature).

The Womersley number,  $\alpha$ , given by

$$\alpha = d_H \left( \frac{\omega}{\nu} \right)^{\frac{1}{2}} \quad (2.26)$$

where  $\omega$  is the angular frequency of the oscillations and  $\nu$  the kinematic viscosity is the ratio of the transient inertial force over the viscous forces and is used to characterise unsteadiness in the flow. When the Womersley number is less than 1, the flow has time to become fully developed during each cycle and the pressure and velocity profiles are in phase. As  $\alpha$  increase to around 10, the oscillations mean boundary layers do not have time to fully develop in each cycle and the velocity lags behind the pressure gradient by approximately  $90^\circ$  [78].

The Strouhal number,  $St$ , given by

$$St = \frac{fd_H}{\bar{U}} \quad (2.27)$$

where  $f$  is the frequency of oscillations ( $f = \frac{\omega}{2\pi}$ ) is also used to characterise unsteadiness in the flow. For Strouhal numbers of order 1, viscous forces dominate the flow leading to collective oscillations, whereas at order  $10^{-4}$ , the high speed, quasi-steady motion dominates [106]. The Reynolds, Womersley and Strouhal numbers are related by

$$\alpha = (2\pi ReSt)^{\frac{1}{2}} \quad (2.28)$$

The Schmidt number,  $Sc$  is calculated as

$$Sc = \frac{\mu}{\rho D} \quad (2.29)$$

where  $D$  is the diffusivity and is the ratio of viscous diffusion to molecular diffusion, while the Péclet number,  $Pe$ , is given by

$$Pe = ReSc = \frac{d_H U}{D} \quad (2.30)$$

and is the ratio of advective to diffusive transport rates.

The Stokes number,  $Stk$ , is given by the equation

$$Stk = \frac{\rho_p d_p^2 C_c \bar{U}}{18\mu d_H} \quad (2.31)$$

where  $\rho_p$  and  $d_p$  are the particle density and diameter,  $\mu$  and  $\bar{U}$  refer to the fluid, as above and  $C_c$  is the Cunningham correction factor, defined as

$$C_c = 1 + \frac{2\lambda}{d_p} \left( A_1 + A_2 e^{-\frac{A_3 d_p}{\lambda}} \right) \quad (2.32)$$

This term is used to account for non-continuum effects in small particles, where  $\lambda$  is the mean free path and  $A_1$ ,  $A_2$  and  $A_3$  are experimentally determined constants. For air at standard conditions,  $\lambda = 68$  nm,  $A_1 = 1.257$ ,  $A_2 = 0.400$  and  $A_3 = 0.55$  [21]. The Stokes number is used to characterise the behaviour of particles suspended in a fluid. It is defined as the ratio of the characteristic time of a particle to that of the fluid i.e. how quickly the particle responds to changes in the flow field. When the Stokes number is small ( $\ll 1$ ), the particle follows the streamlines of the flow closely, but detach when the Stokes number rises.

### 2.6.3 Vorticity, Wall Shear Stress and Turbulence Intensity

The vorticity,  $\omega$ , of the fluid is given by

$$\omega = \nabla \times \mathbf{u} \quad (2.33)$$

and is the curl of the velocity field  $\mathbf{u}$ .

The wall shear stress  $\tau_w$ , is defined by

$$\tau_w = \mu \left( \frac{\partial u_i}{\partial x_j} + \frac{\partial u_j}{\partial x_i} \right) n_j \quad (2.34)$$

where  $u_i$  and  $u_j$  are velocity components and  $n_j$  a component of the wall normal vector.

Turbulence intensity ( $T_u$ ) values are defined by

$$T_u = \frac{\sqrt{\frac{1}{3} (\overline{u'^2} + \overline{v'^2} + \overline{w'^2})}}{|V|} = \sqrt{\frac{1}{3}} \frac{|V'|}{|V|} \quad (2.35)$$

where  $u'$ ,  $v'$  and  $w'$  are the fluctuating components of velocity, calculated using equation 2.20 and  $|V|$  is the magnitude of the velocity.

### 2.6.4 Utilised Area

The distribution of flow in both stenotic [116] and curved [5] geometries has been shown to be non-uniform. In order to quantify the cross-sectional area effectively used by the bulk of the flow, two measures of utilised area (UA) are proposed;  $UA_{\max}$  and  $UA_{\text{mean}}$ . The area  $UA_{\max}$  is the section of the cross-sectional plane where the local plane-normal velocity,  $\mathbf{U} \cdot \hat{\mathbf{n}}$  is above half the maximum  $\mathbf{U} \cdot \hat{\mathbf{n}}$  on that cross-section ( $\hat{\mathbf{n}}$  being the normal unit vector to the plane). Alternatively,  $UA_{\text{mean}}$  is the area where  $\mathbf{U} \cdot \hat{\mathbf{n}}$  is greater than the mean value for that plane. Both  $UA_{\max}$  and  $UA_{\text{mean}}$  are then expressed as ratios to the total available area,  $A$ . A diagram representing a general UA is shown in figure 2.2 and to provide some context for these values, table B.1 in appendix B shows the values for several types of fully developed flow which have analytical solutions, all calculated for circular ducts.

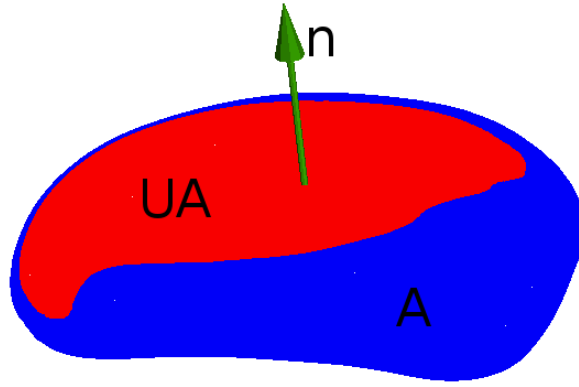


Figure 2.2: The utilised area, UA shown in red on a plane of area A, in blue. The plane's normal vector,  $\hat{\mathbf{n}}$  is represented by the green arrow.

### 2.6.5 Energy Flux

The instantaneous energy flux,  $E_\phi$  through each cross-sectional plane is given by

$$E_\phi = \int_S \left[ (\mathbf{U} \cdot \hat{\mathbf{n}}) P_s + \frac{1}{2} \rho (\mathbf{U} \cdot \hat{\mathbf{n}}) |\mathbf{U}|^2 \right] dS \quad (2.36)$$

The change in energy flux along the length of the geometry equals the energy required to drive the flow through the geometry due to frictional losses.  $\mathbf{U}$  is the velocity vector,

$\hat{\mathbf{n}}$  is the normal unit vector of the plane, which has the surface  $S$ .  $P_s$  is the static pressure on the plane and  $\rho$  is the density of air.

The total energy lost in driving flow between planes  $i$  and  $j$  in a period  $t$  is shown in therefore

$$\Delta E = \int (E_{\phi,i} - E_{\phi,j}) dt \quad (2.37)$$

### 2.6.6 Scalar Quantities

The flux of scalar  $\phi$  through planes is calculated using the following equation

$$\int (\phi \mathbf{u} + D \nabla \phi) \cdot \hat{\mathbf{n}} da \quad (2.38)$$

where  $D$  is the diffusivity. In the bulk of the flow, the second term is small and can be neglected (figure 5.16). However, at any point on the wall, the velocity is zero, so the flux at that point becomes  $D \nabla \phi \cdot \hat{\mathbf{n}}$ . The saturation of volume  $V$  is calculated as  $\frac{\int \phi dV}{V}$ .

### 2.6.7 Vortex Identification

The parameter  $\lambda_2$ , proposed by Jeong and Hussain [46], is used to highlight vortical features within the flow. It is defined as the median ( $\lambda_1 \geq \lambda_2 \geq \lambda_3$ ) eigenvalue of

$$S_{ik}S_{kj} + \Omega_{ik}\Omega_{kj} \quad (2.39)$$

where

$$S_{ij} = \frac{1}{2} \left( \frac{\partial u_i}{\partial x_j} + \frac{\partial u_j}{\partial x_i} \right) \quad (2.40)$$

and

$$\Omega_{ij} = \frac{1}{2} \left( \frac{\partial u_i}{\partial x_j} - \frac{\partial u_j}{\partial x_i} \right) \quad (2.41)$$

$\mathbf{S}$  and  $\mathbf{\Omega}$  are the symmetric and antisymmetric parts of the velocity gradient tensor  $\nabla \mathbf{u}$ , respectively.

### 2.6.8 Turbulent Quantities and Spectra

The mesh size and time step can be compared to the smallest scales in the flow, the Kolmogorov length and time scales, so that the scales which the simulation has resolved can be determined. These values are both calculated from the dissipation,  $\varepsilon$  which is defined by Delafosse et al. [22] as

$$\varepsilon = \nu \left\{ 2 \left( \overline{\left( \frac{\partial u'_1}{\partial x_1} \right)^2} + \overline{\left( \frac{\partial u'_2}{\partial x_2} \right)^2} + \overline{\left( \frac{\partial u'_3}{\partial x_3} \right)^2} \right) + \overline{\left( \frac{\partial u'_1}{\partial x_2} \right)^2} + \overline{\left( \frac{\partial u'_2}{\partial x_1} \right)^2} + \overline{\left( \frac{\partial u'_1}{\partial x_3} \right)^2} + \overline{\left( \frac{\partial u'_3}{\partial x_1} \right)^2} + \overline{\left( \frac{\partial u'_2}{\partial x_3} \right)^2} + \overline{\left( \frac{\partial u'_3}{\partial x_2} \right)^2} + 2 \left( \overline{\frac{\partial u'_1}{\partial x_2} \frac{\partial u'_2}{\partial x_1}} + \overline{\frac{\partial u'_1}{\partial x_3} \frac{\partial u'_3}{\partial x_1}} + \overline{\frac{\partial u'_2}{\partial x_3} \frac{\partial u'_3}{\partial x_2}} \right) \right\} \quad (2.42)$$

where  $u'_1$ ,  $u'_2$  and  $u'_3$  represent the components of fluctuating velocity and  $\nu$  the kinematic viscosity. The fluctuating velocity gradients are calculated using equation 2.20 and setting  $\frac{\partial u_1}{\partial x_1}$  as the values of interest, for example. The instantaneous values are stored for all instances, so the mean and fluctuations can be determined in post-processing. The Kolmogorov length scale,  $\eta$  is then calculated by

$$\eta = \left( \frac{\nu^3}{\varepsilon} \right)^{\frac{1}{4}} \quad (2.43)$$

and the Kolmogorov time scale,  $\tau_\eta$  by

$$\tau_\eta = \left( \frac{\nu}{\varepsilon} \right)^{\frac{1}{2}}. \quad (2.44)$$

Spectra of velocity fluctuations are used to characterise the amount of energy at various scale lengths within the flow. The spectra are calculated using the method described by Varghese et al. [116]. The three components of fluctuating velocity  $u'_1$ ,  $u'_2$  and  $u'_3$  are considered separately and the resultant spectra summed in the frequency domain. Each component consists of a series of values; one taken at each time step over the period of interest. At each instant the fluctuation is calculated as in equation 2.20. The array of data points is divided into sections and each one convolved with a Hann filter  $w(n)$ , defined as

$$w(n) = 0.5 \left( 1 - \cos\left(\frac{2\pi n}{N-1}\right) \right) \quad (2.45)$$

where  $n$  is the sample number and  $N$  the total number of samples, to reduce aliasing effects. The fast Fourier transform of the resultant is then taken for each section and the section's results averaged (this produces smoother spectra than taking the overall spectrum). A correction factor is then applied to compensate for the Hann filter (division by the square of the mean of the Hann window function). To check the accuracy of this process, the energy of the signal is compared in the time and frequency domains, with the same result expected.

The frequencies are multiplied by  $\frac{2\pi}{U}$ , to convert to wave-number where  $U$  is the mean velocity at the point where the spectrum is calculated. For comparison with the spectra analysed by Saddoughi and Veeravalli [94], they are further multiplied by  $\eta$ , the Kolmogorov length scale (equation 2.43) and the spectra are divided by  $(\varepsilon\nu^5)^{\frac{1}{4}}$ , where  $\varepsilon$  is the viscous dissipation rate (equation 2.42).

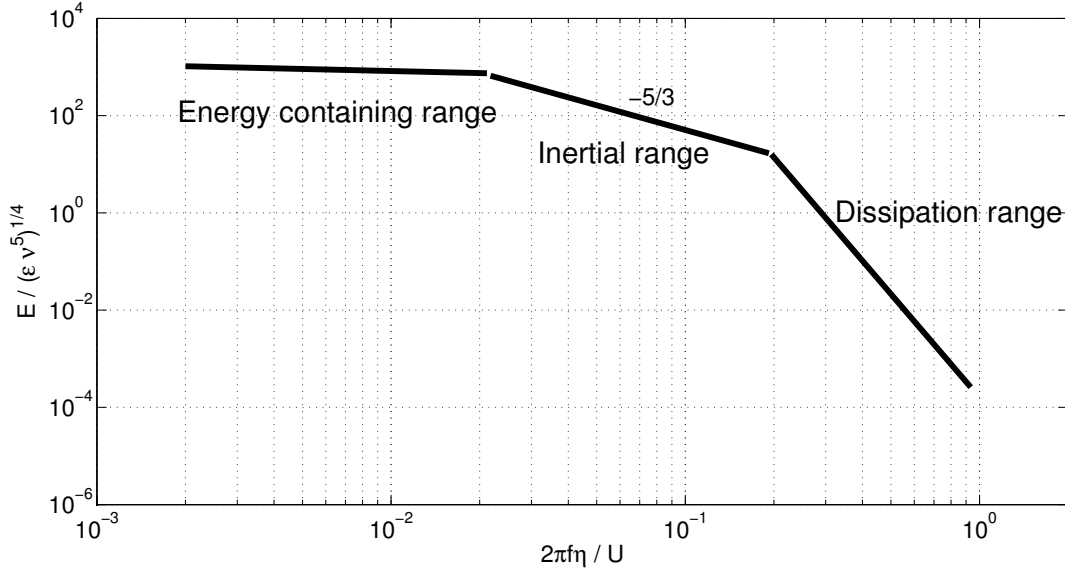


Figure 2.3: The ranges of an idealised turbulent spectrum.

Turbulent flows are characterised by a cascade of eddies of decreasing size [90]. Large flow features are unstable and break up to form smaller eddies. This process continues until viscous forces dominate, absorbing the energy as internal energy, rather than producing further smaller eddies. The length scale at which viscous forces dominate

completely is the Kolmogorov length scale, discussed later and given in equation 2.43. The spectra of fluctuating velocity show the distribution of energy with increasing wavenumber. The range where inertial forces dominate is called the inertial range. Here energy decreases to the power  $-5/3$  as the wavenumber increases ( $E(\kappa) = C\varepsilon^{\frac{2}{3}}\kappa^{-\frac{5}{3}}$ , where  $E(\kappa)$  is the function of energy with wavenumber  $\kappa$ ,  $\varepsilon$  is the dissipation and  $C$  a constant) [90]. As the wavenumber increases to represent smaller flow features, viscous forces start to dominate and this region is characterised by a quicker reduction in energy. An idealised spectrum with these regions labelled is shown in figure 2.3. The region at low wavenumber is called the energy containing range as the bulk of turbulent kinetic energy is carried within this region Pope [90]. Unlike the above scales, this region is dependent on the particular flow. Peaks in energy in this region should correlate with observable periodic flow features and their harmonics [90].

## 2.7 Geometric Analysis

An in-house Matlab (Mathworks) tool was written to calculate the cross sectional areas at various points through the geometry. These were calculated by intersecting planes with the geometry. The bounds of the plane were found where it met the geometry walls. These bounded planes were then used to calculate various measures from the CFD data. This process is described in algorithm 1 and figure 2.4, whilst a complete set of planes from an airway geometry is shown in figure 2.5.

These cross-sectional planes must follow the curvature of the airways to ensure they are approximately normal to the flow direction. For tube-like anatomy such as the trachea, this is done by producing a centreline using the Vascular Modelling Toolkit (VMTK) which incorporates the methods described by Piccinelli et al. [87]. This produces a series of points along the centreline with vectors tangential to the line at each point. These can then be passed to algorithm 1 as plane-normal vectors. In the complex geometry of the nose, it is not possible to generate centrelines using this method. Instead, an assumption is made that the flow will approximately follow the path of narrowest cross-sectional area. In this case, a user can draw an initial flow-path, from which positions and tangential vectors are calculated. The plane generating tool described in algorithm 1 then analyses a range of angles about that described by the user until the minimum area is found at each point. The tool also requires the airway surface and this is provided in stereolithography (STL) file format; a triangulation of the surface described by three

arrays, the triangle nodes, their connectivity and face normal vectors.

---

**Algorithm 1** Calculating the intersection of planes with an STL surface.

---

Inputs: A point on the plane, plane normal vector, STL file of the wall (magenta surface in figure 2.4).

1. Filter all nodes in the mesh to those close to the plane compared with mean triangle edge length.
2. For each remaining triangle, dot product each node with the plane normal. If the result has different signs (positive/negative) for different nodes on the same triangle, this is an element to be split (these elements are coloured green in figure 2.4).
3. Find the point of intersection between each triangle edge and the plane. This is calculated from the ratio the dot product of each centroid-to-node vector with the plane normal. The point is found at this ratio along the edge vector (blue in figure 2.4).
4. Each intersection node should be found twice, as each edge should belong to two triangles. Remove these duplicates.
5. Check for continuous regions - each triangle should share edges with two others allowing a loop to be created - several loops may be created by one slice.
6. Check if these loops represent separate parts of the mesh which cross this plane or are holes within one plane.
7. Mesh each list of nodes using MATLAB's Delaunay triangulation function, (shown in cyan in figure 2.4). This function allows the triangulation of non-convex domains if the edges are known. The edges are defined as an ordered list of node pairs on the region's boundary. All nodes are boundary nodes in this algorithm and the pairing and ordering is found in the same way as the continuity in point 5. The triangulation function will then produce a triangulation where no internal edges may cross the the boundary.
8. Calculate the area of each plane by summing the area of each triangle produced above.
9. Calculate the perimeter by summing the external edge lengths.

Outputs: STL of meshed plane, its area and perimeter.

---

In order to validate the method, slices can be reimported into software that allows

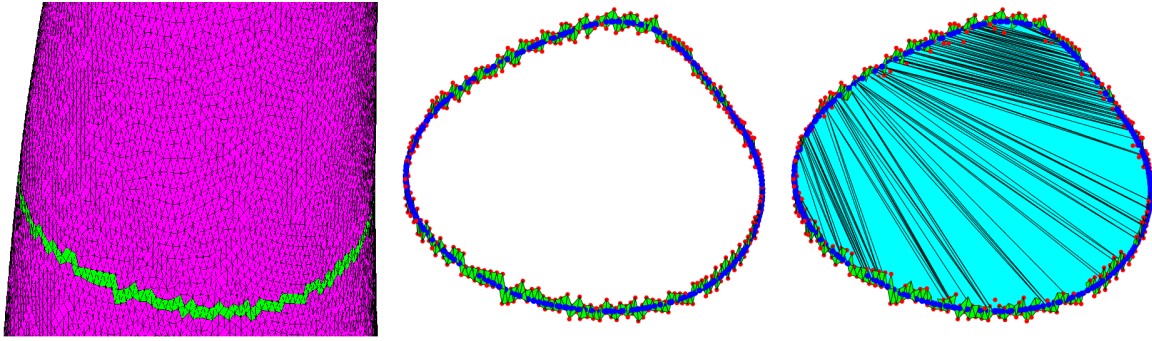


Figure 2.4: The stages in intersecting an STL surface, as described in algorithm 1. Left: Find triangles on the magenta surface which lay in the path of the plane (these triangles shown in green). Centre: Find the intersection points on these triangles' edges (blue). Right: Mesh the plane described by these nodes (cyan).

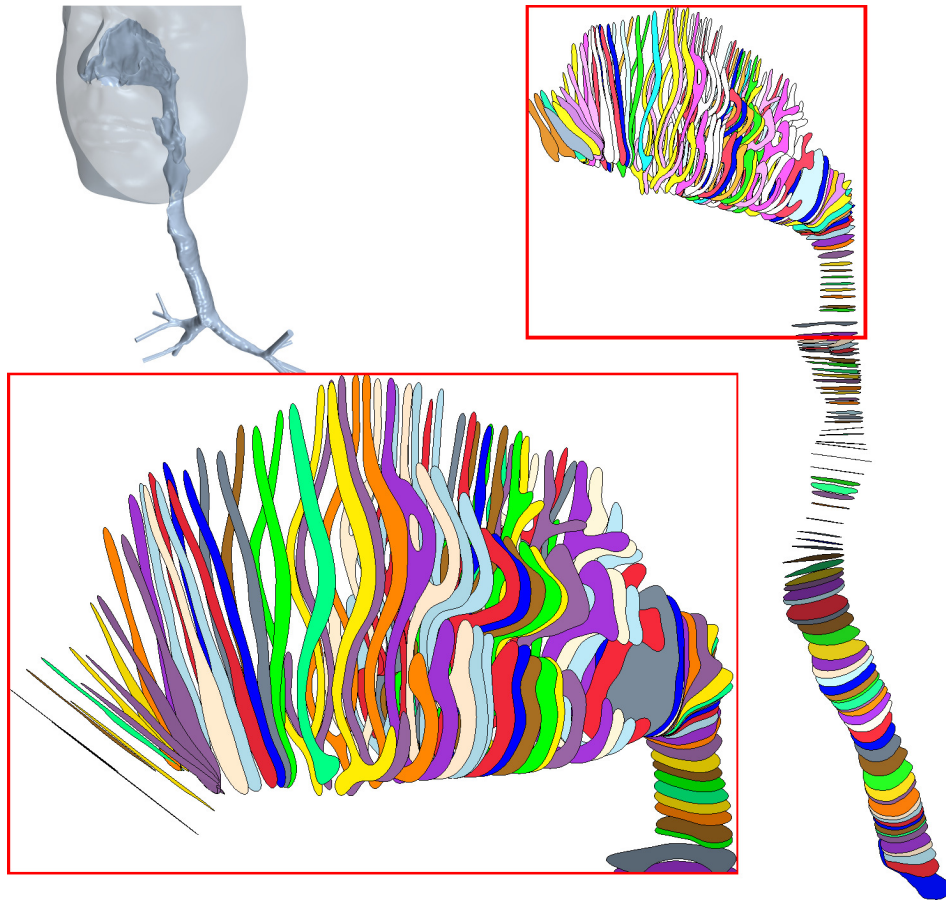


Figure 2.5: Slices through the geometry described in section 4. Top left: The anatomical surface. Right: slices at a spacing of 2 mm, with a detail of the nose shown bottom left.

concurrent viewing of medical images and STL objects, such as in figure 2.6. Here the cross-sectional plane with minimum area is compared to sagittal and coronal views from a CT scan. Visual comparison is used to validate the slices similarity to the airway region within the medical images.

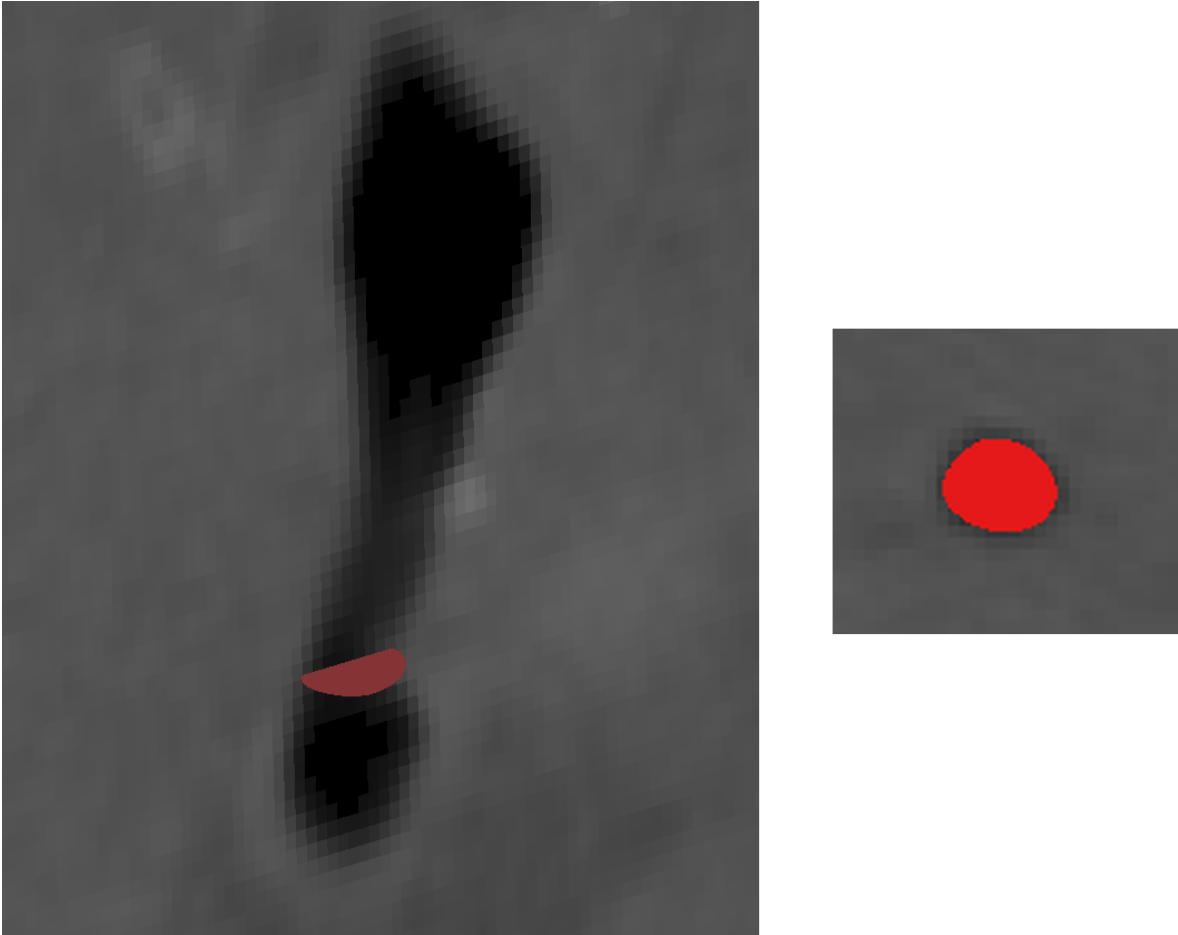


Figure 2.6: One slice (shown in red) through a trachea, compared to the original CT image in coronal (left) and axial (right) views. Image produced by R. Cetto and used with permission.

For tubular structures, such as the trachea, geometric measures such as local curvature,  $\kappa$ , defined as  $\kappa = \frac{1}{r_c}$  where  $r_c$  is the minimum local radius of curvature and the maximum inscribed sphere radius ( $r_{smax}$ ) were calculated.

In order to evaluate pathologically induced geometric changes in tracheas, the length of the constricted section,  $L_C$ , was calculated, with the constricted length defined as that with a cross-sectional area less than 65% of the first tracheal ring area. The length was then expressed as a percentage of the total of the tracheal length (first tracheal

ring to carina). 65% was chosen as it relates to the 35% reduction in 1D measurements in the current American Thyroid Association guidelines [108], assuming constriction is not uniform in all directions and is hence related to this 1D measure.

To characterise the shape of each cross sectional plane, the roundness,  $R$ , was calculated and defined as  $R = \frac{A}{r_{s,max}^2 \pi}$ , where  $A$  is the cross sectional area. This measure gives a result of one for a circular section,  $\frac{4}{\pi}$  for a square and is the ratio of the major and minor radii for an oval.

The surface area to volume ratio (SAVR) is commonly quoted in the literature (SAVR) for comparison of nasal geometries. These are calculated by surface and volume integrals on the walls or regions of interest.

## 3 Convergence and Accuracy Evaluation

### 3.1 Converging the Simulation

CFD simulations produce approximations to the *in vivo* flow conditions. Therefore, the results must be analysed to quantify the extent to which they are accurate. Measuring flow conditions *in vivo* is not practical, hence the utility of CFD simulations in the first place. There are several techniques to check the accuracy of the simulation. Firstly, one of the sources of errors in CFD simulations is that the finite resolution of the simulation means that small scale features may not be resolved. The smallest scales resolved by the simulation can be compared to the smallest scales expected in the flow (the Kolmogorov scales). Simulations which resolve all the scales (or nearly all as the energy decreases with the length scale) can therefore be used as benchmarks for less well resolved simulations and the differences in the results quantified. Coarse simulations may use modelling to account for these differences and the success of these techniques can be measured. Further validation can be performed by comparison with experimental results, which may also differ from *in vivo* conditions, but allow measurement of pressure losses for comparison with CFD simulations.

The unsteady simulation procedure gives three variables with which to improve simulation fidelity; improvements in each come at increased computational expense. These parameters are mesh resolution, the time step and the degree to which the solution is converged at each time step. Each of these variables effects different quantities of interest to different degrees, so various considerations are investigated.

#### 3.1.1 Residuals

The number of inner-iterations the simulation undergoes per time step was set based on two parameters; the residuals of momentum and continuity (and scalar transport where necessary) and the convergence of specific quantities of interest. For example, the residual,  $r$ , from the transport equation for a passive scalar,  $\phi$ , is

$$r = \frac{d}{dt} \int_V \rho \phi dV + \oint_A \rho \phi \mathbf{u} \cdot d\mathbf{a} - \oint_A D \nabla \phi \cdot d\mathbf{a} \quad (3.1)$$

and is equal to the non-zero result when all terms are put on the same side of the

equation [8]. This value is driven towards 0, with a limiting value equal to machine round-off error for each inner-iteration of every time step.

The root mean squared value ( $R_{rms}$ ) of the degree to which the discretisation equation is satisfied in each cell is given by

$$R_{rms} = \sqrt{\frac{1}{n} \sum_n r^2} \quad (3.2)$$

where  $n$  is the number of samples.

For the simulations in this study these quantities were driven as low as possible in the early iterations where large transients occur, reducing by at least twelve orders of magnitude. In later iterations approximately six orders of magnitude per time step was deemed sufficient, depending on the other resolution parameters (a simulation with a very small time step will change less between time steps).

Furthermore, various quantities of interest (overall pressure loss, velocities at points of interest) were monitored to ensure that they had converged to a stable value at each time step.

### 3.1.2 Spatial and Temporal Resolution

Convergence testing was performed on a pathological tracheal geometry which shows is affected by a goitre, since it exhibits large curvature and constriction and hence should represent the most difficult tracheal geometry on which to simulate flow. Flow is faster moving in the descending airways and therefore requires finer resolution than the nose (comparison of different simulation resolutions in the nose can be found in section 4.8).

A range of meshes were generated with numbers of elements ranging from 945,000 to 9.2 million. Quasi-steady simulations were run on each mesh with time steps of 1, 0.1 and 0.01 ms. The coarser simulations were run both without further turbulence modelling and with the LES model as shown in table 3.1.

The leftmost graph in figure 3.1 shows the temporal variation in pressure loss for the seven sets of simulations parameters described in table 3.1. Simulation a is the finest in both temporal and spatial resolution and is hence used as a benchmark to compare the other simulations against. This simulation is then evaluated to determine how close it is to a fully resolved DNS simulation in section 3.2, to justify its use as a benchmark case.

	Number of elements	Time step ( $\mu s$ )	Additional modelling
a (Fine)	9,217,771	10	None
b (Production)	2,245,514	100	LES
c	2,245,514	100	None
d	2,245,514	1000	LES
e	2,245,514	1000	None
f	974,611	100	None
g	974,611	1000	None

Table 3.1: Simulation parameters used in convergence study.

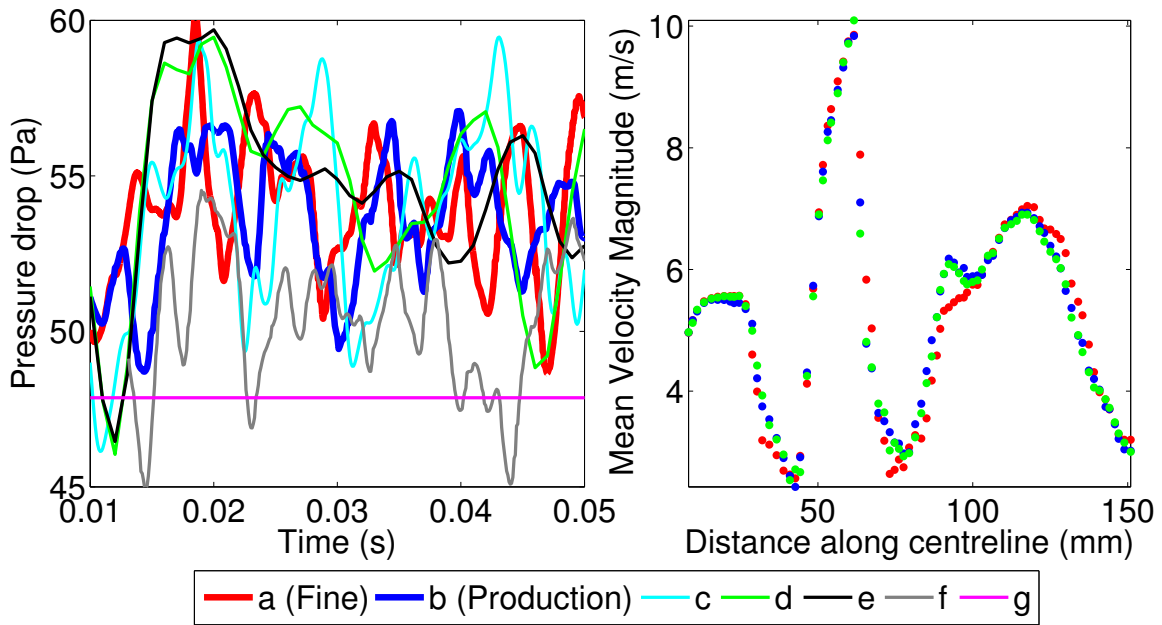


Figure 3.1: Comparison of results from different solution resolutions and modelling. Left: Pressure loss variation with time. Right: The magnitude of velocity on points along the centreline for cases a, b and d.

The following criteria were used to judge similarity in temporal variation of pressure loss between meshes b-g and a: Mean pressure loss, the dominant frequency of pressure loss oscillations (calculated by counting clear peaks in the time period of interest), and amplitude of pressure loss oscillations (and therefore temporal extremes of pressure loss variations). Each of these is tabulated in table 3.2.

Figure 3.1 and table 3.2 show that none of the simulations with time steps of 1 ms (d - green, e - black or g - magenta curves in figure 3.1) capture the temporal fluctuations

Simulation	Mean $\Delta P$ (Pa)	Amplitude of $\Delta P$ oscillations (Pa)	Approximate frequency of $\Delta P$ oscillations (Hz)
a (Fine)	53.8	6.2	312
b (Production)	53.8	6.3	312
c	53.9	9.9	312
d	54.8	8.2	188
e	54.9	4.1	156
f	50.3	5.2	343
g	47.87	0	-

Table 3.2: Comparison of pressure loss ( $\Delta P$ ) values for the seven simulations listed in table 3.1 and shown in figure 3.1.

apparent in the benchmark case (a - red curve in figure 3.1). The higher frequency oscillations have been damped out at this resolution. At higher temporal resolution, but coarse spatial resolution (f - grey curve in figure 3.1) the fluctuations are well captured, but the mean pressure loss is 5% lower than in the better refined cases. Simulations b and c share the same mesh and temporal resolution but b utilises LES modelling of smaller scales and is preferred as the additional damping supplied by the LES modelling reduced the range of the pressure loss oscillations to a similar range as in the finest case. The simulation without additional modelling (c) exhibits higher amplitude oscillations.

Several further criteria were used to judge convergence, such as mean and variance of velocity along the centreline (figure 3.1) and lines normal and tangential to the flow path (figure 3.2). Overall pressure drop and spectra of velocity fluctuations, were also considered figure 3.3. The similarity of the flow throughout the geometry can be seen in figure 6.13 (discussed in other context later) where the variance of velocity for the production and fine meshes are shown. Both resolutions exhibit similar unsteadiness throughout, in terms of patterns and magnitude of fluctuations.

Figure 3.3 shows spectra of fluctuating velocity calculated at the same point in both the fine and production simulations. Comparison between the two resolutions reveals that the LES turbulence modelling extends to the scales where the fluctuating energy has fallen by five orders of magnitude, so is within the dissipative range.

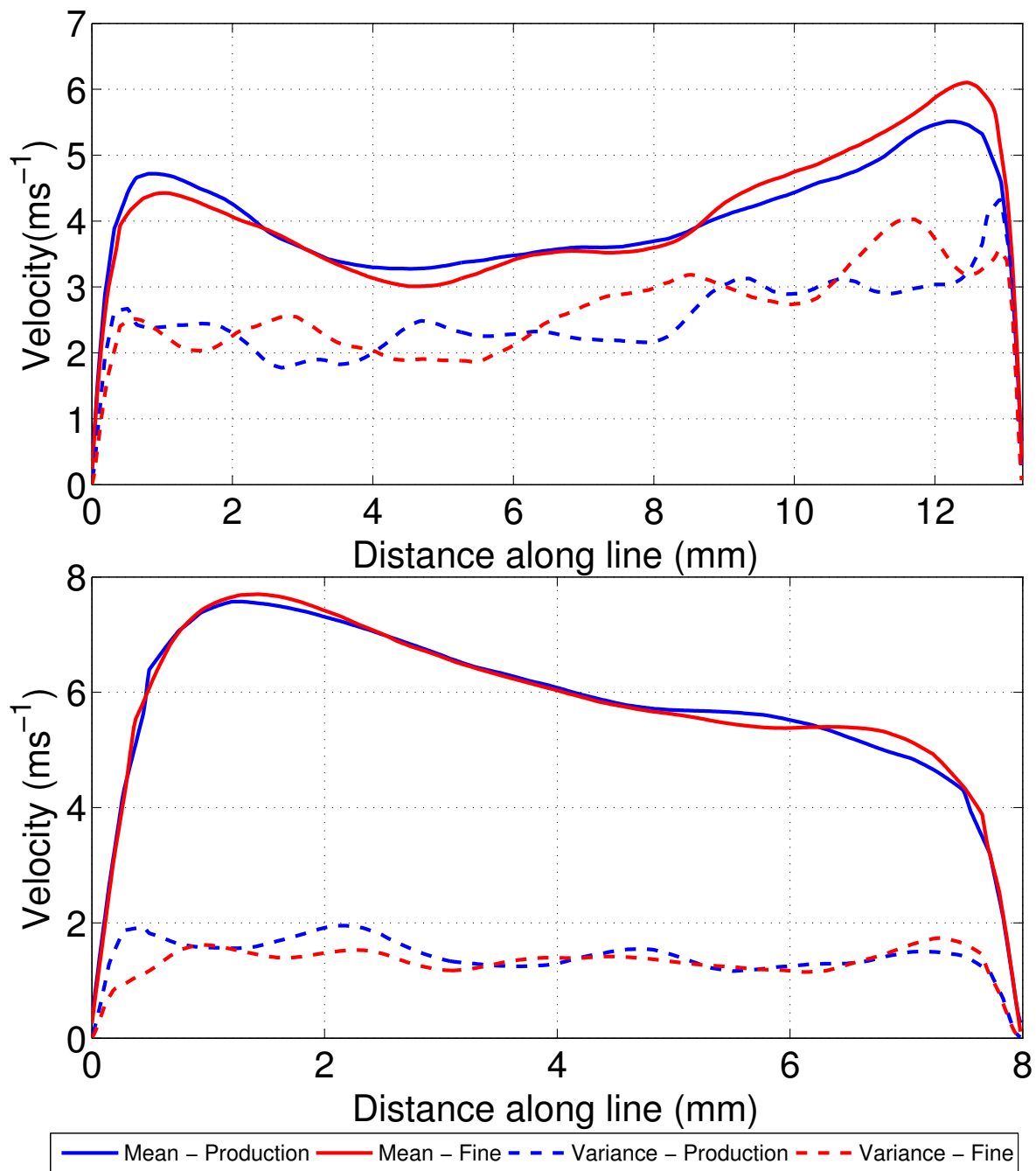


Figure 3.2: Comparison of mean and the variance of velocity on lines across geometry B normal to the flow path for the production and fine meshes. These lines are located on planes *ii* (right) and *iii* (left) from figure 6.1.

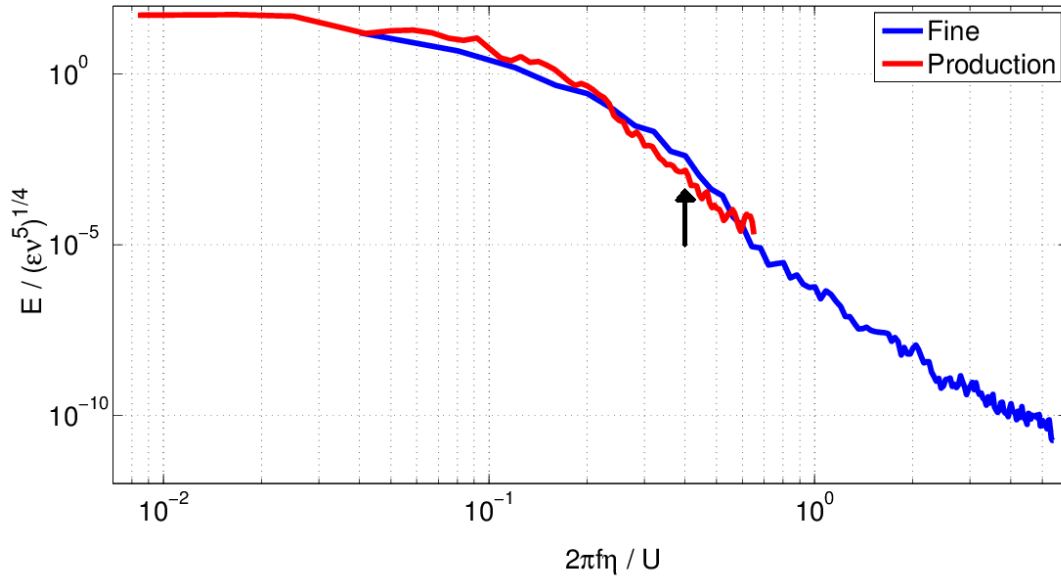


Figure 3.3: Comparison of fluctuating velocity spectra at the same point in the “fine” simulation without subgrid viscosity and the “production” simulation with LES. The energy is scaled by the dissipation,  $\epsilon$  and the kinematic viscosity,  $\nu$ . The frequency is scaled by the mean velocity at the point,  $U$  and the Kolmogorov length scale,  $\eta$ .

### 3.2 Quantifying the Captured Scales

Comparison of simulation refinement levels with the Kolmogorov estimates relies on accurate values of the viscous dissipation rate, which will vary with simulation resolution. It was found that neither quantity changed significantly in value between the resolutions, suggesting these quantities had converged sufficiently for estimates of magnitude to be obtained (figure 3.4). Nonetheless, this analysis uses values of  $\eta$  and  $\tau_\eta$  from the finest simulation as they are most accurate. The cube root of cell volume,  $\sqrt[3]{V}$  and the time step  $\Delta t$  were used as characteristic length and time scales respectively.  $\frac{\sqrt[3]{V}}{\eta}$  represents the ratio of mesh refinement level to the smallest length scale in the flow. The parameter  $\frac{\Delta t}{\tau_\eta}$  is the ratio between the time step and the smallest time scale it is necessary to resolve neglecting convection and  $\frac{U\Delta t}{\eta}$  shows how far such a feature can be convected during one time step as a ratio to the smallest scale in the flow.

The dimensionless wall distance  $y^+$  is given by

$$y^+ = \frac{yu_\tau}{\nu} \quad (3.3)$$

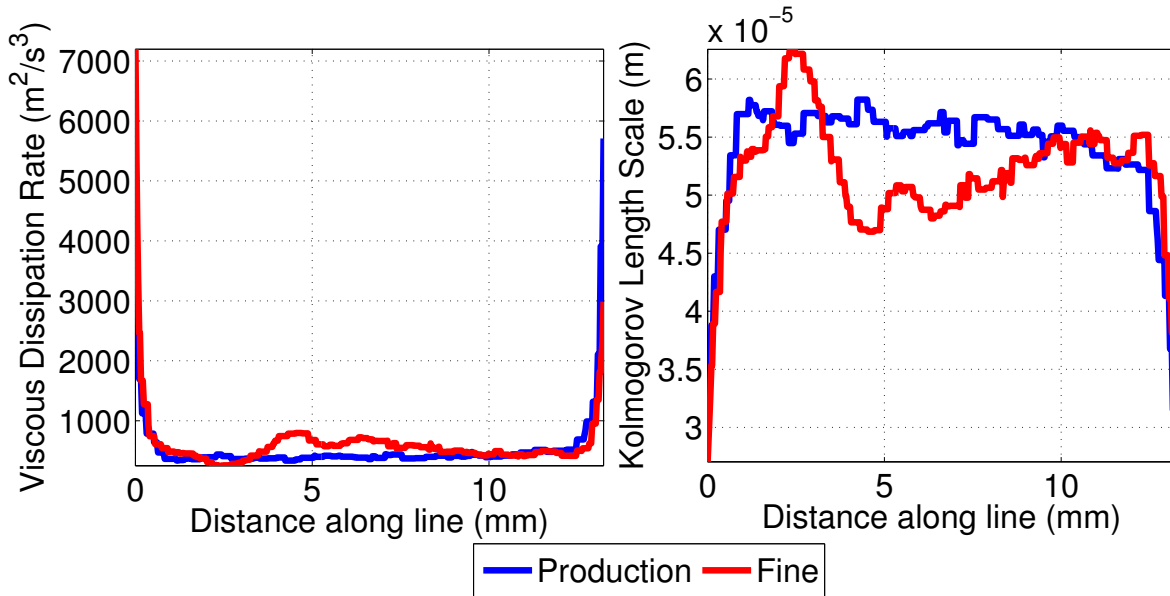


Figure 3.4: The viscous dissipation rate and Kolmogorov length scale along a line in plane *iii* (figure 6.1) from the production and fine simulations.

and is often used to determine how well the velocity gradient at the wall is captured captured [98], with  $y$  equal to the distance from the wall to the first solution point in the bulk of the flow,  $\nu$  is the kinematic viscosity and  $u_\tau$  is the friction velocity given by

$$u_\tau = \sqrt{\frac{\tau_w}{\rho}} \quad (3.4)$$

$\tau_w$  is the wall shear stress.

A temporal equivalent,  $\Delta t^+$  is given by

$$\Delta t^+ = \frac{\Delta t u_\tau^2}{\nu} \quad (3.5)$$

where  $\Delta t$  is the time step [79].

Table 3.3 shows the refinement statistics for this finest mesh, a. The Kolmogorov length and time scales were calculated as described in equations 2.43 and 2.44. These values indicate that the simulation is very well resolved in time, with both  $\frac{\Delta t}{\tau_\eta}$  and  $\frac{U\Delta t}{\eta}$  less than 1. The low values of  $y^+$  indicate that the mesh is well resolved at the wall, however  $\frac{\sqrt[3]{V}}{\eta}$  is higher than 1, showing the mesh is not capturing the smallest features in the flow. However, it is capturing all scales down to twice the Kolmogorov length scale and

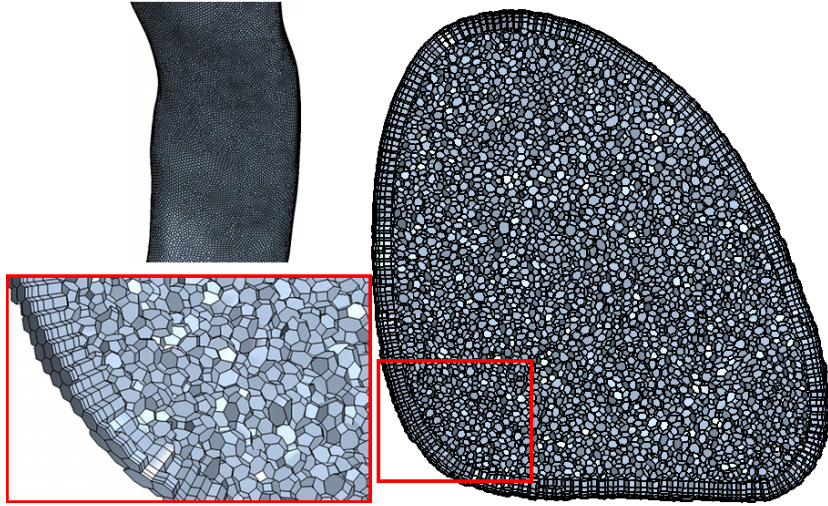


Figure 3.5: Details of the “production” mesh structure. Clockwise from top left: the surface of the trachea; all mesh elements that fall on a cross-sectional plane; a detail highlighting the prism layer mesh at the geometry wall.

there is very little energy contained below that, suggesting the simulation is close to fully resolved.

	Simulation a (Fine)
Mean $y^+$	0.096
Maximum $y^+$	0.43
Mean $\frac{\sqrt[3]{V}}{\eta}$	2.36
Mean $\frac{\Delta t}{\tau_\eta}$	0.0336
Mean $\frac{U\Delta t}{\eta}$	0.83

Table 3.3: Refinement statistics between the finest mesh simulated, a showing comparison between mesh length scales and the time step and the smallest features in the flow.

Images demonstrating the movement of flow features at five time step intervals is given in figure 3.6. It is clear that flow features only move a small amount between each image, which represents 5 time steps, therefore the motion between each time step is even smaller and the simulations is well resolved in time.

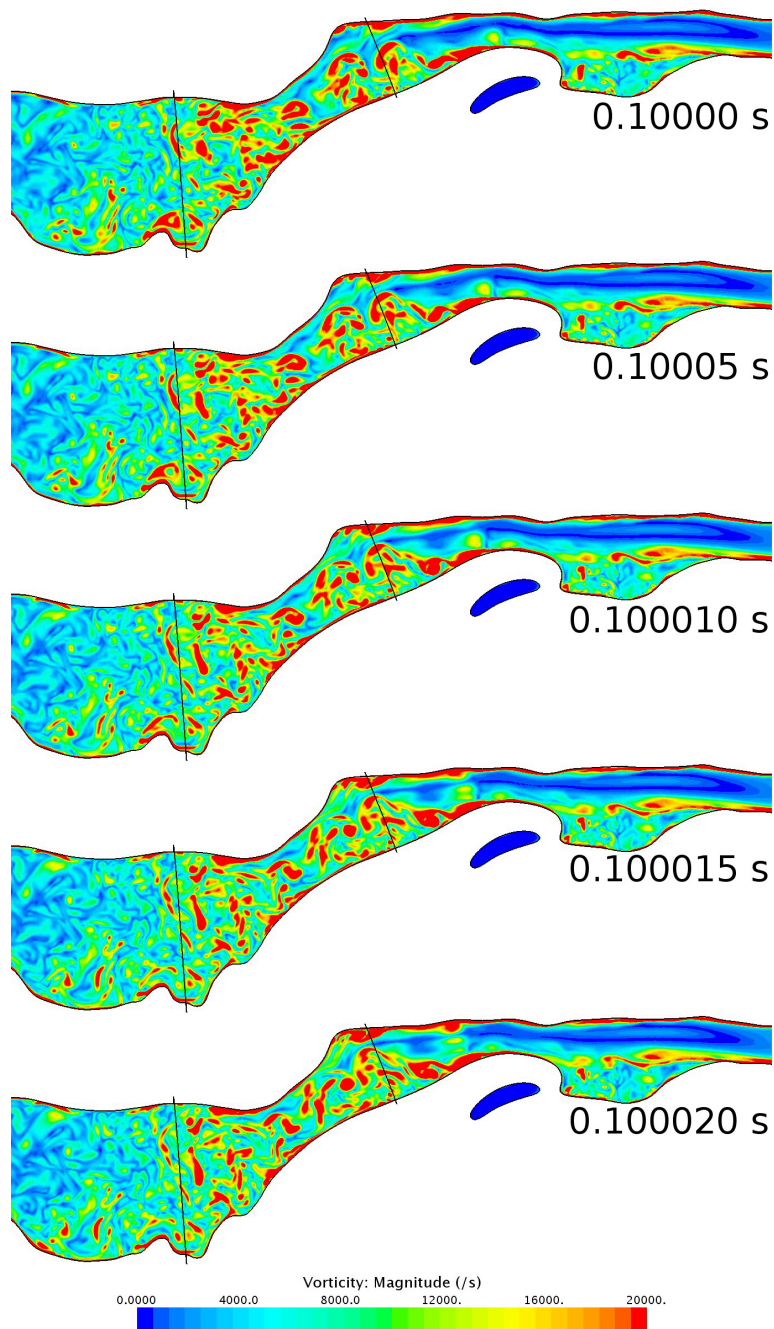


Figure 3.6: Vorticity in the pharynx at five instants, each separated by  $5 \times 10^{-5}$  s, which is 5 time steps. The small movement of each flow feature between each instant, demonstrates the high temporal resolution of the simulation.

### 3.3 Validation of Simulations by Experimental Comparison

Experimental validation of the simulations was performed using an existing model of a healthy tracheal geometry. The pressure difference between two points on the surface of a model trachea was compared to the same pressure difference determined by a CFD simulation of the same geometry with the same flow rate. The flow rate was then varied in both methods and the pressure losses compared. The variation in pressure loss with flow rate is expected to be the same for both methods, within the bounds of experimental error. The pressure loss to flow rate relationship was chosen as the variable of interest due to its ease of experimental measurement. The two points between which the pressure difference was measured were above the glottis and above the carina, providing the longest section of geometry over which comparison was possible.

The surface geometry was extruded outwards to form a volume with the inner surface representing the tracheal airway. This was then rapid prototyped in a rigid material using an Objet Connex 350 3D printer, producing the model shown in figure 3.7. The resultant geometry was then pressure tapped along its length as shown. The geometry was connected to a pump downstream of the bronchial end of the geometry and pressures measured at the pressure tap locations and across a calibrated orifice plate using an alcohol manometer. The suction of the pump was varied across the range of flow rates the pump was able to achieve (27-90 l min<sup>-1</sup>) and several measurements taken at each flow rate and a mean taken. Flow rates,  $Q$ , were calculated as

$$Q = \sqrt{\frac{2k\Delta p}{\rho}} A \quad (3.6)$$

from the pressure drop across a calibrated orifice plate  $\Delta p$ . Here,  $\rho$  is the density,  $A$  the cross-sectional area of the pipe and  $k = 0.125$ , a calibration factor for this particular orifice plate. A comparative pressure-flow plot is shown in figure 3.8a.

From 3.8a it is clear that both modalities produce similar flow rate to pressure loss relationships throughout the range of flow rates analysed. The largest uncertainty in comparing experimental and computed pressure losses was in the location of the pressure tap and its comparison to the equivalent point in the computational fluid dynamics (CFD) simulation. Figure 3.8b shows the surface variation of static pressure in geometry A at 30 lmin<sup>-1</sup>. Moving the probe 5 mm can change the recorded pressure loss by 5%.

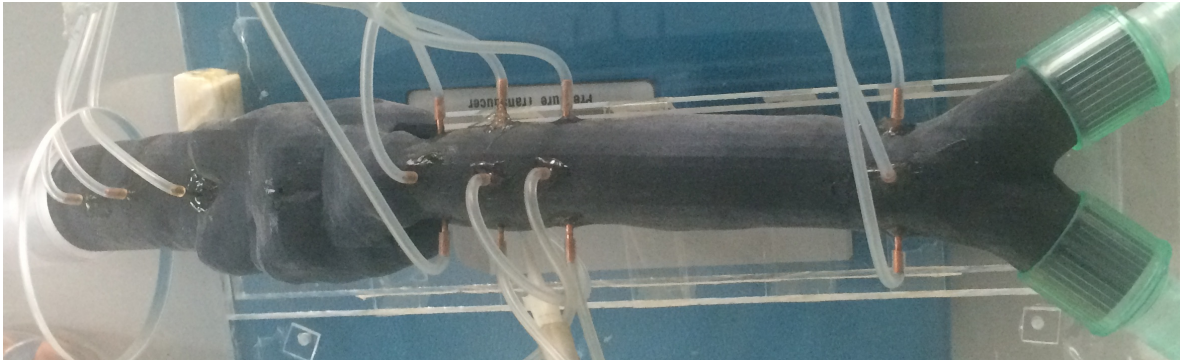
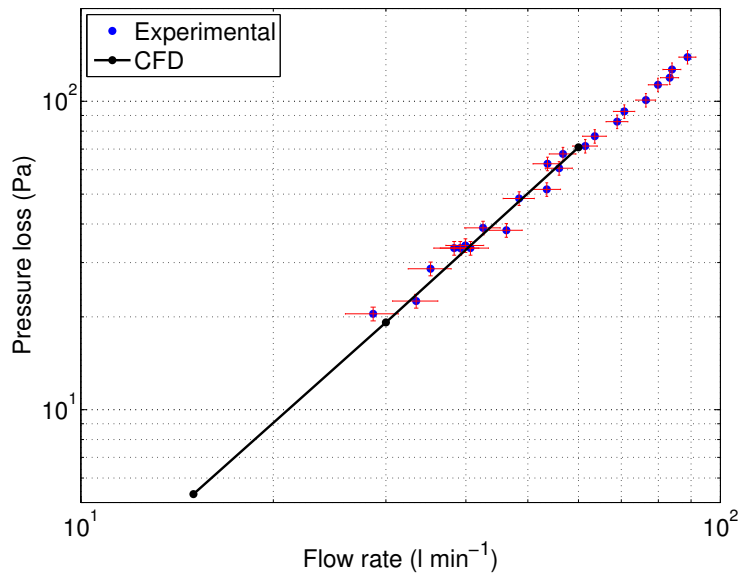
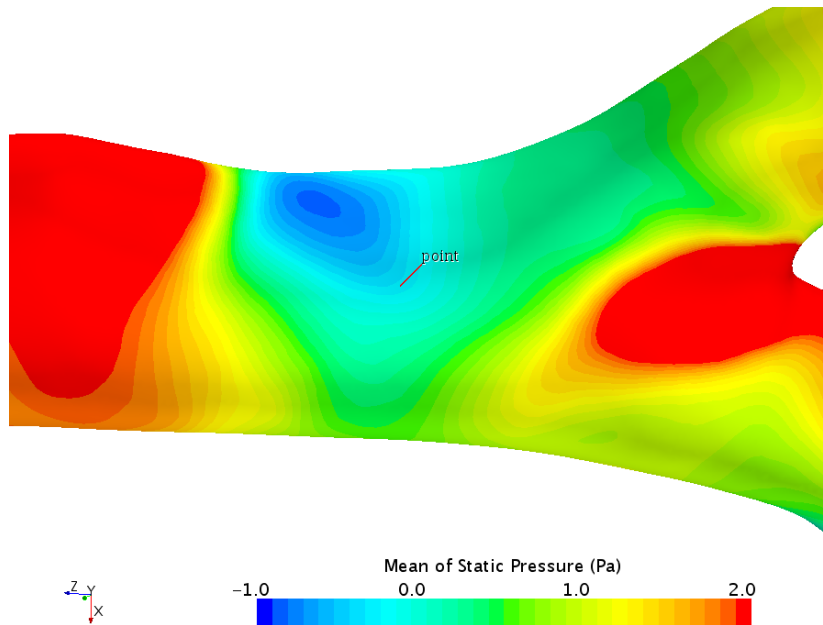


Figure 3.7: Photograph of rapid prototyped trachea with pressure taps. Flow is sucked in at the opening (left of image) and out at the two outflows (right of image).

Further losses are due to the difficulty in clearing support material used during the printing process from the lumen of the trachea and burrs from drilling the pressure taps. The pressure tapping holes are checked using an endoscopic camera, but it is difficult to achieve perfectly flush finishes. Any such surface imperfection would increase the flow speed across the probe, lowering the recorded pressure. Additionally, if the holes are not tangential to the wall, the probe may detect a component of velocity, rather than just the static pressure, with approximately 2% error in pressure recorded with a  $10^\circ$  misalignment [93].



(a) Comparison of experimental and CFD simulated pressure loss between two points on the trachea surface. The first is above the glottis, whilst the second is just above the carina.



(b) Surface contours of the mean of static pressure at  $30 \text{ lmin}^{-1}$  for geometry A. The marked point is the equivalent position to the bottom pressure tapping in figure 3.7.

Figure 3.8: Comparison of experimental and CFD simulated pressure loss.

## 4 Dynamics of a Rapid Inhalation

A high resolution spatio-temporal simulation of a rapid inhalation was performed using realistic geometry and inflow conditions. The resolution was such that the entire inertial range and much of the dissipative range was captured.

Several key metrics are investigated through the duration of the inhalation manoeuvre, including pressure losses, resistance, energy flux, velocities and turbulence quantities. The regional division of flow is also analysed. Investigation throughout inspiration shows the time scales governing these criteria and their variation with changes in flow rate. All these quantities are related to the specific flow patterns within the airways, hence detailed description of the flow pattern and how it changes through the inhalation are key to understanding temporal variation of these measures.

### 4.1 Specific Anatomy

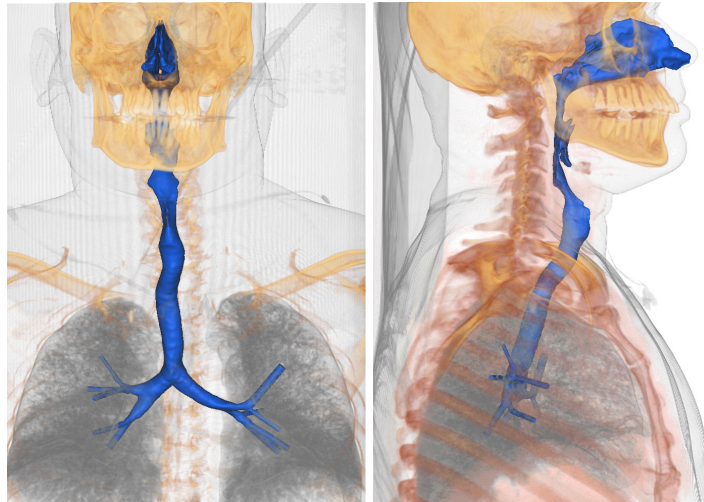


Figure 4.1: Volume rendering of neck and chest CT scan with segmented airway surface highlighted in blue.

The airway geometry was derived from a neck and chest computed tomography (CT) image set of a 48-year-old male, in the supine position. The images were enhanced with contrast and were collected retrospectively from a hospital database. The scan was requested for clinical reasons and reported to be normal. Consent from the patient for subsequent use of the data was obtained. The data was acquired using a Philips –

Brilliance 64 scanner and consisted of 912 slices of 1.0 mm thickness with a pixel size of  $0.65 \times 0.65$  mm. A consultant radiologist reported the nasal airways as clear and of normal appearance. The position of the tongue base and other soft tissues in the pharynx were deemed consistent with the patient being scanned in the supine position. The vocal cords were noted to have the appearance of being abducted, whilst the trachea was considered to be of normal dimensions, not demonstrating any abnormalities. The airway in the pharynx may be narrower than if the patient had been standing, but the geometry is within the normal range.

A small angulation of just over 3 mm of the bony nasal septum is seen projecting to the left cavity at the level of the inferior turbinate in the form of a septal spur. The resulting surface was then smoothed using Taubin's [113] algorithm (with parameters set to achieve bilaplacian smoothing) in MeshLab (Visual Computing Lab). The smoothed surface was then merged with the external non-anatomical surfaces to define the boundaries of the flow domain.

The graph in figure 4.2 shows the cross-sectional area of the airway, with the nostrils marked as plane 1 and plane 12 lying just above the carina, (i.e. where the trachea divides). The minimum cross-sectional area in the nose occurs at plane 3 in the diagram (area  $1.82 \times 10^{-4}$  m<sup>2</sup>, corresponding hydraulic diameter of  $4.94 \times 10^{-3}$  m). This plane is located slightly posterior to the nasal valve, often assumed to be the minimum area [49, 88]. In the post-septal airway, a series of minima occur in the laryngopharyngeal zone in the region of planes 8 and 9. The local area increases between these minima correspond to openings such as that into the back of the mouth and are not representative of the area utilised by the bulk of the flow; the effective flow area is closer to the minimum shown at plane 8. The glottis (plane 10) does not correspond to the minimum area airway. This is a consequence both of the vocal cords being abducted and the supine position of the subject, which results in the the tongue and soft tissues reducing airway area about planes 8 and 9.

The left and right nasal cavity airspaces are separately delineated in figure 4.2. The left nasal airspace (red curve) has a volume of 14,600 mm<sup>3</sup>, slightly larger than on the right, 12,300 mm<sup>3</sup>, (blue curve). The associated surface areas are however similar, yielding a Surface area to volume ratio (SAVR) for the left nasal airway of 0.717 mm<sup>-1</sup> and 0.827 mm<sup>-1</sup> for the right, mean 0.768 mm<sup>-1</sup>. The nasal airway volumes were measured from the nostril to a plane which extends the floor of the nasal cavity through the nasopharynx, and split in the post-septal region by another plane which is tangential

to the posterior aspect of the septum. This differs from the method employed by Segal et al. [101], who used a coronal plane at the back of the septum as the posterior marker for the nasal volume. The latter volume does not necessarily include the posterior aspect of the inferior turbinate, the size of which can have significant impact on airway volume.

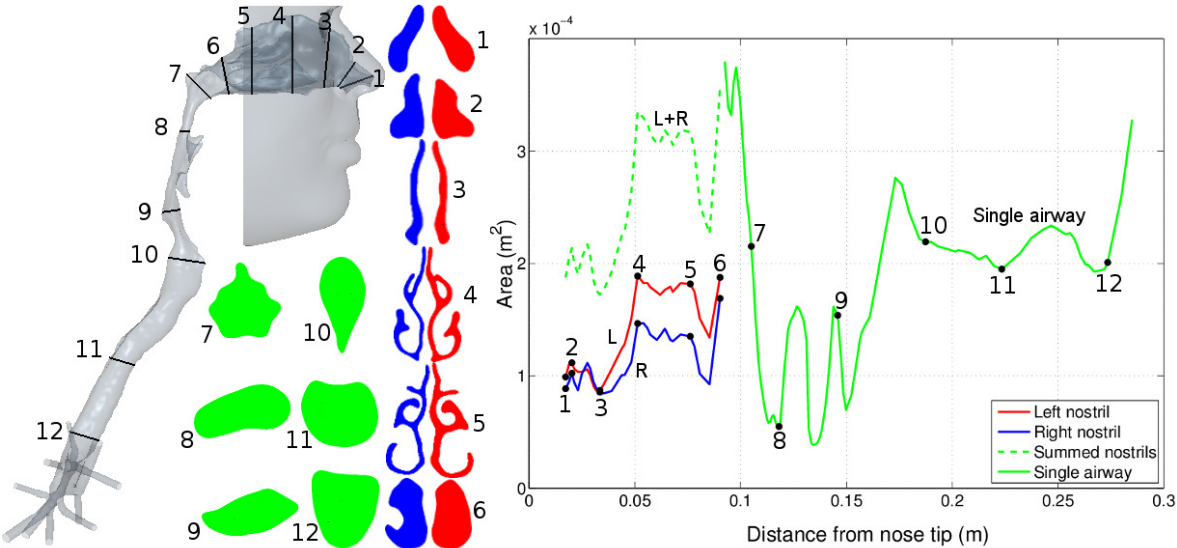


Figure 4.2: Geometry of the airway with flow-normal cross sectional areas. In the nose the area distributions are shown separately for the left and right cavities. Geometric values for each plane can be found in table A.1.

Figure 4.3 shows the position of planes selected to illustrate the dominant features of the flow.

## 4.2 Boundary Conditions

The face was placed inside a hemisphere of radius 0.5 m and flow imposed uniformly on the curved outer surface of the hemisphere, allowing a natural inflow to develop. The consequences of prescribed inflow at the nostril have been described previously by Taylor et al. [114], Doorly et al. [25]. The flat plane of the hemisphere was located approximately 0.05 m behind the chin and treated as a rigid wall; limiting the exterior airspace has negligible effect as little inhaled air originates behind the head [114]. To

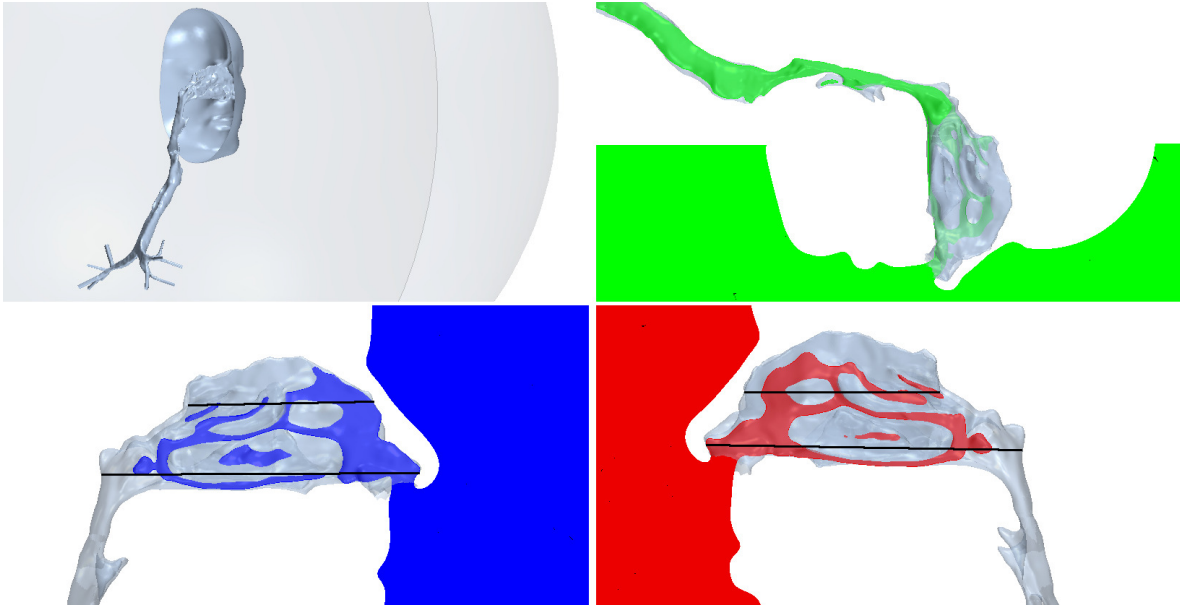


Figure 4.3: Positions of planes within the airways: Lower left - sagittal through right nasal cavity; Lower right - sagittal through left nasal cavity; Upper right - sagittal through laryngopharyngeal and glottal regions. Lower images show the positions of axial planes within the nose.

provide a well-defined outlet, the final bronchial branches were extruded into constant cross-section pipes for several diameters.

The time-varying inflow velocity was applied to the external hemisphere, whilst the ends of the extended bronchi were held at constant pressure throughout. A no slip condition was applied to the flat surface of the hemisphere and to all anatomical surfaces. No significant differences were found when (i) the radius of the hemisphere representing the external far field boundary was increased from 0.5 m to 1 m from the centre of the face, or (ii) the simulation was rerun using a prescribed pressure as an inlet condition rather than specifying the velocity (figure 4.4). The inhalation flow profile used was defined by fitting a 6th order polynomial to experimentally measured data from a previous *in vivo* investigation [91]. The raw data from which the polynomial was obtained is shown by the black curve in figure 4.5a, however some processing was performed by Rennie et al. [91] to produce the polynomial. Hot wire anemometry is not sensitive at low flow speeds due to the convection caused by the hot wire. This accounts for the black curves non-zero end values. The raw data curve was extended with constant gradients taken from the region above the convection velocity to approximate the low velocity behaviour. The 6th order polynomial used for the inlet velocity profile was generated

with a least-squares fit and is

$$V = -2.63t^6 + 4.84t^5 - 3.42t^4 + 1.17t^3 - 0.20t^2 + 0.02t \quad (4.1)$$

and is represented by the green curve in figure 4.5a. Here,  $t$  is the simulation time in seconds and  $V$  the velocity imposed on the hemisphere in  $\text{ms}^{-1}$ . Figure 4.5b shows the cumulative volume inhaled through each nostril and in total. The graph of total airflow against time is shown in green in figure 4.5a, whilst the computed left and right nasal flow rates are shown in the red and blue curves (labelled also R and L). The subject paused before the start of inhalation and at the end, so flow commences from an initial state different from that expected of a cyclic breathing pattern. This is an important distinction from cyclic breathing, as are the depth of inhalation and rapidity of acceleration [91].

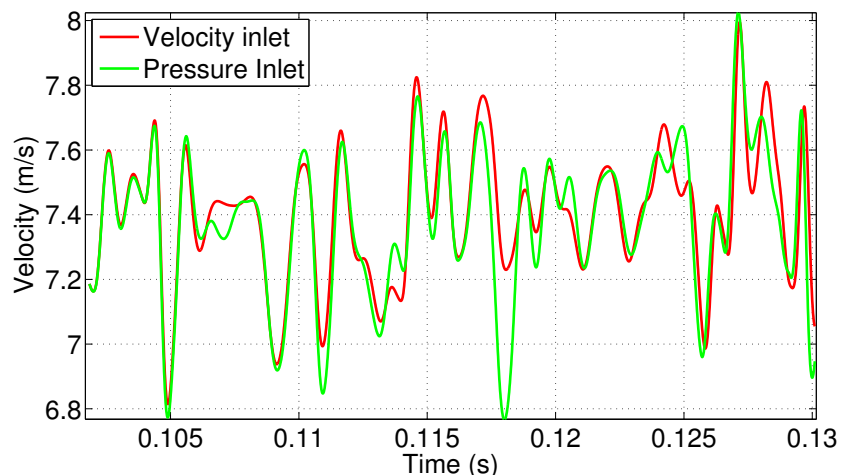
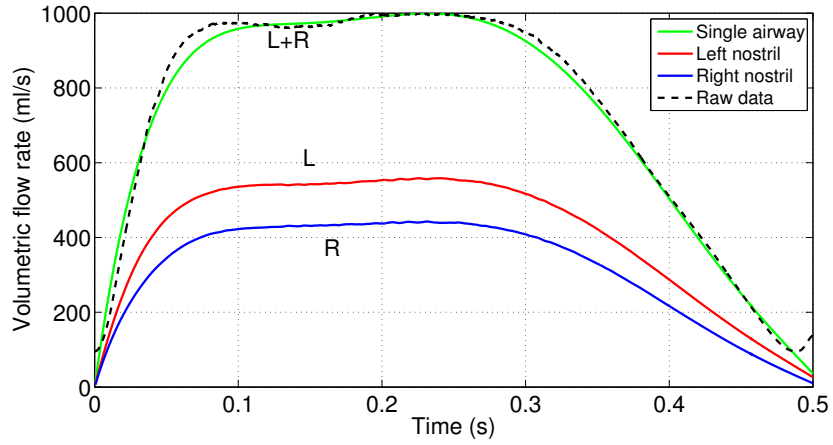


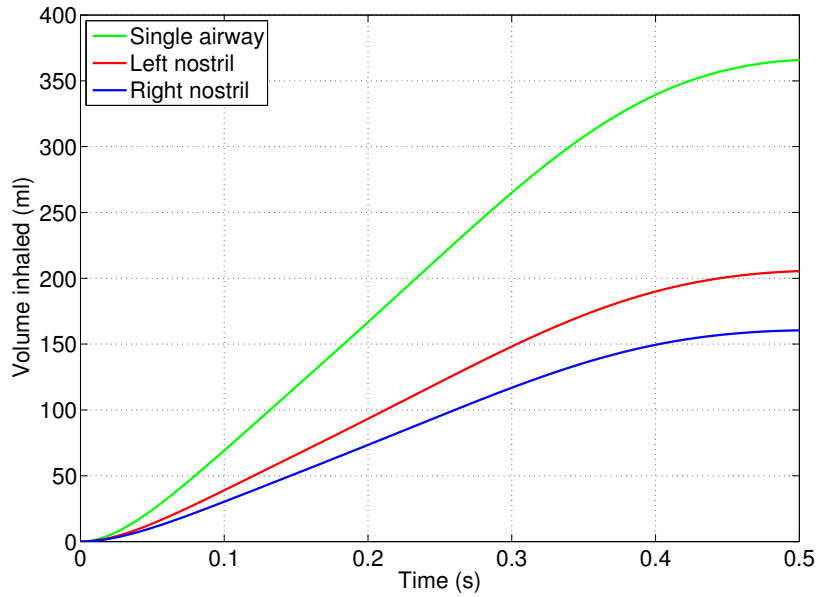
Figure 4.4: Comparison of velocity signals at a point in the nose in simulations driven by a pressure inlet (green) boundary condition and a velocity inlet (red) boundary condition.

### 4.3 Mesh Analysis

The geometry was divided into regions, with cells more densely allocated in the regions in which the flow was more disturbed. In regions such as the anterior nasal airways and



(a) Volumetric flow rate showing differences between left and right sides. The dashed black curve shows the raw data from which the green curve was obtained.



(b) Cumulatively inhaled volumes through each nostril and the unified airways.

Figure 4.5: Volumetric flow rate and cumulatively inhaled volumes over the duration of the sniff. The total flow (green curve) is applied, while the division between the two nostrils is simulated.

the larynx, nine prism layers were used with the first element from the surface having a height of approximately 0.02 mm. For cells crossing planes 2 and 3, as described in figure 4.2, the mean volume was  $2.7 \times 10^{-3}$  mm. All cells within the airways had a

volume of less than  $1.0 \times 10^{-2} \text{ mm}^3$ , although they could be much larger in the external geometry, especially far from the face. Figure 4.6 shows a cross section through the mesh in two of the refined regions, a) the right nostril and b) the glottis region.

The  $y^+$  value is less than one throughout the internal geometry. In the refined regions of the nose it has a mean value of 0.38 and across planes 9 and 10 (figure 4.2) the mean is 0.77.

The temporal discretisation of the simulation was set at  $1.0 \times 10^{-5} \text{ s}$ . This yielded mean  $\Delta t^+$  values of 0.22 in the nose and 0.92 across plane 9.

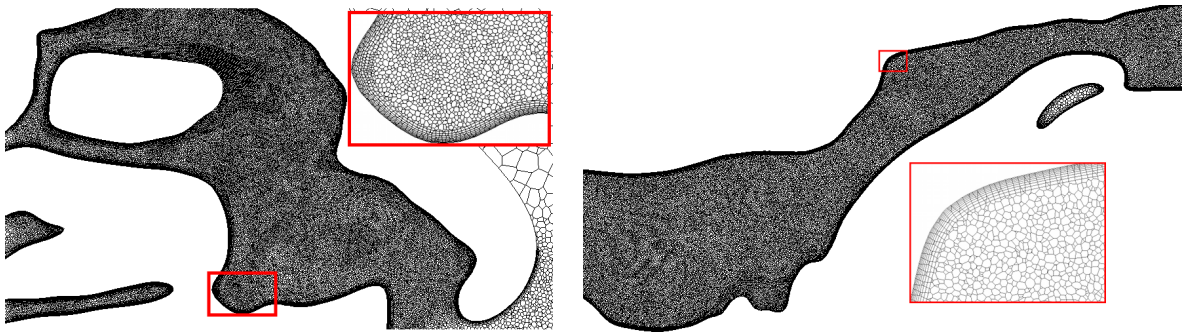


Figure 4.6: Details of the airway mesh on planes in the nose (left) and oropharynx, hypopharynx and larynx (right).

## 4.4 Flow Development

Inhaled air divides naturally between the nostrils, with that entering the left nostril (red curve, figure 4.5a) approximately 1.25 times greater than on the right (blue curve, figure 4.5a) throughout the inhalation. Integrating the flow curves yields a total inhaled volume of 364 ml, 204 ml through the left nostril and 160 ml through the right, figure 4.5b. Whilst there is more air being inhaled by the left nostril throughout the sniff, the proportions between the two nostrils varies as the sniff progresses. Figure 4.7 shows that the initial division in volumetric flow rate is exactly equal to the difference in volumes between the two sides; 54% on the left. The initial resistance to flow is purely inertial and therefore the flow division is the same as the amount of air in each cavity. However, once the flow is moving frictional losses increase and the flow further biases the left nostril (57% through the left cavity) as a result. Towards the end of the breath, the ratio changes again as recirculating regions in the right nasal cavity (discussed later) enlarge and further increase the resistance to flow in this cavity. Between 0.1 s

and 0.25 s the inhaled flow rate approximates a plateau, with corresponding Reynolds numbers in the nose (based on the hydraulic diameter of the minimum cross sectional area (plane 3))  $\sim 1900$  on the right and  $\sim 2400$  on the left; by contrast in the supraglottic region (plane 9), the Reynolds number is  $\sim 14,000$ . Figure 4.8 shows the nasal flow field on sagittal planes during the ramp-up phase (at four instants) and near flow cessation.

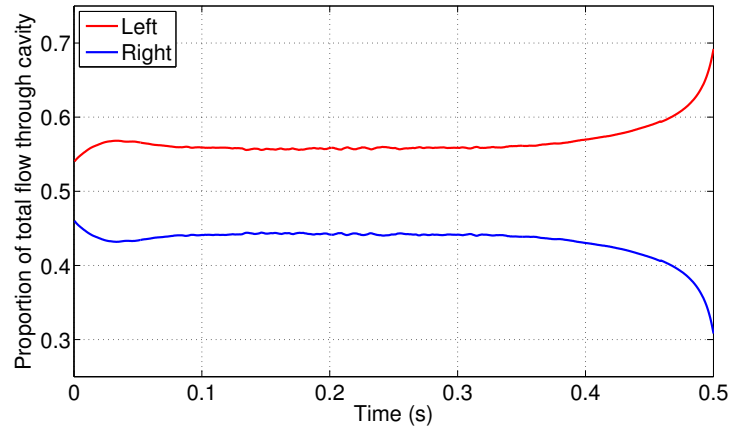


Figure 4.7: Division of volumetric flow rate between nostrils.

After 10 milliseconds elapsed time, (top) flow is at low speed ( $< 3 \text{ ms}^{-1}$ ) and attached everywhere.

After 20 ms (second pair), flow recirculation is developing in the upper anterior portion of the right cavity (note left side of figure), posterior to the nasal valve; it appears similar to that observed in the study of Doorly et al. [24] for a different geometry. No such recirculation is however apparent in the left airway. Both sides of the nose display a rapid increase in passage height after the nasal valve, but the abruptness of the increase is greater on the right, inducing flow separation.

After 50 ms, the flow pattern appears fully established in each cavity. Little further change, except in velocity magnitude, appears in the image pair at 100 ms. In the anterior region of the right cavity, the separation occupies a significant volume, acting to “block” the ingress of newly inhaled air. Flow in the left side is somewhat faster, particularly in the region of the jet formed through the nasal valve. Flow from the nasal valve appears less uniform on the right with smaller regions of fast moving flow interspersed with slower regions. Other features evident include smaller recirculation

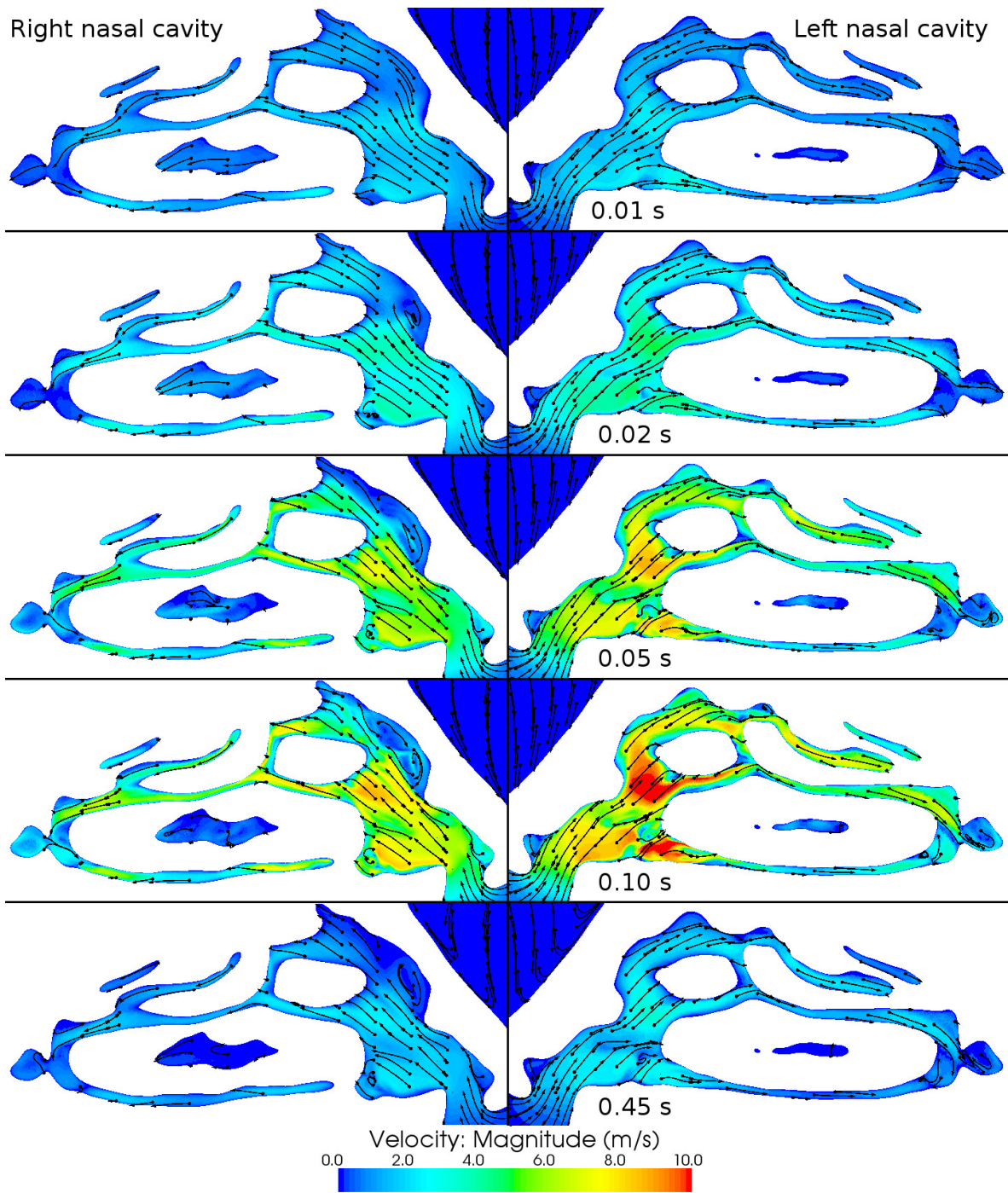


Figure 4.8: Velocity contours and planar streamlines on two planes in the right and left nasal cavities at succeeding instants.

zones in the nostril vestibules and low flow in the portions of the inferior meatus cut by the image planes. The final image pair corresponds to 0.45 s, when the total flow rate

has diminished to approximately  $250 \text{ m/s}^{-1}$ , about the same level as that in the first image pair at 0.01 s. The anterior recirculation zone has begun to enlarge and continues to grow as flow decays further; on the left flow is simply reduced in magnitude.

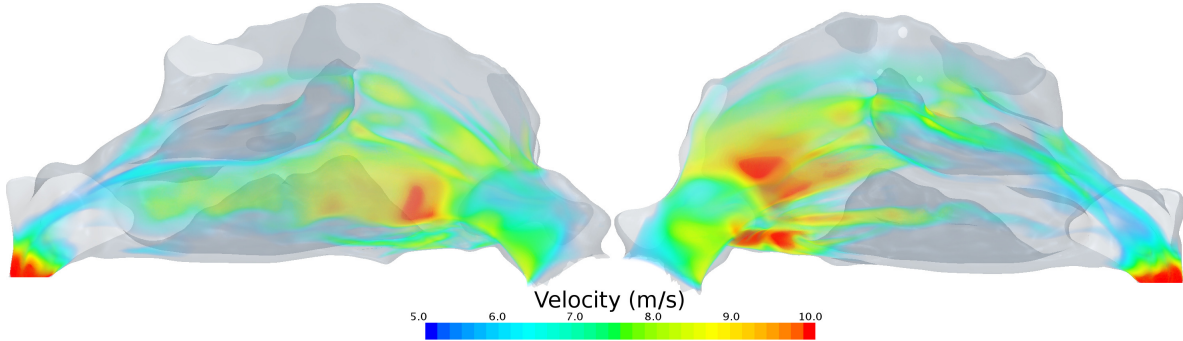
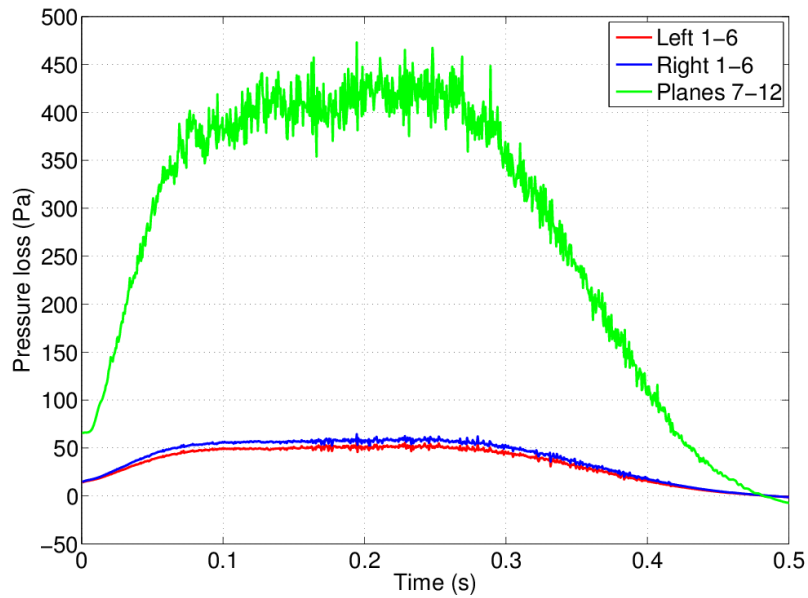


Figure 4.9: Volume renderings of instantaneous velocity field at 0.1 s in each cavity. The right nasal cavity is shown on the left and vice versa.

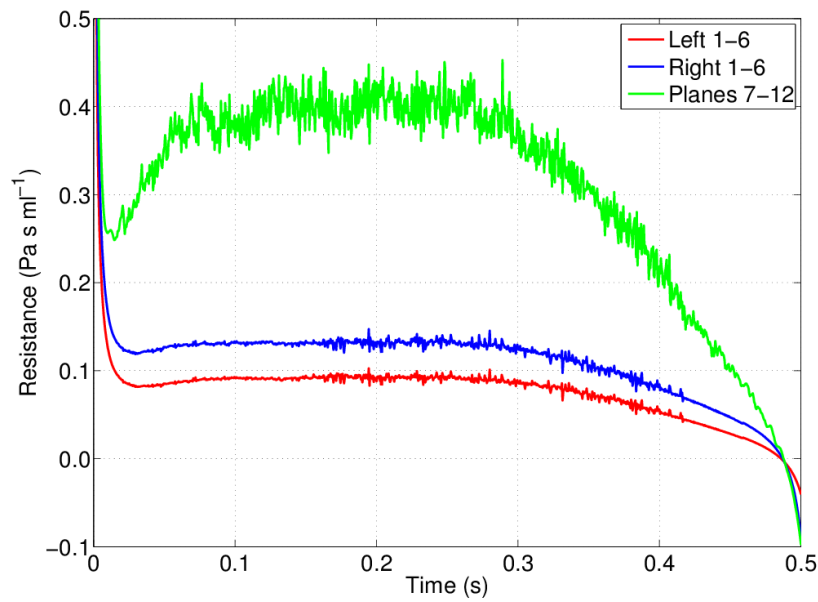
To highlight the three dimensional nature of the flow, volume renderings of the instantaneous velocity field at 0.1 s are shown in figure 4.9. The stratified nature of the flow is apparent in both cavities, as the various structures and passage shapes direct the flow into different paths. The separation in the superior and anterior section of the right nostril is again apparent by the lack of fast moving flow. The bulk of the flow is directed between the septal wall and the inferior turbinate, with just a small amount impinging on the head of the middle turbinate. By contrast, this latter route dominates in the left cavity, which is faster throughout. A strong vortex is also seen along the floor of the anterior cavity. Flow progresses higher in this cavity due to the lack of recirculation region and strong flows are seen in the middle meatus. Both sides meet posterior to the septum and here the flow is dominated by the rapid acceleration towards the oropharynx.

## 4.5 Flow Metrics

The evolution of regional pressure loss and airway resistance, defined as total pressure difference divided by flow rate is compared for the transnasal airspaces (planes 1-6) and the descending airway (planes 7-12) in figure 4.10. In steady flow, the resistance depends only on flow rate. The inhalation profile considered involves significant flow acceleration up to 0.1 s, which requires an additional transient pressure gradient. At 0.05 s, the left transnasal pressure loss is approximately 39 Pa, but rises to approximately 50 Pa at



(a) Pressure loss across each nasal cavity and the descending airways.

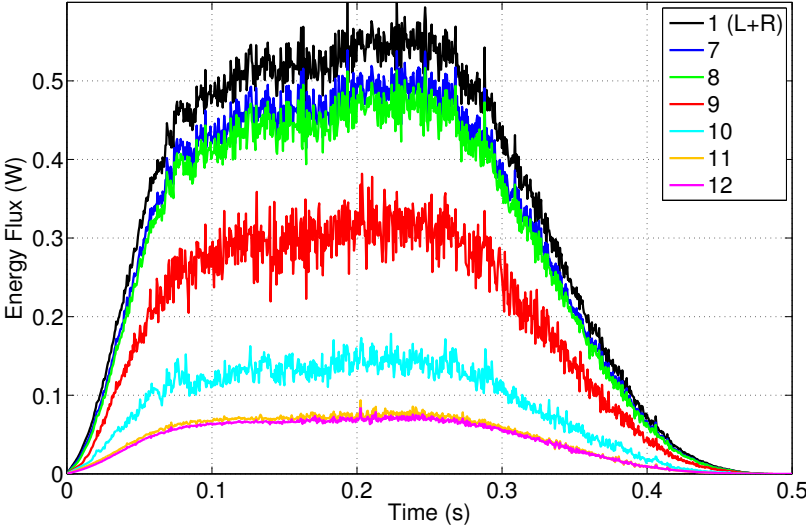


(b) Comparison of transnasal and descending airway resistances.

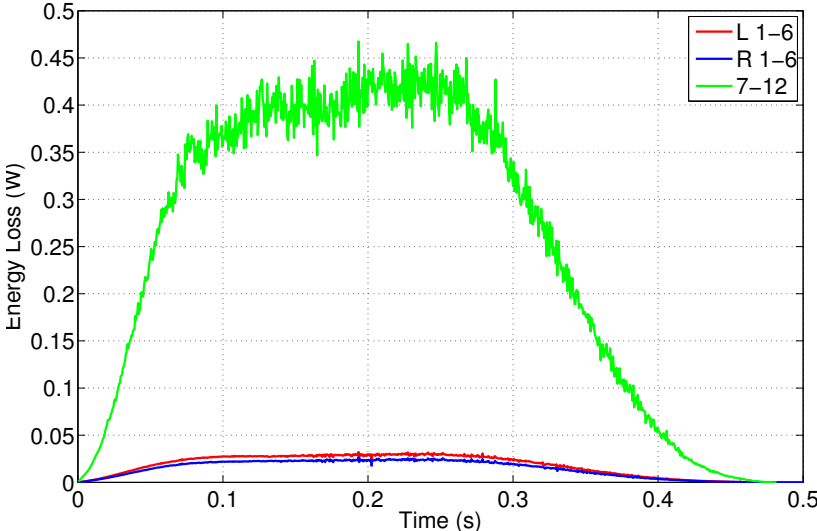
Figure 4.10: Pressure loss and resistance during a sniff.

0.1 s. However the resistance is virtually unchanged, as the component needed for an acceleration that is diminishing happens to be balanced by that needed to drive

an increasing flow. The same does not occur in the descending airway, which is the dominant resistance for the subject, due to the reduced area in the oro- and hypopharynx.



(a) Energy fluxes through the planes described in figure 4.2.



(b) Energy losses through regions of the airway delineated by the planes in figure 4.2.

Figure 4.11: Energy fluxes through planes during a sniff.

Figure 4.11a shows the energy flux, calculated using equation 2.36 across the nostrils (plane 1) and the six planes in the descending airways (figure 4.2). The energy flux through the nostrils is represented by the black curve. The highest fluxes occur at peak

flow rate,  $\sim 0.1$  to  $\sim 0.27$  s, with the energy reducing more quickly than flow rate due to the cubic relationship between them. The energy lost in traversing various regions of the airway can be seen in the distances between the curves. There is very little energy loss between planes 1 and 7 (hence the intermediate planes are omitted) and in the turn between planes 7 and 8. The highest losses occur either side of plane 9, in the narrow regions through the oropharynx and above the glottis. In the trachea, more energy is lost in the superior section, between planes 10 and 11 as it contains strong mixing regions than in the inferior section where the losses are minimal. The total energy losses across each nasal cavity and the entire descending airway are shown in figure 4.11b, whilst integrating the energy flux loss between each pair of consecutive planes (defined in figure 4.2) as in equation 2.37 produces the total energy loss in each region, figure 4.12.

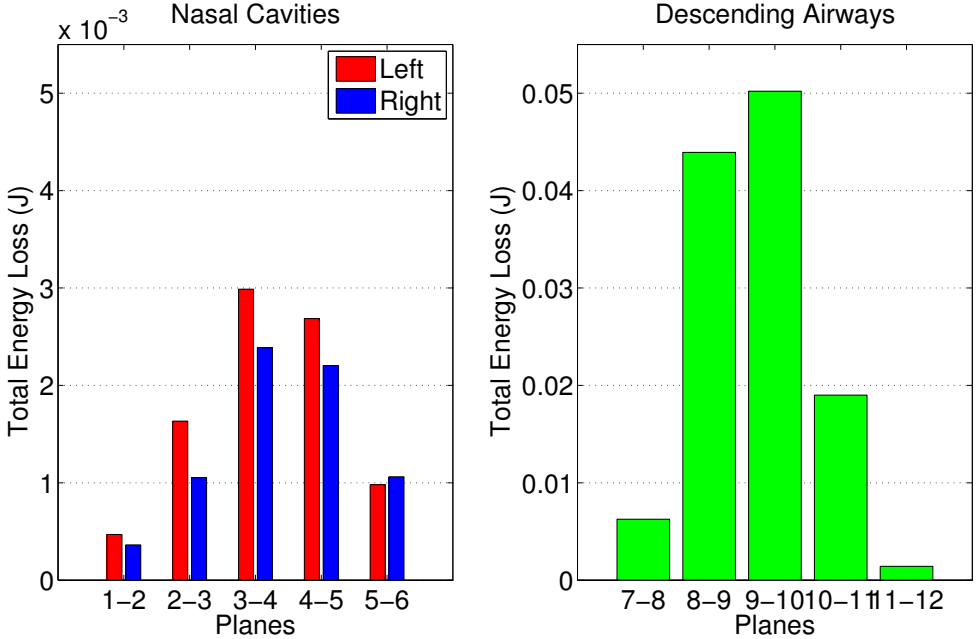


Figure 4.12: The total energy loss between each pair of consecutive planes (shown in figure 4.2) over the duration of the sniff. The energy scale for the descending airways (right) is ten times higher than that for the nasal cavities (left).

## 4.6 Patterns of Flow: Nasal Flow Division

The architecture of the nose partitions the flow into separate streams to best accomplish physiological functions such as heat and water exchange [29] and sampling of inhaled

air by the olfactory receptors. Airflow partitioning during inhalation was quantified by computing the flux through different sectors of nasal plane 4 (see figure 4.2). Plane 4 lies in the turbinate region and is subdivided into sectors referred to as the upper and lower medial and lateral quadrants in figure 4.13. The division between the upper and lower regions was effected by positioning a plane oriented in the axial direction between the middle and inferior turbinates, so that the plane did not touch either structure. Asymmetries in the turbinates on either side of the nose slightly displaces this division on the left side relative to that on the right. The cross sectional areas of each section are shown as percentages of each side's total in figure 4.14.

In figure 4.13 the graphs indicate how the partitioning of flow in each cavity varied during the inhalation. Three distinct stages in the dynamics of the flow split are apparent; initiation, equilibrium and decay.

In the right cavity, after approximately 0.03 s, the flow split equilibrates. On the left it appears to take almost twice as long. In both cases it is somewhat surprising that the equilibrium flow balance is established quickly, despite the flow having attained only approximately 50% of its peak and whilst still accelerating. However, most of the gross changes in flow pattern occur within this period as shown in figure 4.8. The initiation process sees the potential flow-like pattern change once the nasal valve jet develops and recirculation zones appear where the flow separates. The time scales for these events depend on the length scales of local features; in this part the time is broadly comparable to the 50 ms required for the inhalation to fill a volume equivalent to that of the nose.

As flow initially accelerates, the jet entering the nasal cavity strengthens, diverting more flow to the upper regions and around the middle turbinate, rather than along the floor of the nasal cavity. This accounts for the rapid rise of flow to the upper regions on both sides of the nose during the establishment phase.

Minor fluctuations in the proportions of flow directed through the various sectors reflect local unsteady disturbances at peak flow rates. The manner in which the flow streams are divided differs between left and right sides, despite the division of the nasal airspace yielding quadrants of proportionately similar size on left and right (figure 4.14). On both sides the bulk of the flow passes along the medial side of the respective cavity, i.e. along the septal wall; this accounts for 73% of the flow at equilibrium in the right nostril and 66% in the left. However, the divide between the flow transiting upper versus lower regions is different: on the right, 60% of flow favours the lower regions, whilst on the left, 60% favours the upper. This effect seems to be linked to the flow pattern

illustrated in figure 4.8, where the recirculation zone in the right nostril prevents flow to the upper regions, causing a bias of flow to the lower regions. With no separation in the left nostril, flow appears more evenly spread between the various divisions.

Deceleration of the flow commences after 250 ms, but the flow divisions do not change until later, perhaps 400 ms. Even then there is little change until the final few tens of milliseconds when certain features developed in the initial phase of the flow alter, whilst the inertia of the nasal jet continues to direct air to the upper reaches of the nose increase those regions' share of flow.

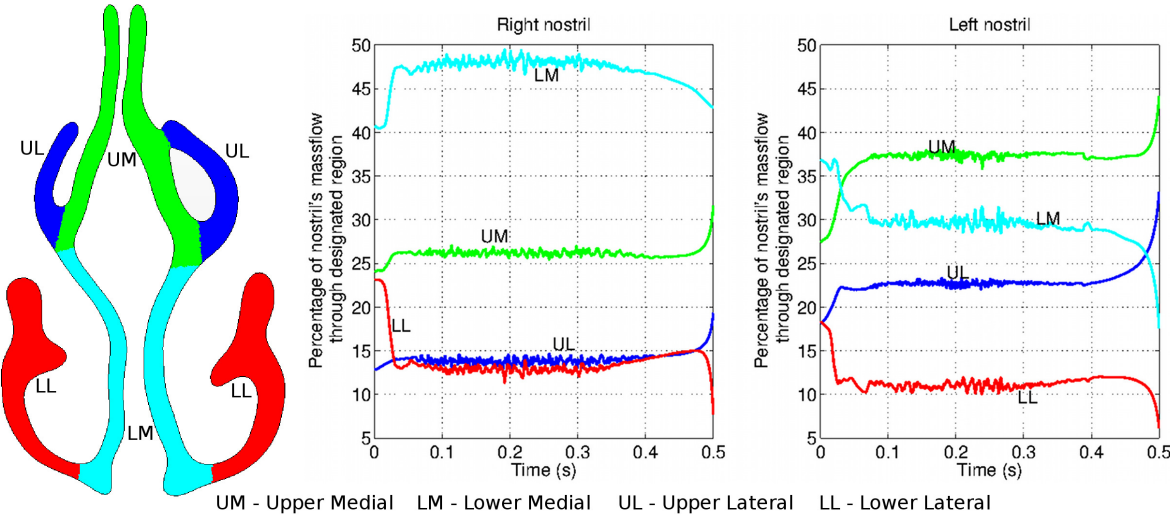


Figure 4.13: Mid-nasal cavity (figure 4.2, plane 4) regional cross-sectional area division and corresponding flow distribution.

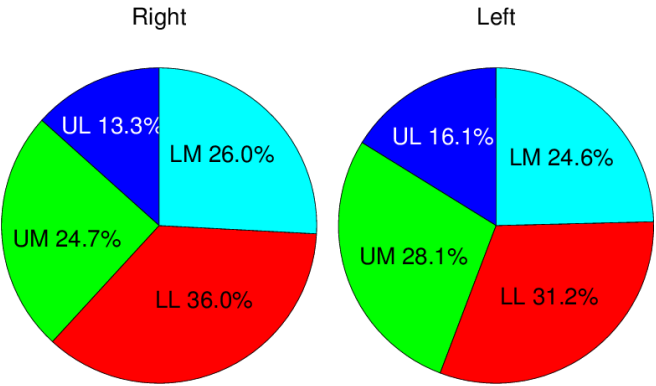


Figure 4.14: The regional division of cross-sectional area as per the sectors shown in figure 4.13.

## 4.7 Patterns of Flow: Unsteadiness and Turbulence

Spontaneous fluctuations associated with turbulence develop earlier in the glottic region than in the nose, in line with the near order of magnitude greater Reynolds number. This is evident in figure 4.15, where samples of velocity magnitude are compared for a point on plane 10 within the glottal region (red curve) with those from a point on the sagittal plane in the right nostril, halfway between planes 2 and 3. In the nose, flow speed increases calmly until 0.07 s (corresponding flow rate  $\sim 900 \text{ mls}^{-1}$ ) then oscillations of relatively small amplitude appear; these diminish as flow decays and are absent after 0.35 s (flowrate  $\sim 750 \text{ mls}^{-1}$ ).

Flow in the laryngeal region becomes unsteady after 0.02 s, by which time the local mean airspeed reaches around  $6 \text{ ms}^{-1}$ . There the oscillations persist, merely reducing somewhat towards flow cessation.

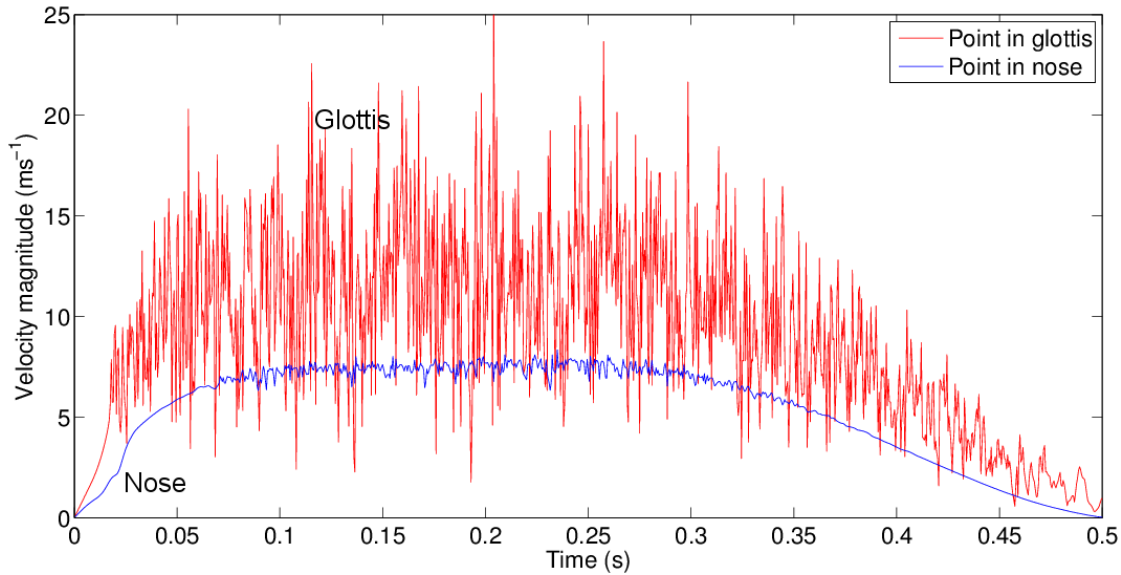


Figure 4.15: Flow velocity signals at two points: lower curve - point in the right nasal cavity towards the top of the intersection of the right sagittal plane (figure 4.3) and plane 3 (figure 4.2); upper curve - point in the glottis at the intersection of the sagittal plane (figure 4.3) and plane 10 (figure 4.2).

Figure 4.16 shows the mean velocity,  $V_{\text{mag}}/V_{\text{ref}}$  and the fluctuating velocity,  $V'_{\text{mag}}/V_{\text{ref}}$  across two sagittal planes, one in each nostril, whilst corresponding quantities for the supraglottic region are shown in figure 4.19.  $V'_{\text{mag}}$  is defined as the square root of the

variance of the velocity magnitude and is proportional to the square root of turbulent kinetic energy (TKE). These quantities are calculated over a 30 ms window of the sniff, starting at 0.1 s, when flow approaches a plateau. The reference velocity taken for normalisation in the nose, ( $V_{\text{ref, nostrils}} = 3.52 \text{ ms}^{-1}$ ), is obtained by taking the spatial and temporal mean of velocity on plane 4 (figure 4.2) during the 30 ms window.

Mean velocities appear higher and more uniform in the left nasal cavity than the right. The right cavity shows regions of fast moving flow negotiating the obstacles of the septal wall and turbinates, with a separation region in the anterior portion of the right nostril. Plots of  $V'_{\text{mag}}$  also reveal flow on the right to be more unsteady than on the left, other than at the head of the middle turbinate in plane 4 where the septal spur is located. It is noteworthy that in the nose, regions of significant fluctuation appear localised and quite different between the two sides.

The exterior flow is sink-like and laminar in nature. The flow in the left cavity remains largely laminar in the anterior region, although there is evidence of transitional flow on the right side, especially around the break down of the nasal-valve jet (where the sagittal plane crosses plane 3.)

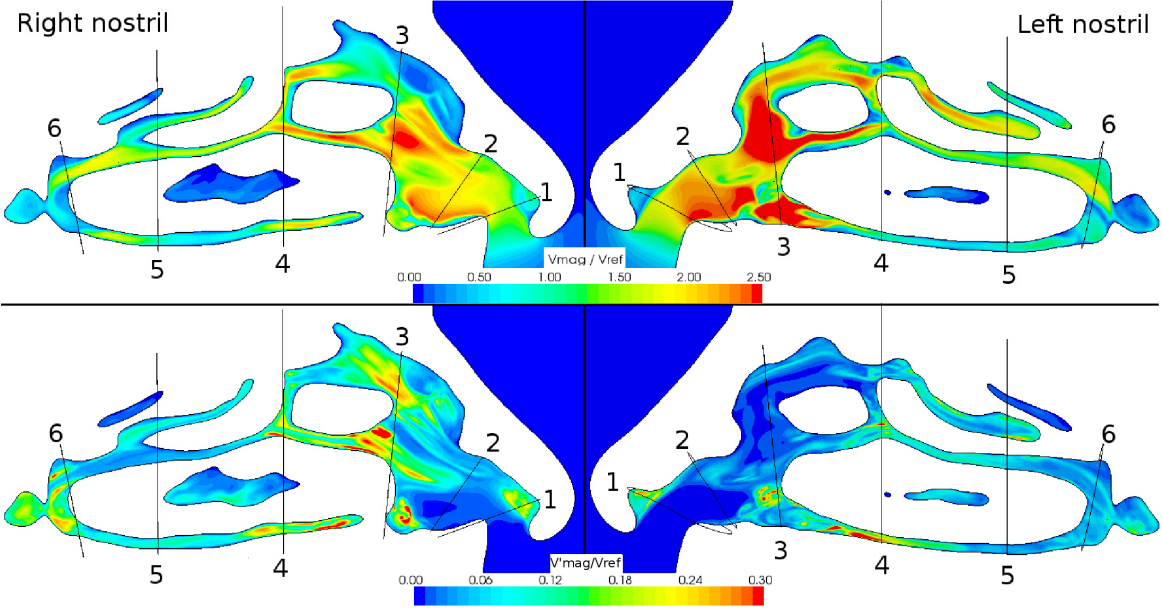


Figure 4.16: Mean  $V_{\text{mag}}$  (upper) and  $V'_{\text{mag}}$  (lower) in the nose at peak flow, scaled by local reference velocities.

Flow in the cross-sectional planes 3 and 4 in the nose and at planes 9 and 10 in the

descending airway are compared in figure 4.18. Comparing left and right cavities at plane 3, in the upper region of the right cavity  $V_{\text{mag}}$  is low, whereas  $V'_{\text{mag}}$  is high, due to the unsteady recirculation in this zone. Plane 4, positioned at the head of the middle turbinate and slightly posterior to the septal spur reveals some unsteadiness in flow on the left. The right nostril flow is concentrated in the lower medial section, along the septal wall, whereas flow on the left is more uniformly distributed with highest velocities around the head of the middle turbinate. Downstream of this cross-section, the flow in the nose appears calmer, as the passage traversed is more uniform in shape until the nasopharynx.

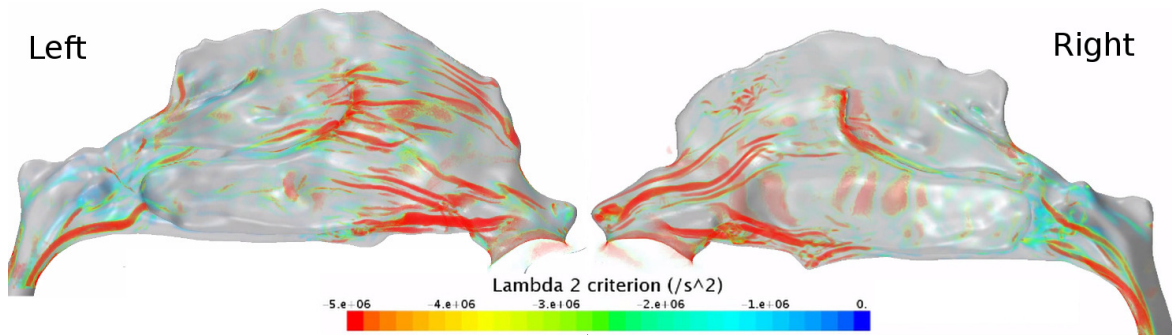


Figure 4.17: Instantaneous structures of  $\lambda_2$  in both nasal cavities at 0.13 s. This figure is shown with the left and right cavities on the opposite sides to other figures as here the septal wall has been removed to show the structures interaction with the turbinates.

Figure 4.17 reveals the vortical structures within both nasal cavities. The right anterior recirculation is apparent, as seen throughout this analysis. In the equivalent region in the left cavity, several flow-wise streamers indicate the flow is still attached here. Both cavities indicate vortices originating in the nasal vestibule and these appear higher up in the right side, perhaps contributing to the separation at the nasal valve. Both exhibit strong vortices along the floor of the cavity. The left cavity has a large number of small structures impacting on the head of the middle turbinate, these structures fluctuate with time, explaining the small oscillations seen in the mass distribution figure (4.13). Few structures exist in the inter-turbinate region, but new ones form posterior to the inferior turbinates on both sides, the so-called “dorsal” vortices described by Zhao and Jianj [128]. There are two of these in the right cavity with the upper originating at the middle turbinate, this feature does appear in the left cavity, but is much weaker.

Flow in the supraglottic region (figures 4.18 and 4.19) is dominated by the jet issuing from the constrictions through the epiglottis and the back of the tongue. Here, the

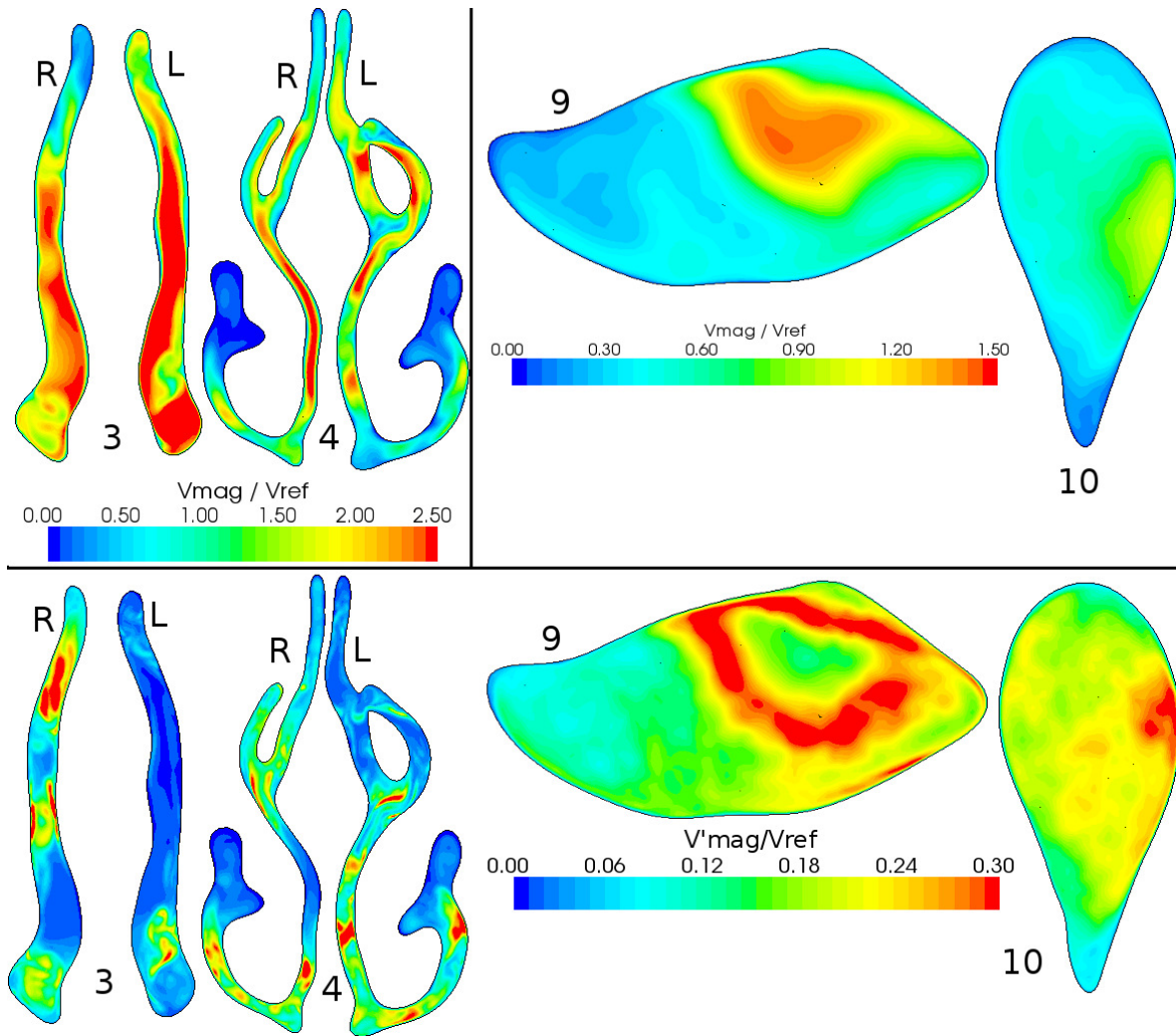


Figure 4.18: Through-flow  $V_{\text{mag}}$  (upper) and  $V'_{\text{mag}}$  (lower) velocities in anterior and mid nasal cavity (figure 4.2, planes 3 and 4) and supraglottic and glottic regions (figure 4.2, planes 9 and 10).

normalising value,  $V_{\text{ref}} = 17.7 \text{ ms}^{-1}$ , corresponds to the average velocity at plane 8. At plane 9, flow effectively bypasses much of the available airway area. The peak fluctuation intensity can be seen in the plots of figures 4.18 and 4.19 to occur at the margins of the jet. Direct comparison of the flow in this region with idealized problems, such as the mildly eccentric stenosis considered in Varghese et al. [116] is difficult, given that the airway is a more complex shape and the inflow is highly disturbed.

Elevated values of  $V'_{\text{mag}}$  at plane 10 point to the continued high fluctuation amplitude as the jet impinges on the side wall. By plane 11 (not shown) the fluctuations are much reduced as the flow fills the trachea more uniformly. Summary values of the fluctuation

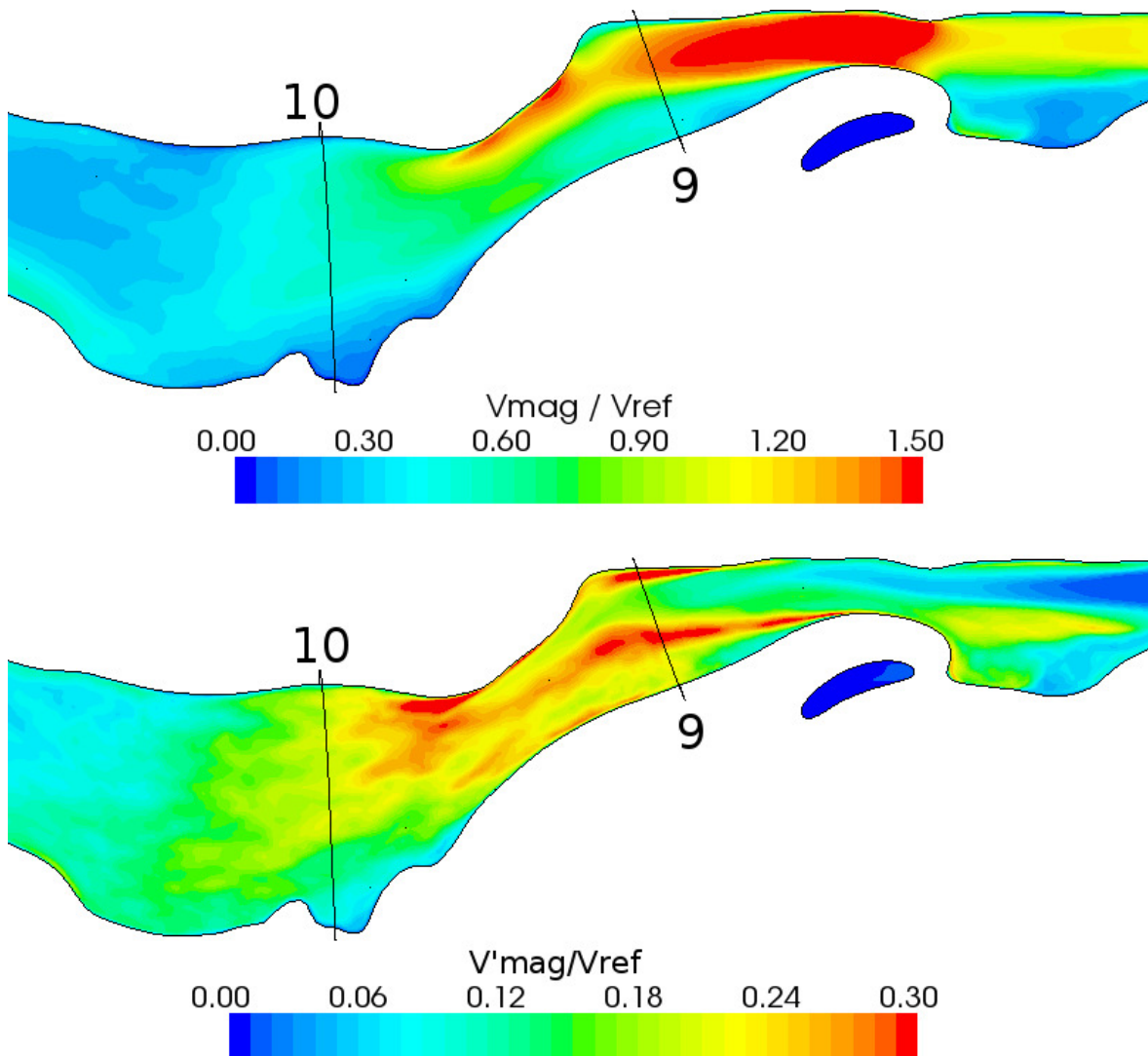


Figure 4.19:  $V_{\text{mag}}$  (upper) and  $V'_{\text{mag}}$  (lower) in the oropharynx, hypopharynx and larynx at peak flow, scaled by local reference velocities.

intensity integrated over the various cross sectional planes are shown in table 4.1, comparing the magnitude of velocity fluctuations and the turbulence intensity, defined as the ratio of a representative fluctuation velocity to the mean flow velocity. Hahn et al. [39] reported experimentally determined values of turbulence intensity (equation 2.35)  $T_u$  in the range 1.5-5% at point locations in the nose. This measure is subject to large variations in regions with low mean flow values, however.

The rich detail of the flow that lies behind the unsteadiness is revealed by plotting the instantaneous magnitude of vorticity (defined as the curl of the velocity field) in the

Plane	$V_{mag}(\text{ms}^{-1})$	$V'_{mag}(\text{ms}^{-1})$	$T_u\%$
1 (L - R)	5.6 - 5.5	0.11 - 0.13	4 - 3
2 (L - R)	6.4 - 5.9	0.06 - 0.10	1 - 1
3 (L - R)	7.2 - 5.8	0.13 - 0.39	1 - 7
4 (L - R)	3.5 - 3.4	0.30 - 0.31	9 - 9
5 (L - R)	3.5 - 3.5	0.22 - 0.17	5 - 5
6 (L - R)	3.6 - 3.2	0.20 - 0.50	5 - 5
7	4.9	0.36	6
8	17.7	0.47	2
9	10.8	3.37	22
10	8.8	3.39	24
11	5.3	0.88	11
12	5.2	0.64	8

Table 4.1: Mean values of velocity and turbulence quantities on planes defined in figure 4.2 in the period 0.1 - 0.13 s.

nose and in the supraglottic region, figure 4.20. The arrow in the right nasal cavity (top) points to breakup of the shear layer at the margin of the anterior recirculation. The pair of arrows in the supraglottic region (bottom) highlight successive shear layer instabilities, demonstrating the complex inflow condition for the downstream jet.

Figure 4.21 highlights the flow features through the superior section of the descending airways. The first image shows the post-turbinate vortex dissipates in oropharynx. New  $\lambda_2$  structures form at the top of the epiglottis and extend through the hypopharynx. These structures then dissipate in the superior section of the trachea. The second image also shows  $\lambda_2$ , but coronally and focuses on the region of jet impingement and the rich structures formed. Comparison with the rendering of velocity in the third image shows flow-wise streamers in the shear layer at the edge of the jet, with a more complex pattern in the impingement zone. This image also shows the skew of the jet, also seen in figure 4.18. The final image shows the distribution of high velocity regions throughout the trachea.

The perturbations of velocity and vorticity fields at 0.13 s are shown in figure 4.22. These are defined in equation 2.20. The flow is made up of a mean which advects these perturbations downstream over time. The quasi-regular pattern of these fluctuations indicates an underlying temporal pattern assuming the mean velocity is relatively constant during the traversing period. The perturbations at this instant are most intense in the expansion above the glottis, in contrast with the instantaneous vorticity field

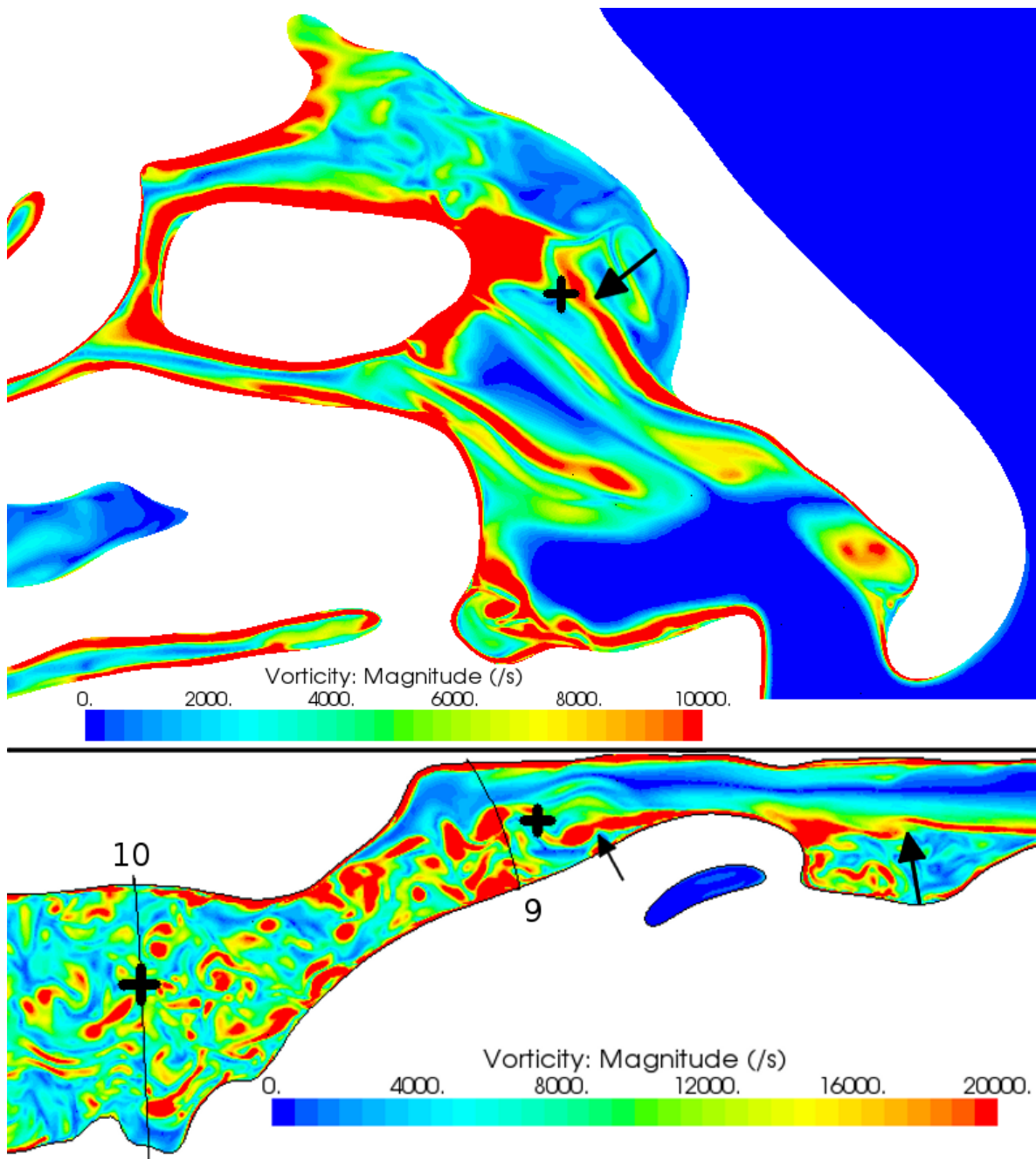


Figure 4.20: Contours of vorticity magnitude on sagittal planes in the right nasal cavity (upper) and oropharynx, hypopharynx and larynx (lower). The arrows illustrate shear layer instabilities. The black crosses illustrate the points at which the spectra in figure 4.25 are calculated.

shown in figure 4.20, where the highest values are seen in the constriction, perhaps showing the mean values are higher in this latter region. Comparison with figure 4.19

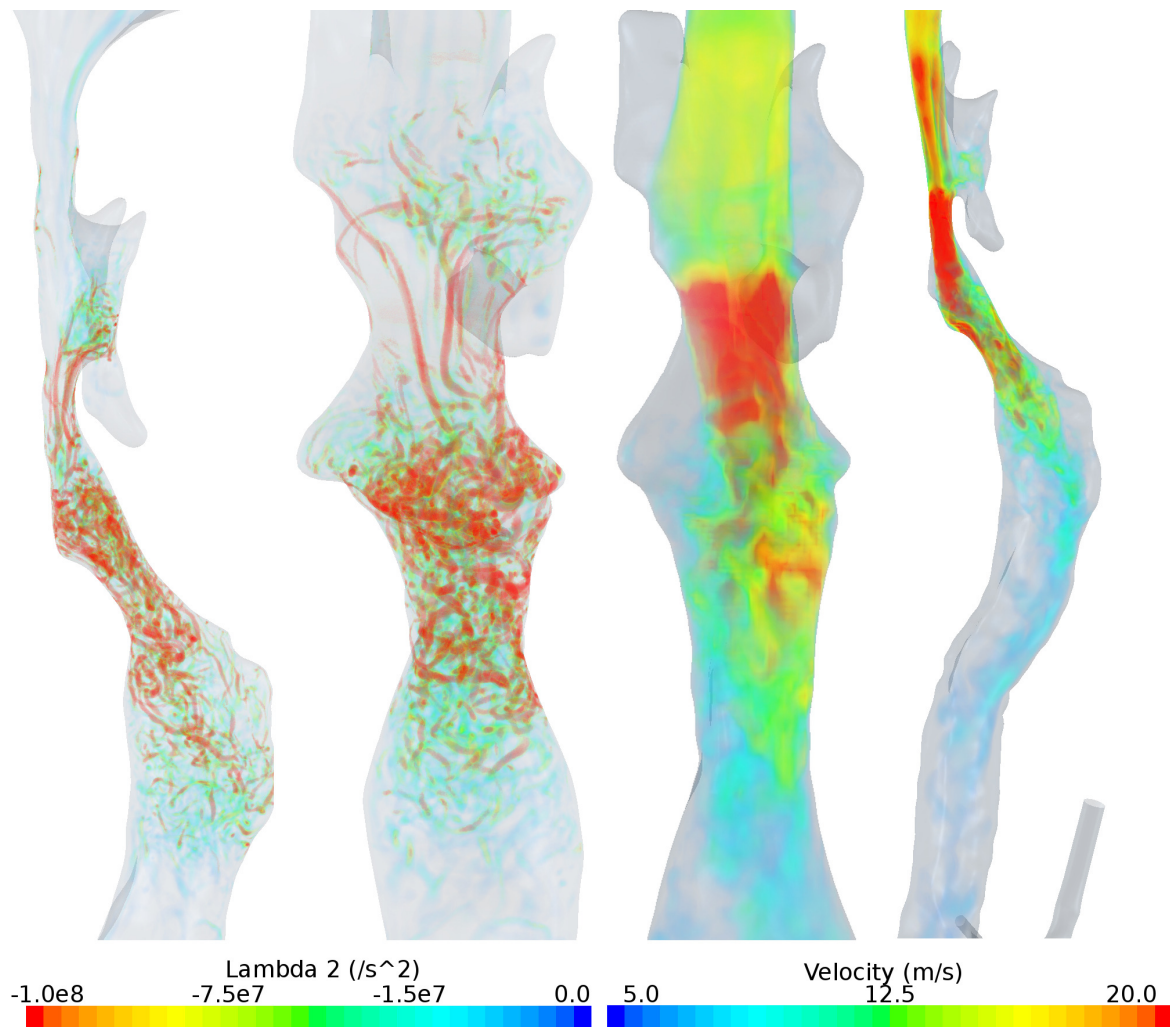


Figure 4.21: Volume renderings of instantaneous  $\lambda_2$  (left pair) and velocity (right pair) showing the supraglottal jet and the structures associated with its formation and impingement. Images are shown at different scales to highlight particular flow features as described in the text.

reveals a large region of high fluctuating velocity in the expansion, demonstrating that these instantaneous perturbations are representative of the temporal dynamics of the flow.

The black line in figure 4.22 represents a series of points over which these temporal fluctuations are plotted, figure 4.23. Distance along the line is measured from the superior end of the line. The line is not well aligned with the flow direction in this region, but some propagation along it can be seen in the diagonal angle of the flow features seen in the distance-time surface plots. From this angle, a propagation speed of 14.46

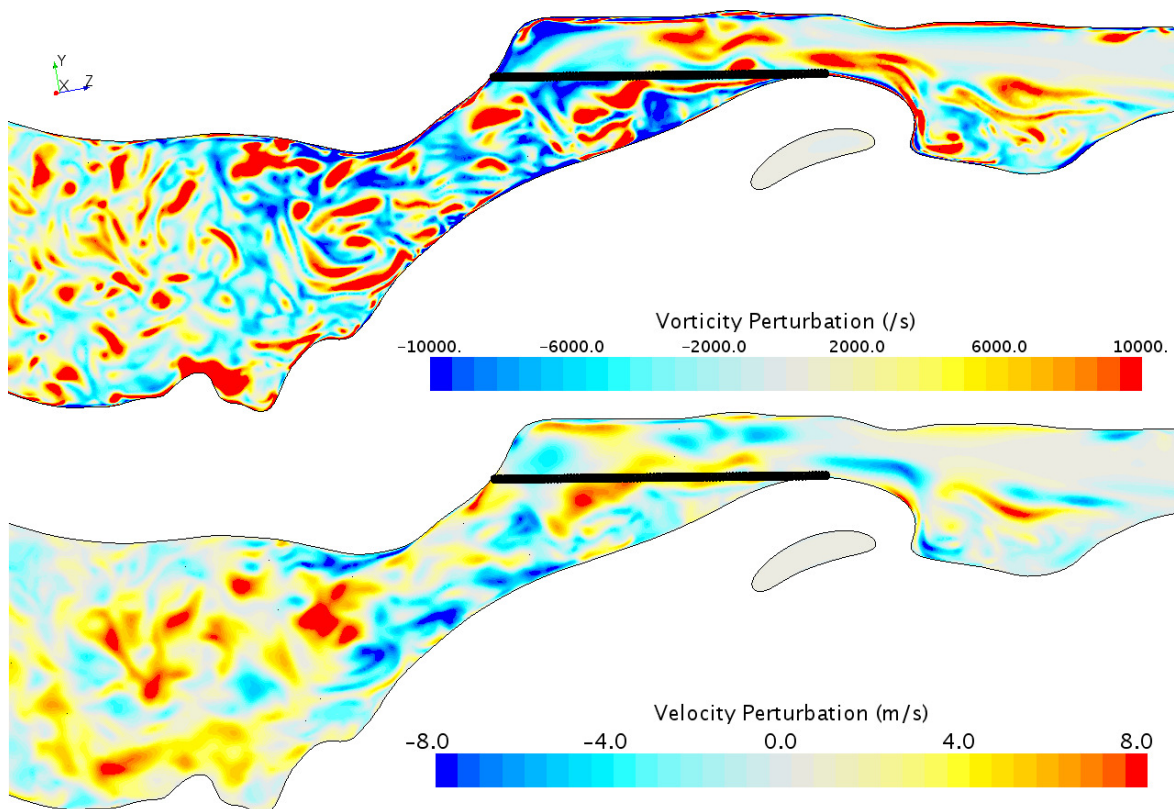


Figure 4.22: Instantaneous vorticity and velocity perturbations in the pharynx and larynx at 0.13 s. The black line is shown to indicate the positions over which figures 4.23, 4.26 and 4.27 were calculated. The axis symbol (top left) shows the principal directions used in figure 4.23.

$\text{ms}^{-1}$  can be calculated, which is somewhat slower than the mean velocity magnitude calculated over this period of  $24 \text{ ms}^{-1}$  (figures 4.19 and 4.24). This discrepancy is due to the shape, size and swirling nature of the features.

The perturbations are strongest in the  $u_3$  direction, which is most closely aligned with the flow, followed by the  $u_1$  direction (medial to lateral) with the weakest fluctuations apparent in the anterior to posterior direction. A clear pattern of peaks can be seen with a separation of approximately 0.9 ms, however the strength of these peaks varies greatly, with high values often occurring in pairs, suggesting a lower frequency oscillation at about ten times the period. The fluctuations at the superior end of the line are more regular and are indicative of flapping in the shear layer at the epiglottis (see the left arrow in figure 4.20).

The superior end of the line is within the boundary layer at the anterior side of the

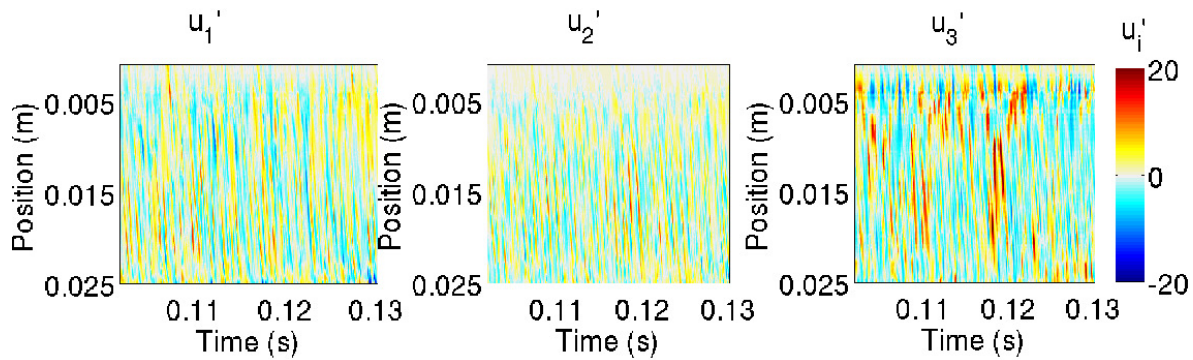


Figure 4.23: Fluctuating velocity components taken over a 30 ms window from 0.1 s to 0.13 s over the line shown in figure 4.22. Distance along the line is measured from the superior end.

hypopharynx, so the velocity is lower here. The velocity then rises as the line enters the bulk-flow region. The change in mean velocity at the inferior end of the line is due to the flow turning above the glottis.

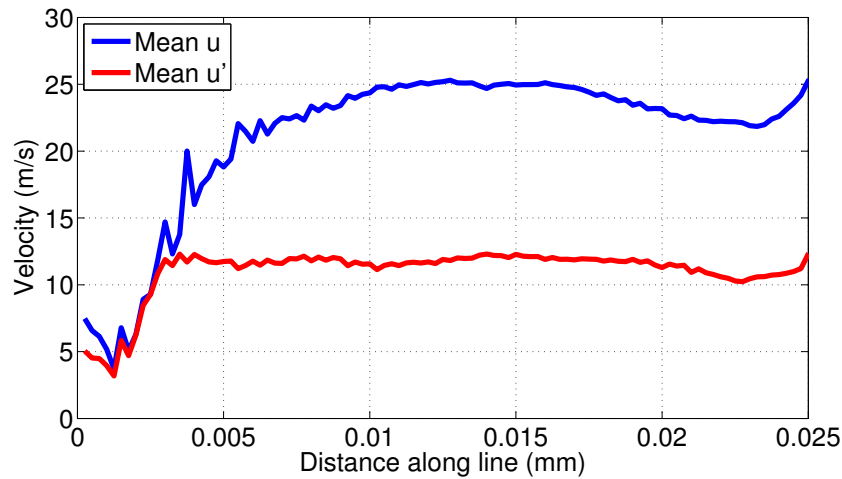


Figure 4.24: Mean of the magnitude of velocity and the mean of the fluctuating magnitude of velocity along the line shown in figure 4.22.

The break down of separated shear layers as the primary cause of fluctuations in airway flow. The fluctuation energy is far larger in the supraglottic and glottic zones than in the nose, but is of a different character. This is shown by plotting the energy spectra of the velocity fluctuations in the nose and supraglottic region in figure 4.25, at the points indicated by crosses in figure 4.20. Given the limited duration of the temporal window, the spectra are processed in the manner described by Varghese et al. [116],

but using just two Hann windows. Figure 4.25 shows the (unnormalised) fluctuation energy in the supraglottic region to be more than two orders of magnitude greater than in the nose; moreover the velocity spectrum at the point in the nose lacks the broad band energy content of that in the downstream regions. Normalising the spectrum indicates the emergence of a limited inertial subrange, consistent with  $Re_\lambda$  of around 20, as computed at that point [94].  $Re_\lambda$  is defined by the equation

$$Re_\lambda = \frac{u'\lambda}{\nu} \quad (4.2)$$

where  $\nu$  is the kinematic viscosity,  $u'$  the fluctuating velocity and  $\lambda$  the Taylor microscale,

$$\lambda = u' \left( \frac{15\nu}{\varepsilon} \right)^{\frac{1}{2}} \quad (4.3)$$

assuming isotropic turbulence [90].

To determine how sensitive the spectra shown in figure 4.25 are to their location, a series of one hundred spectra are calculated and plotted as a surface in figure 4.26. There is less fluctuation energy at the superior end of the line, with a band of high energy representing the flapping frequency of the shear layer. Most of the surface forms a plateau, before a further reduction in energy occurs at the far side of the surface, which correlates with the region where the flow is relatively constant, as seen in figure 4.22. The distribution of energy between frequencies is similar across the surface.

In order to determine the fundamental frequencies of the flow, the low frequency region of the spectral surface is plotted linearly in figure 4.27. The two periods detected in figure 4.23 are both apparent here. A period of 0.9 ms approximately correlating with the peak close to 1 kHz occurs near the inferior end of the line. The higher period detected has a frequency close to 100 Hz and this can also be seen around the mid portion of the line. Both peaks have a series of harmonics extending throughout the frequency band shown here. In the boundary layer (top of figure) little low frequency energy is visible, but the flapping frequency of the shear layer is detected at 212 Hz (equivalent period of  $\sim 5$  ms), with a further peak at 990 Hz, perhaps related to the lower frequency discussed above.

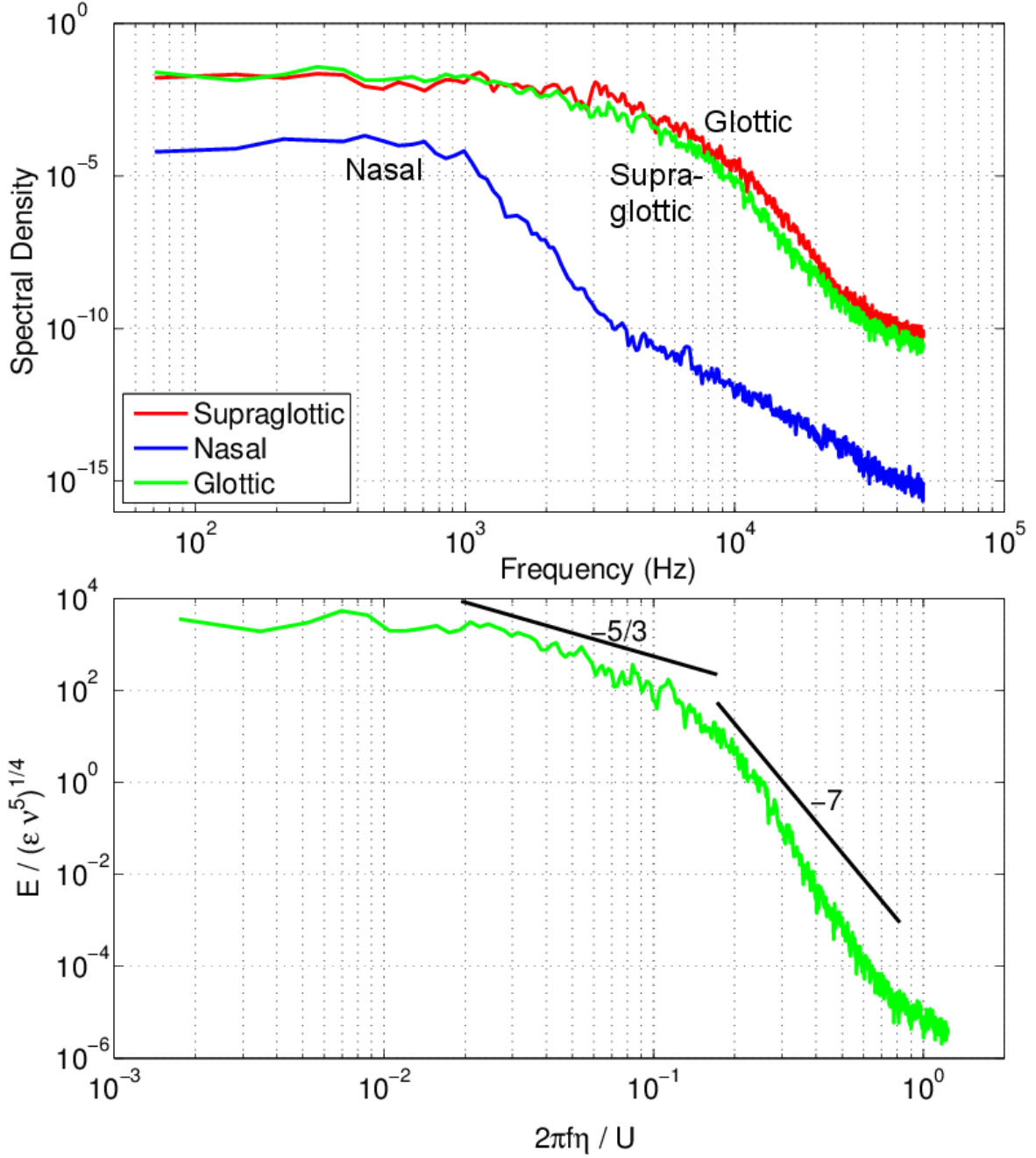


Figure 4.25: Upper: Summed power spectra of fluctuating components of velocity at points in the nose (lower curve), supraglottic region (upper curve) and glottic region (middle curve). Lower: spectra from the point in the glottis, scaled by the viscous dissipation rate,  $\epsilon$  and the kinematic viscosity,  $\nu$ . The frequency,  $f$  is scaled by the  $\frac{2\pi\eta}{U}$ , where  $U$  is the mean velocity at that point and  $\eta$  the Kolmogorov length scale.

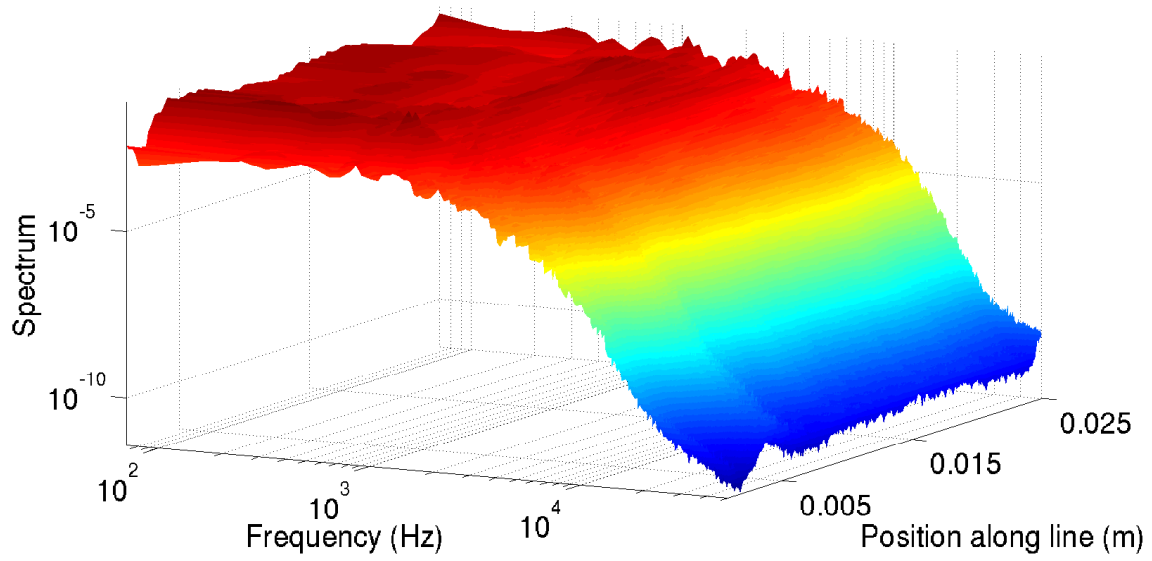


Figure 4.26: Surface of spectra calculated at 100 points along the line shown in figure 4.22.

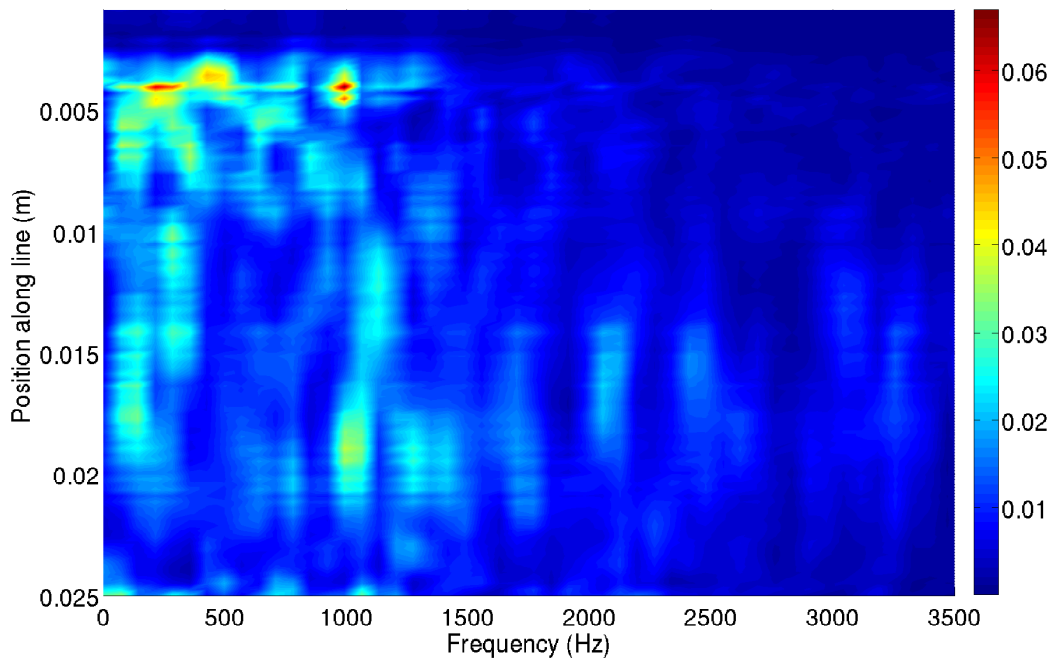


Figure 4.27: Low frequency region of spectra calculated at 100 points along the line shown in figure 4.22.

## 4.8 Reduced Resolution Simulation

The simulation described in this chapter was repeated on a coarse mesh with approximately one fifth as many elements and at a time step ten times larger. The partitioning of mass flow between the various sectors lacked only the minor high frequency oscillations visible in figure 4.13, but was otherwise virtually identical. Likewise, the computed pressure loss between each plane in figure 4.2 differed between the simulations by less than 4% (ignoring the high frequency fluctuations) for nearly all planes. The exception was the transglottal loss (planes 8–10), where the coarse simulation recorded a 9% lower pressure drop. Since the latter region contains the main laryngeal jet and thus the most chaotic flow, it was expected that incomplete resolution would be most evident in this zone.

Simulations at lower resolution thus appear capable of capturing the overall dynamics of the flow, with adequate accuracy given the multiple physiological uncertainties. However for measures such as heat and water exchange and particle dispersion that are more sensitive to flow gradients, it is less likely that the coarse resolution would be adequate, without some form of additional modelling.

## 4.9 Summary

Numerical simulation was applied to chart the dynamics of the airflow and the transport of an inhaled gas during a rapid inhalation such as a sniff. The inhalation profile had overall parameters: 0.5 s duration,  $1 \text{ l s}^{-1}$  peak flow, inhaled volume 364 ml and was derived from previous *in vivo* measurements by an analytic fit. A realistic airway geometry was used extending from the nose to the large bronchi, whilst computations employed high spatial and temporal resolutions (cell volume of order  $0.001 \text{ mm}^3$  in refined regions, time step  $10^{-5} \text{ s}$ ).

Local flow patterns strongly affect convective transport throughout the airways. The patterns of flow changed both spatially in response to the airway cross-sectional area and shape, and temporally as the flow rate built up and decayed. Significant differences in flow structure and flow distribution were found between the left and right nasal cavities. Where the airway enlarged rapidly in the nose and in the supraglottic region, separated shear layers were produced, becoming unstable when the local velocity became sufficiently high. In the supraglottic region, fluctuations of a relatively high

amplitude developed early in the acceleration phase and persisted to the end of the inhalation. In contrast, fluctuations in the nose developed later and died out as the flow diminished below 70% of its peak.

The dynamics of the flow development followed significantly different time scales in the various zones; consequently it is inappropriate to assume that flow behaviour simply scales with the inhalation profile. Key features of the observed evolution of inspiratory flow can be summarized as follows:

- In the nose, different patterns of flow appeared in three phases, labelled initiation, quasi-equilibrium and decay. The intra-cavity partitioning of nasal flow altered part way through the initiation or flow build up phase. This corresponded to the establishment of localised flow separations and was of similar duration to the time required for the initial flow and the scalar to fill the nasal cavity (50 ms). Thus flow initiation was essentially completed for the nose significantly before peak inhalation flow.
- During the approximately flat plateau phase of the bulk of the inhalation, the partitioning of flow between various parts of each cavity, and between cavities, was virtually constant, save for minor disturbances due to flow field fluctuations.
- Spontaneous fluctuations in local flow velocity were observed at an early stage ( $\sim 20$  ms) in the region of the glottis, whereas fluctuations in the nasal cavity were delayed nearly to peak flow ( $\sim 100$  ms) and were of a lower amplitude. High turbulence intensities (fluctuating velocities of around  $10 \text{ ms}^{-1}$ ) occurred at the margins of the jet in the supraglottic region, whilst in the nose, fluctuations were lower (less than  $1 \text{ ms}^{-1}$ ) and occurred predominantly in the right cavity. The pattern of flow transition, both spatial and temporal, differed not just along the airway but between both sides of the nose.
- Finally, in the decay phase, the partitioning of flow between the parts of the nasal cavities remained unaltered until approximately the final 100 ms and in some parts even later.

## 5 Transport in a Rapid Inhalation

The primary purpose of inspiration is to deliver fresh air to the lungs. Before fresh air reaches the lungs however, the “dead space” of air remaining in the airways must be cleared, and it is of interest to note how rapidly this occurs. For a sniff however, the primary interest is in the fate of inhaled species: where do they reach in the nose, how quickly does concentration build and wash out, where are the fluxes of transport greatest etc. Introducing a scalar species to be tracked during the inhalation process addresses many of the pertinent questions. In its simplest role, the scalar species acts as a flow marker. If advective transport of the scalar dominates over diffusive transport, the scalar will move with the flow; provided it is not depleted at the wall through absorption, this flow marker will be representative of the transport behaviour of the airstream. Transport times can be determined for air originating outside the airways to reach various locations throughout the airways. In the limiting case for transport this governs how quickly a scent could reach the olfactory receptors, where it may be detected. However, *in vivo* the scent molecules must adhere to the mucus film and be transported across this before activation of the chemosensory receptors. Regional analysis of scalar progression also highlights the clearance rates of various regions, determining areas with long residence times and those where the bulk through-flow dominates. The external origins of the inhaled air reaching particular locations can also be determined, as outlined in Doorly et al. [26].

Scalar transport is modelled in the rapid inhalation described in section 4. This allows the effect of the flow patterns discussed in that chapter, such as the separation in the anterior portion of the right nasal cavity on scalar transport to be characterised. Different scalar species are considered. As a marker for the purely convective transport by the flow, a species with very low diffusivity and with no absorption at the wall is introduced. The fate of inhaled species depends on several parameters, but principally their size and mass. Larger particles do not follow path lines of the flow due to factors such as size, shape, inertia and gravitational effects. These effects diminish with particle size, though additional displacements due to Brownian motion become significant at very small scales. Pure convective transport by the flow is more approximately realised for nanoparticles which are small enough to neglect inertial effects. Whilst analysis of the low diffusing, non-absorbing scalar is revealing for the reasons described above, it is not representative of particles or gaseous species which are likely to be absorbed *in*

*vivo*. Therefore, having established the transport behaviour of the limiting case, three additional scalars are analysed, representing a range of the two factors absorption and diffusivity. Comparison of the different transport behaviour of each scalar allows the effect of the parameters to be quantified.

## 5.1 Transport by the Flow of a Low Diffusion Inhaled Scalar

As outlined, to investigate the effect of the dynamics of airflow on convective transport during rapid inhalation, a scalar species with low diffusivity ( $Sc = 900$ ) was introduced and tracked. At all boundaries other than the outlet, the scalar concentration gradient was held at zero, as in equation 2.16, to prevent absorption by the surface, whilst the outlets afforded no barrier to escape. The focus of the following section is to describe how tracking this idealised scalar reveals how the flow field directs inhaled species to enter and to fill the various regions of the airway in the absence of species dependent absorption and diffusion characteristics.

Before the inhalation, the scalar was confined to an approximately hemispherical volume of 364 ml (the total volume inhaled) positioned against the face, with the widest point (diameter) level with the nostrils, figure 5.1.

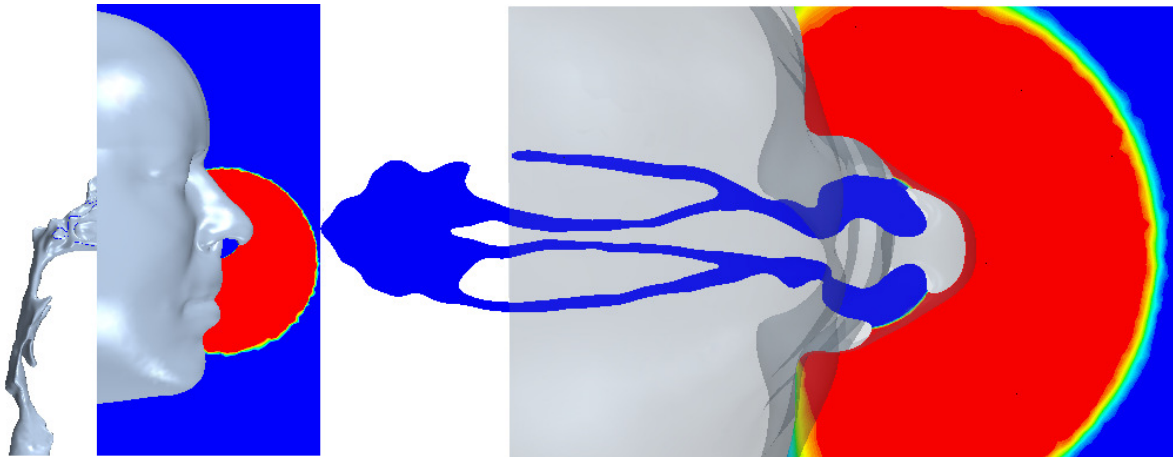


Figure 5.1: Initial scalar distribution.

The concentration of scalar at the nostrils (plane 1, figure 4.2) is shown in figure 5.2. The scalar reaches the nostril after 0.005 s and quickly reaches almost 100% concentration. This plateau lasts for approximately 0.2 s, at which time the concentration decreases.

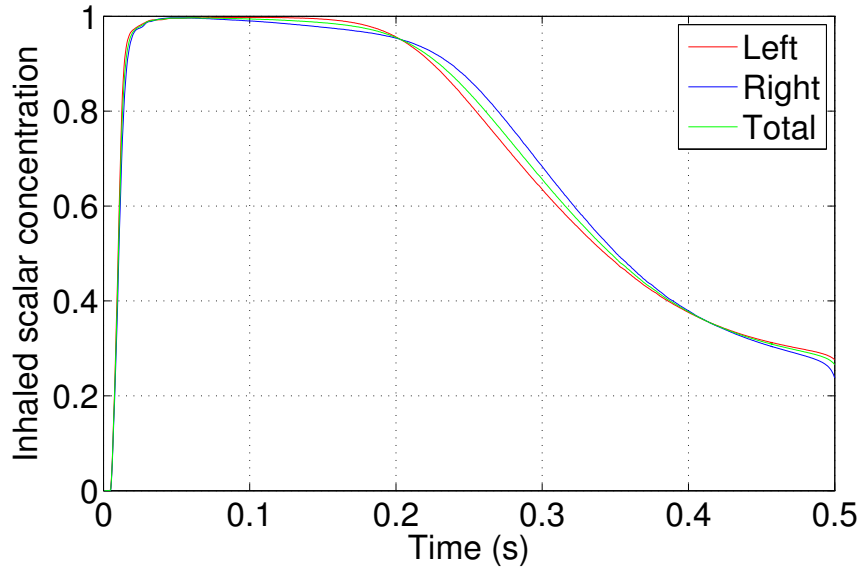


Figure 5.2: Concentration of scalar inhaled through the nostrils (plane 1 figure 4.2).

Figure 5.3 shows the initial progress of the scalar into each nasal cavity, where overlaid colours are used to mark the 50% concentration threshold at various instants up to 0.1 s.

The figure shows how the local recirculation regions that develop hinder the scalar advance. This recirculation zone is similar to that found experimentally by Schreck et al. [99], Kelly et al. [51] and Doorly et al. [26] and inhibits scalar ingress into the upper regions of the nose (where olfactory receptors are located most densely) throughout the early part of the sniff. As noted by Kelly in comparing their work with earlier studies of Schreck, the size and occurrence of recirculation zones are geometry dependent; here there is no comparable recirculation in the left cavity.

Between 0.01 s and 0.02 s, the scalar front has progressed beyond the vestibule and at 0.03 s has reached the head of the middle turbinate. Also at 0.03 s, the scalar has progressed further into the left cavity, where velocities are higher, than into the right.

On both sides, the scalar progression is greater above than below the inferior turbinate. By 0.04 s, almost the entire left cavity is flooded with scalar, whereas on the right, the white, unfilled region marks the recirculating air in the upper anterior cavity.

After 0.05 s, the scalar field has reached the back of the turbinates and is entering the nasopharynx region. Though not evident in the sagittal plane shown, the scalar takes a similar amount of time to reach the olfactory cleft located in the upper region of the

nasal cavities.

After 0.1 s both cavities appear well-filled, with the notable exception of the recirculation regions and dead-end passages, which are bypassed by the bulk flow. Overall, the pattern of scalar advance agrees well with in-plane velocities in the nose, due to the relatively narrow calibre of the passages.

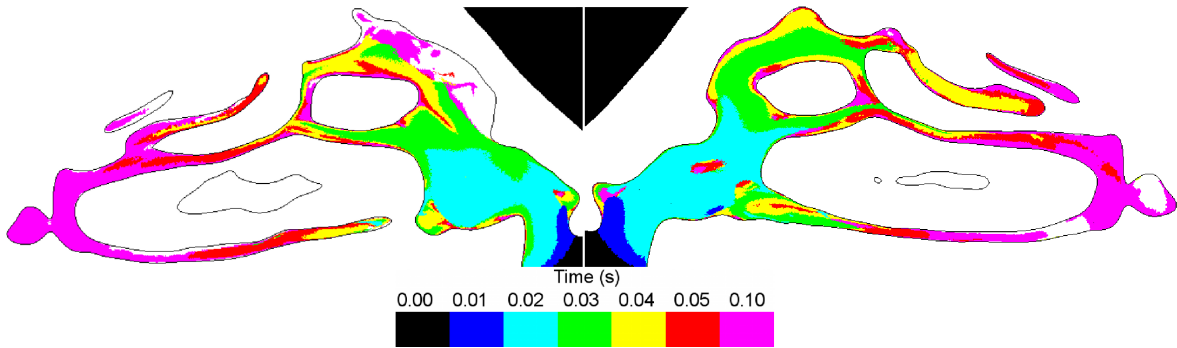


Figure 5.3: Planar contours of 50% scalar concentration at successive instants (coded by colour) in the nasal cavity.

Figure 5.4 shows the progress of the scalar in the external and internal domains over the entire course of the inhalation. Scalar concentration is shown on the lower axial plane described in figure 4.3. At 0.04 s, saturated scalar has filled the nostrils and spread either side of the inferior turbinate in each cavity. Mixing by the complex velocity field dilutes the scalar front, which is entering the nasopharynx, carried by a pair of post-septal jets. By a tenth of a second, the nasal cavity is almost saturated.

The effect of the physical separation of the nostrils can be seen in the external scalar distribution at 0.25 s. Whereas earlier the scalar appears to be drawn to a single sink, the external scalar front is now retreating towards the nostrils more rapidly at the sides. Hence at 0.25 s, scalar-free air begins to be drawn in from the sides and below the nostrils, before all the external scalar has been inhaled.

By 0.5 s, the scalar has almost disappeared externally, with 81% of the available scalar inhaled. Some scalar remains within each cavity, with less in the right nostril as this has been washed out by clean air due to high velocity in the lower medial region (figure 4.13).

The extent of dispersion of the advancing scalar front, resulting from the combination of narrow passageways, flow division and recombination throughout the nose is revealed

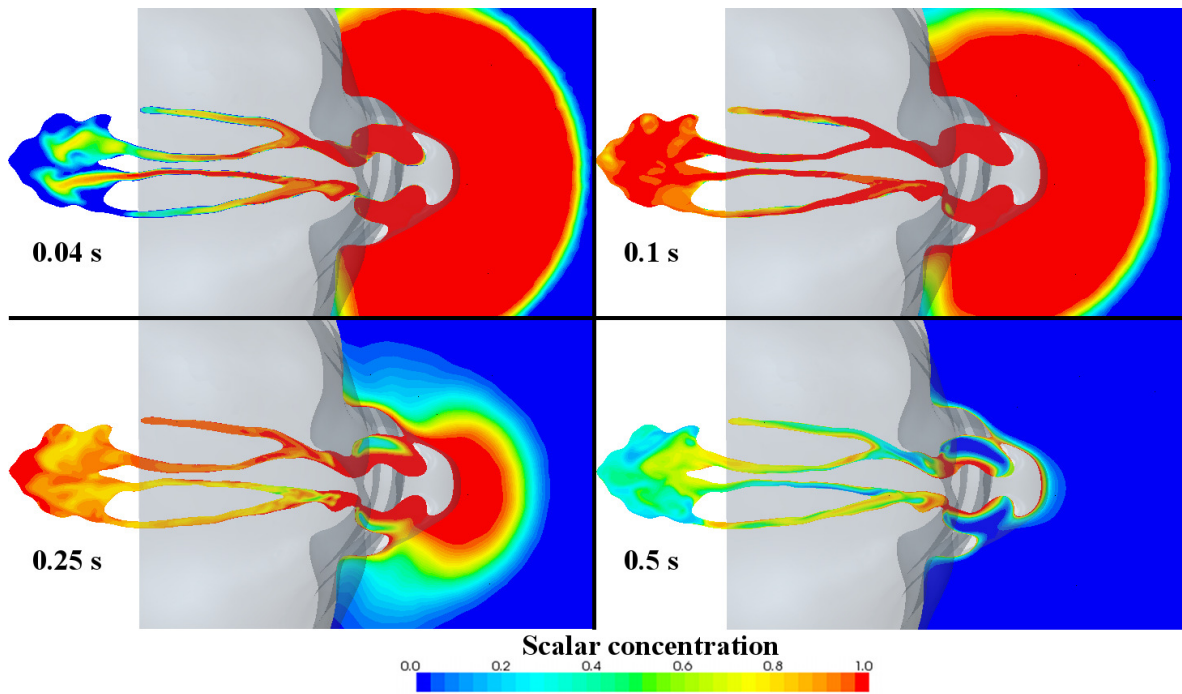


Figure 5.4: Distribution of scalar species on lower axial plane (figure 4.3).

in figure 5.5, where the scalar concentrations on the higher axial plane (figure 4.3) and on planes 1-7 from figure 4.2 are shown at 0.04 s.

The imprint of the anterior recirculation in the upper right cavity on the scalar field is again evident in both views, corresponding to a zone of low scalar concentration. Similarly, recirculation regions affect the anterior region of each nasal vestibule in plane 1.

At plane 4 the bulk of the flow bypasses the upper parts of the inferior meatus, which remains devoid of scalar at this time. At plane 5, differences between the flow in each cavity are also apparent in the more homogeneous distribution of scalar on the left side; the relative concentration distributions accord with the partitioning of airflow shown in figure 4.13.

Planes 6 and 7 show that the greater flow in the left cavity results in a larger but less intense post-septal jet, whilst the effect of the mixing of jets in the nasopharynx on scalar distribution can be seen in plane 7.

An overview of this scalar inhalation is given in figure 5.6. This figure shows volume renderings of scalar concentration at five instants through the sniff, highlighting the

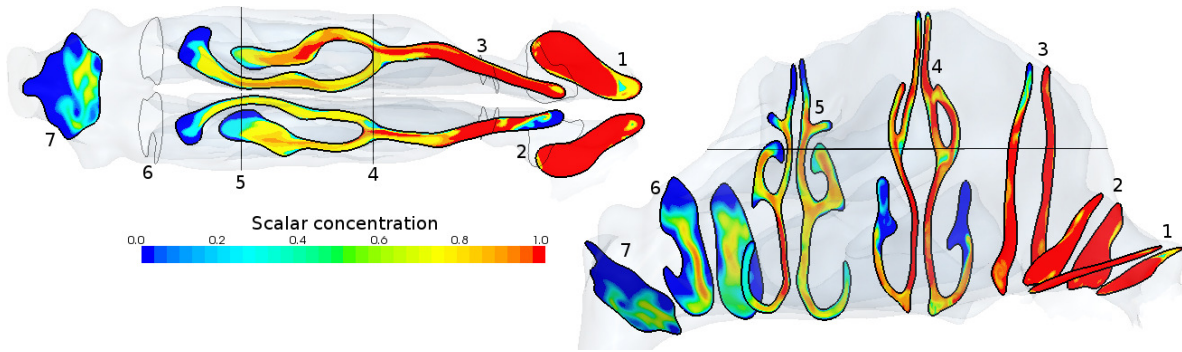


Figure 5.5: Instantaneous scalar distribution in the nose at 0.04 s on planes 1-7 (figure 4.2) and the upper axial plane (figure 4.3).

three dimensional nature of its progression. At 0.02 s, flow is drawn upwards into the nasal vestibule, separation occurs at the right nasal valve as mentioned previously and the scalar in the left nostril has been drawn towards the superior aspect of the nasal cavity more than in the right. By 0.05 s, the anterior region of the right nasal cavity remains clear of scalar due to the recirculation zone. Flow is moving faster on the left side and has penetrated further into the cavity. Most of the scalar travels along the septal wall, although some is visible in the left cavity's middle meatus.

At 0.10 s, scalar has flooded the bulk of the nose, but certain regions remain clear or with low concentration. These regions include the upper medial region of the cavity where the surface contains many olfactory receptors and the inferior meatus.

In the latter half of the sniff, the olfactory region is highly saturated with scalar in both nostrils, increasing the likeliness of scent detection. By the end of the sniff, the right posterior aspect of the olfactory region is still saturated with scalar, showing very high residence times here.

The boundary of the scalar remaining outside the face progressively deforms through each image, showing the directional bias of inhaled air. It is taken up most rapidly from a horizontal plane in line with the nostrils, causing clean air to be taken in from the sides of the face, this allow the nose to clear of scalar rather than to continue to saturate.

The arrival of scalar and its decay as fresh air is inhaled was computed for each of the planes shown in figure 4.2 with the results from four planes shown in figure 5.7.

The shape of these curves approximately follows that of the volumetric flow profile shown in figure 4.5a, although it must noted that the concentration of inhaled scalar

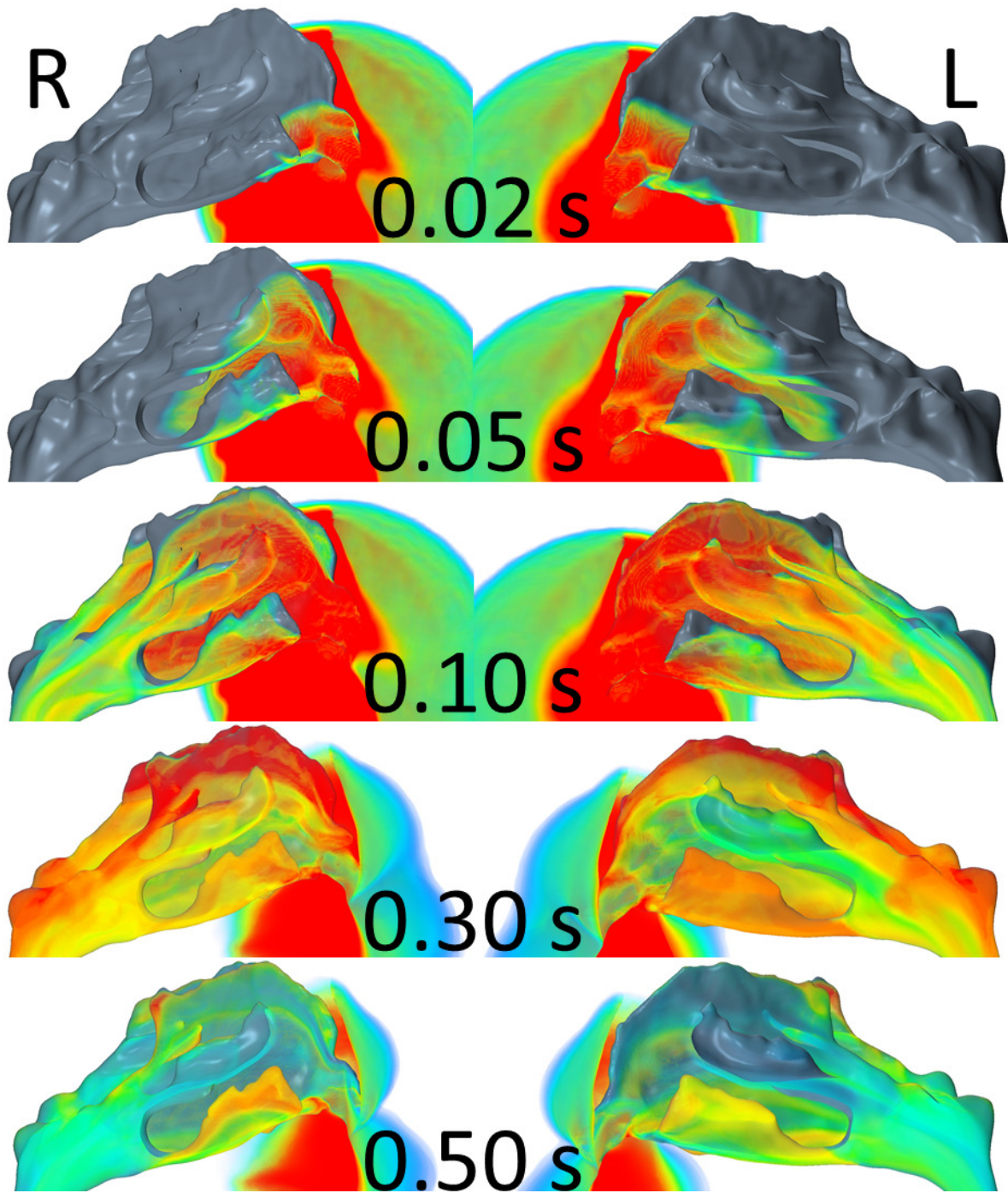


Figure 5.6: Volume renderings of scalar concentration at five instants. Red, opaque regions indicate regions of high concentration, whilst semi-transparent blue represents low concentration. The nasal geometry is rendered in grey and in regions where this is visible there is no scalar.

begins to become diluted from about 0.1 s, figure 5.7. Thus the scalar flux through plane 1 shows a slight downwards slope to the plateau, contrary to the slight increase in volumetric flow beyond 0.1 s; since the initial dilution is small, the effect is very slight. By plane 4, this effect is offset somewhat by recirculation regions filling through mixing with the main flow.

The time taken for the scalar to first appear at successive downstream planes increases from virtually zero at the nostril plane, to 0.03 s at the head of the middle turbinate (plane 4) and 0.07 s at the carina (plane 12). This latter time is actually shorter than the time taken to inhale a quantity of air equivalent to the volume of the airway to the carina, 0.093 s. The difference between these times indicates that newly inhaled air does not effectively fill the entire volume, whilst the non constant velocity profile causes some scalar dispersion.

Integrating curves of scalar flux shows that 292 ml of scalar was inhaled out of a total inhaled volume of 364 ml. Of the inhaled scalar, 265 ml passed plane 12, the carina entering the bronchial tree, whilst 27 ml remained in the airways. 10 ml of scalar was left in the nasal region (between planes 1 and 7), representing a concentration of 40% in the nasal volume.

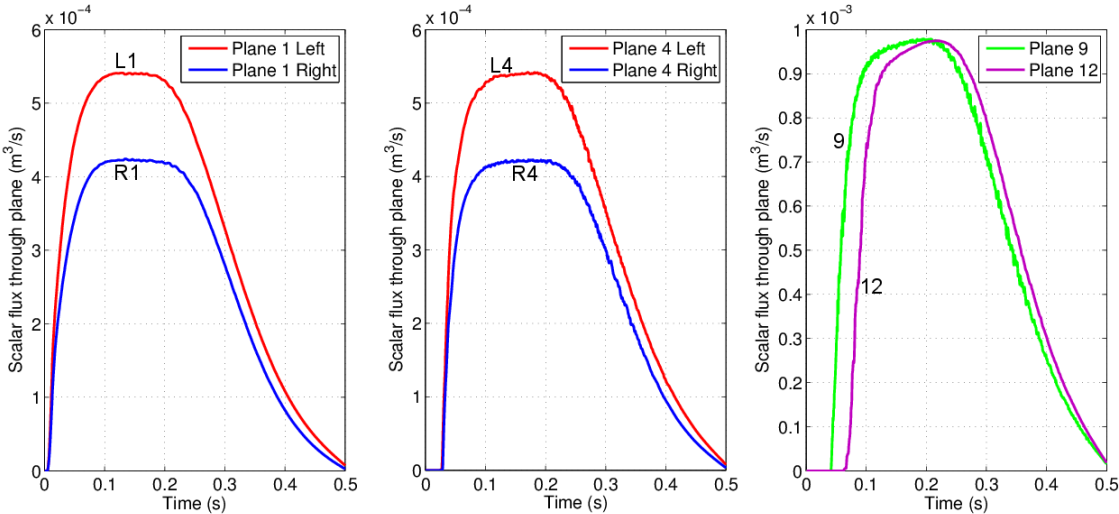


Figure 5.7: Scalar flux  $\int (\mathbf{u}\phi + D\nabla\phi) \cdot \hat{\mathbf{n}} da$  through the nostril (figure 4.2, plane 1, left), mid nasal cavity (figure 4.2, plane 4, centre), supra-glottic region (figure 4.2, plane 9, right) and the distal trachea (figure 4.2, plane 12, right). The first two plots show the two sides of the nasal cavity separately.

Figure 5.9 shows the saturation of the scalar species in the upper region of the nasal cavities, defined as shown in figure 5.8. This region includes the olfactory cleft, so scalar intrusion into this region makes sensory detection more likely. Both nostrils fill their upper regions to above 95%, showing that despite the recirculation zones and low flow rate areas, the mixing of the flow is sufficient to flood both nostrils eventually. The left cavity fills more quickly than the right, due to the higher flow rates on this side whereas on the right the recirculation zone fills slowly through mixing with the main flow. These effects mean that scalar clears the right cavity more slowly.

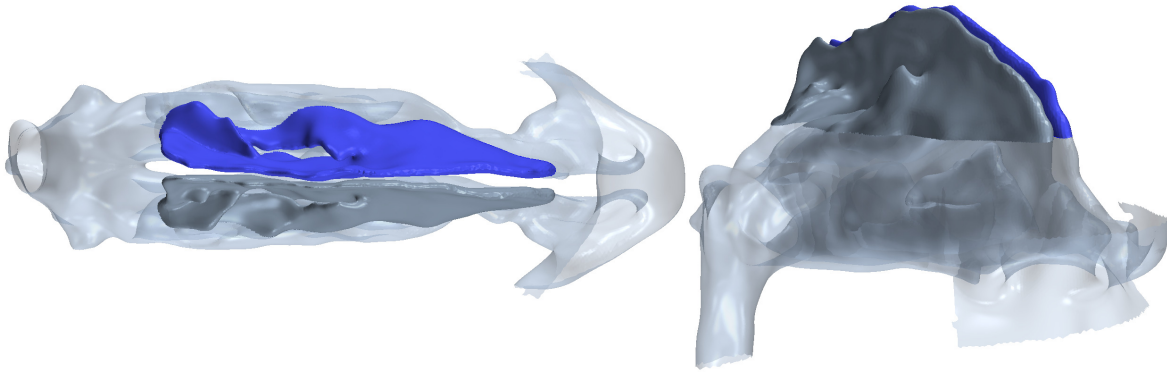


Figure 5.8: The upper regions of the airway in sagittal (left) and projection (right) views. These volumes represent those considered in figures 5.9 and 5.14.

## 5.2 The Effect of Diffusivity and Absorption on Scalar Transport

The scalar species considered in section 5.1 had low diffusion and was not absorbed at the airway wall. These parameters allowed analysis of convective flow patterns. Real inhaled nanoparticles are likely to exhibit more diffusion and to be absorbed at the airway wall into the mucus and serous lining. Three additional scalar species were considered, representing the bounds of parameters likely in inhaled species. The properties of these species are tabulated in table 5.1, where scalar A is the species considered in section 5.1. The Schmidt and Péclet numbers are defined in equations 2.29 and 2.30 respectively. The high values of Péclet number show that advective transport dominates over diffusion for scalars A and C and is still many times higher in B and D. Most odourants have Schmidt numbers in the range 0.6-2.5 [53] and therefore diffusive properties similar to the latter pair.

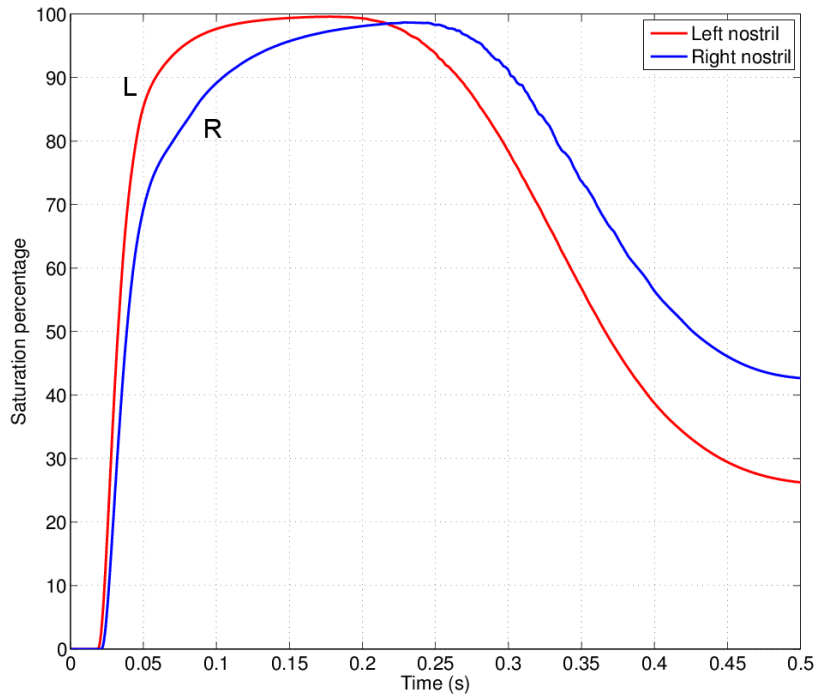


Figure 5.9: Scalar build up and decay in nasal region above the upper axial plane (figure 4.3), and shown in figure 5.8, calculated as  $\int \phi dV$  and expressed as a percentage of the total volume of the upper region in each nasal cavity.

The boundary conditions of scalars A and B are the same on all surfaces of the geometry and are non absorbing, as shown in table 5.1. Scalars C and D have different boundary conditions in different regions to represent the conditions *in vivo*. Posterior to the nasal valve, an absorbing boundary condition is applied to the airway lining to represent the mucosa that would naturally line this region. Anterior to the nasal valve, in the nasal vestibule and on the face, the non-absorbing boundary condition used in scalars A and B is applied to represent the exterior epidermis found in these regions.

The flux of these species across planes in the nose and descending airways is shown in figure 5.10. The differences between each pair of similarly coloured pairs shows the absorption in the relevant area; red the left nasal cavity, blue the right and green the descending airways. Scalars A and B behave similarly, with no absorption apparent (as expected) but with an offset showing the transit time for each region. Scalar C, which may be absorbed by the wall, also exhibits almost identical behaviour, with a slight difference in the shape of the peak flux at the carina, showing some scalar has

	A	B	C	D
$Sc$	900	0.9	900	0.9
$D$ ( $m^2s^{-1}$ )	$1.74 \times 10^{-8}$	$1.74 \times 10^{-5}$	$1.74 \times 10^{-8}$	$1.74 \times 10^{-5}$
$Pe_{Nose}$ (L - R)	$2.16 \times 10^6 - 1.71 \times 10^6$	2160 - 1710	$2.16 \times 10^6 - 1.71 \times 10^6$	2160 - 1710
$Pe_{Glottis}$	$1.26 \times 10^7$	12,600	$1.26 \times 10^7$	12,600
Boundary condition	$D\nabla\phi_A \cdot \hat{\mathbf{n}}_w = 0$	$D\nabla\phi_B \cdot \hat{\mathbf{n}}_w = 0$	$\phi_{C,w} = 0$ *	$\phi_{D,w} = 0$ *
Description	Low diffusion, non absorbing	High diffusion, non absorbing	Low diffusion, with absorption	High diffusion, with absorption

Table 5.1: Properties of considered scalar species.  $Sc$  is the Schmidt number,  $D$  the diffusivity and  $Pe$  the Péclet number (calculated at the nose (plane 3, figure 4.2) and above the glottis (plane 9) at peak flow). These boundary conditions are explained in the discussion of equations 2.17 and 2.16. \*The absorption boundary condition only applies to the airway lining posterior to the nasal valve, elsewhere (the nasal vestibule and exterior face) the non-absorbing boundary condition is used.

been absorbed by this location. Scalar D, which is allowed to absorb but which is also highly diffusive is markedly different from the previous three. The fluxes at the nostril are the same as in the other cases, as no absorption takes place outside the nose, but by plane 6, at the back of the nose, has reduced by more than 60%. This value compares well with the work of Inthavong et al. [43], who found 72% of 1 nm particles were deposited within the nose and a decrease in this value with particle size. This absorption in the nose means less scalar enters the nasopharynx at plane 7 than in the other cases and this has further decreased by the carina. Therefore, it is necessary that an inhaled substance is diffusive for significant absorption to take place, regardless of the boundary condition.

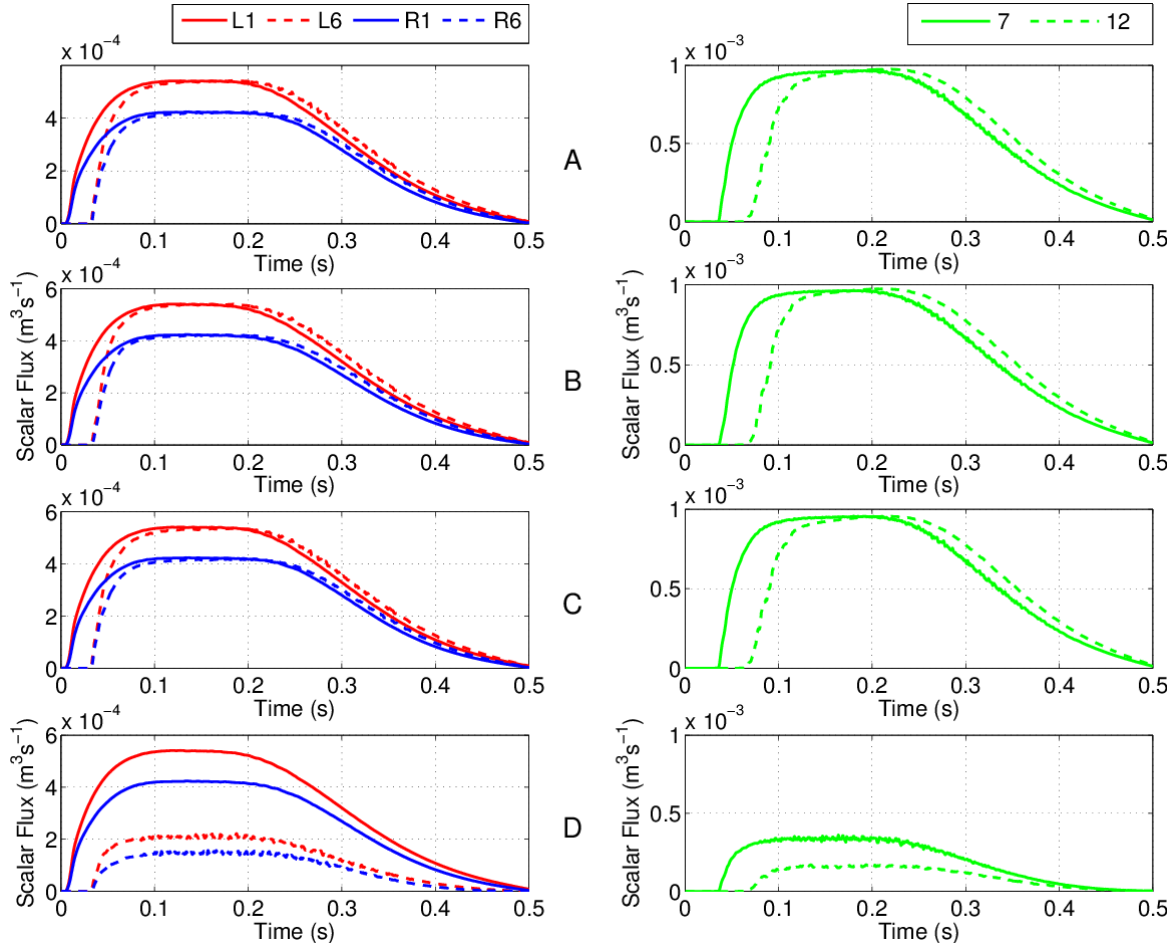


Figure 5.10: Comparison of scalar flux through planes 1 and 6 in either side of the nasal cavities (upper) and 7 and 12 in the descending airways (lower) for scalars A-D (left to right). The planes are defined in figure 4.2. (A - low diffusion, non-absorbing, B - high diffusion, non-absorbing, C - low diffusion, absorbing, D - high diffusion, absorbing.)

The flux for each scalar through the nostril (plane 1, figure 4.2) and the carina (plane 12) are compared in figure 5.11. At the nostril the two pairs of scalar with the same diffusion rates overlay each other exactly. There is a difference in the two pairs' flux through the nostril which increases through the duration of the sniff. This is due to the scalar outside the face, which has a large surface area and diffuses away from the nostrils before it is inhaled. Furthermore, the low velocities in this region means that the diffusion effects are comparatively larger here than they are within the airways. The exterior Péclet number in this region is 14,000 for scalars A and C and just 14 for scalars B and D, using the nostril hydraulic diameter as the length scale. This difference at the nostril accounts for the vast majority of the difference downstream at the carina and suggests that diffusion within the airways and the absorption of a low-diffusing scalar is small in comparison.

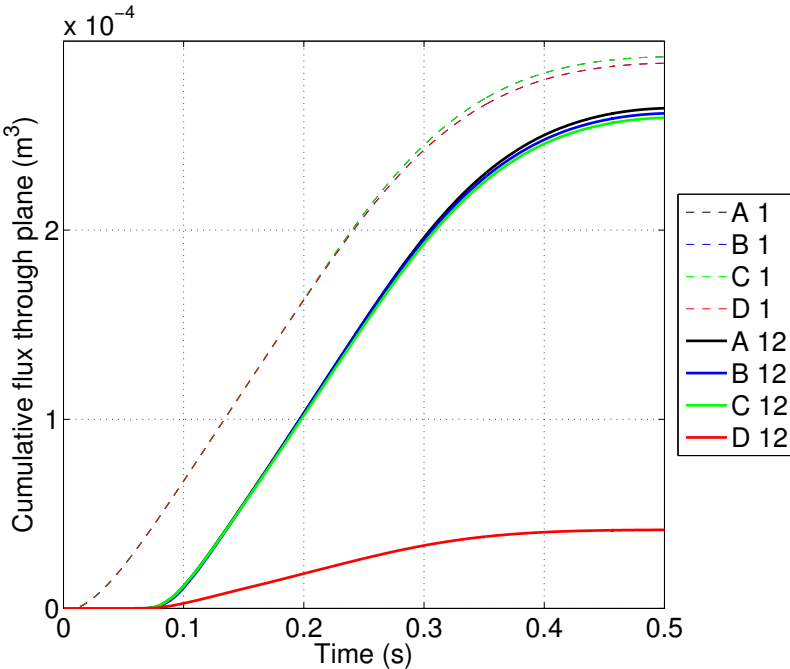


Figure 5.11: Comparison of fluxes of scalars A-D through the nostril (both sides summed, dashed line, plane 1, figure 4.2) and the carina (solid line, plane 12). At the nostril, the curves for scalars A & C and B & D overlay each other exactly. (A - low diffusion, non-absorbing, B - high diffusion, non-absorbing, C - low diffusion, absorbing, D - high diffusion, absorbing.)

To distinguish which regions are responsible for this absorption, figure 5.12 shows the flux of scalars C and D through each plane in figure 4.2. As scalar C is not significantly

absorbed, the difference in the total flux between each pair of planes represents the volume of scalar remaining in that region at the end of the sniff. These amounts are likely to be reduced in the depleted scalar D, but the difference between the fluxes in C and D represents the minimum amount absorbed at the wall by each subsequent plane. The difference between subsequent lines is the amount absorbed between the planes they represent. The largest volume is absorbed between planes 4 and 5, the region containing the bulk of both the middle and inferior turbinates. The region anterior to this, between planes 3 and 4, also exhibits large scalar absorption, as does the pre-turbinate region between planes 2 and 3. As scalar is inhaled at each location, there is less available to be absorbed in each subsequent region, therefore the percentage of scalar absorbed in each region compared to what entered is tabulated in figure 5.13.

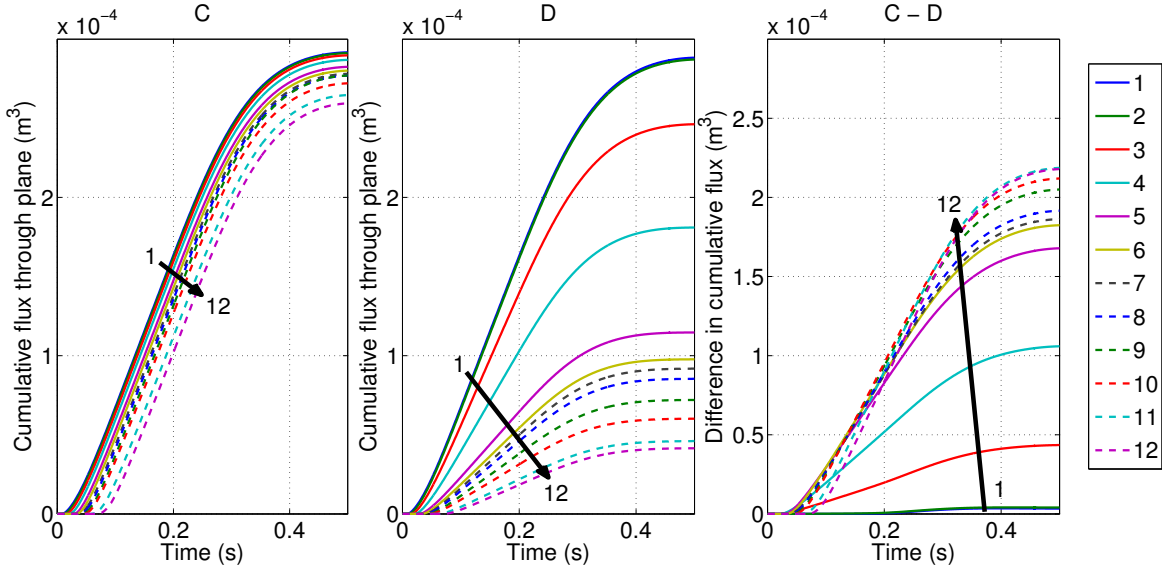


Figure 5.12: Cumulative scalar flux through each plane in figure 4.2 for scalars C and D (left and centre). Planes in the nasal cavity show the total of left and right sides and are represented with solid lines, whilst planes in the descending airways are shown with dashed lines. The third image shows the difference between through time. (C - low diffusion, absorbing, D - high diffusion, absorbing.)

It is not expected that these flux differences will be equal across regions, as the intra-plane regions are not equal either in airway volume or wall surface area, but it does allow the anatomic regions responsible for absorption to be identified. Furthermore, as this figure shows the total difference in flux between each successive plane, it does not differentiate between flux that is “lost” due to absorption at the wall and that which is left in the airway and the end of the sniff. However, these remaining amounts should

be small as seen in the left-most graph in figure 5.12.

The region between planes 4 and 5 (figure 4.2) absorbs proportionally more scalar than any other region. This accounts for the region where both the middle and inferior turbinates intrude into the nasal cavities - resulting in a very high surface area to volume ratio, although the volumes are also quite large. The region anterior to this absorbs less proportionally, as only the inferior turbinate protrudes through most of this region.

Comparison of the two cavities reveals that more is absorbed proportionally throughout the right cavity, despite it having a similar surface area to the left, suggesting that lower velocities in the large recirculation regions allow more flux to the boundaries. The region between planes 10 and 11 extends from the glottis to the middle of the trachea. Here almost 25% of the scalar entering this region is absorbed, despite the concentrations being low (figure 5.12). This region is downstream of the most highly disturbed in the geometry (figures 4.19 and 4.20) and significant mixing is therefore apparent. The strong non-axial flows upstream redistribute the scalar, replenishing that which has been absorbed at the walls.

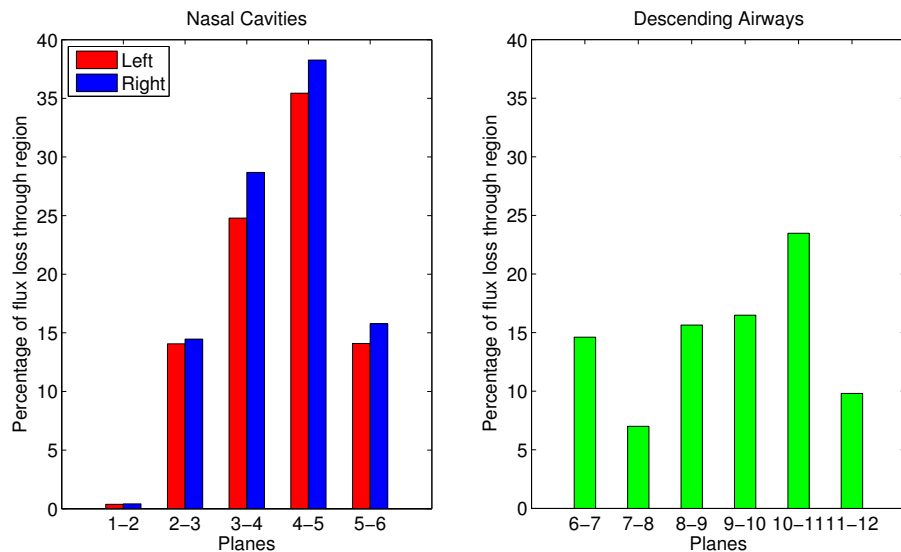


Figure 5.13: Proportion of scalar  $D$  entering each region (through first plane) that does not leave (through second plane). Planes 6-7 is calculated from the sum of the left and right planes 6. All planes are defined in figure 4.2.

Figure 5.14 shows the different filling and clearing characteristics of all four scalars in the upper region of the nose (figure 5.8). Scalars A (black curve) and B (blue curve) differ only in their diffusivity; neither are absorbed. The effect of this diffusivity can be seen in the quicker saturation of this region by the scalar B, the higher diffusivity allowing it to quickly fill regions not swept by the bulk flow. It is also cleared more quickly than scalar A. Scalar C (green curve) has the same low diffusivity as scalar A, but is absorbed at the walls. Therefore, it cannot saturate the region, reaching a plateau at 97% in the left cavity and slightly lower in the right. Scalar D, which is highly diffusive and is absorbed at the walls never saturates the region. Two factors account for this; firstly, it is absorbed at the walls and secondly, less enters the region as it has been absorbed upstream. The relative contributions of each of these factors are explored in figure 5.15. It is clear however, that significant absorption requires high diffusivity. The high diffusivity allows the scalar to diffuse into boundary layers along walls, maintaining high absorption.

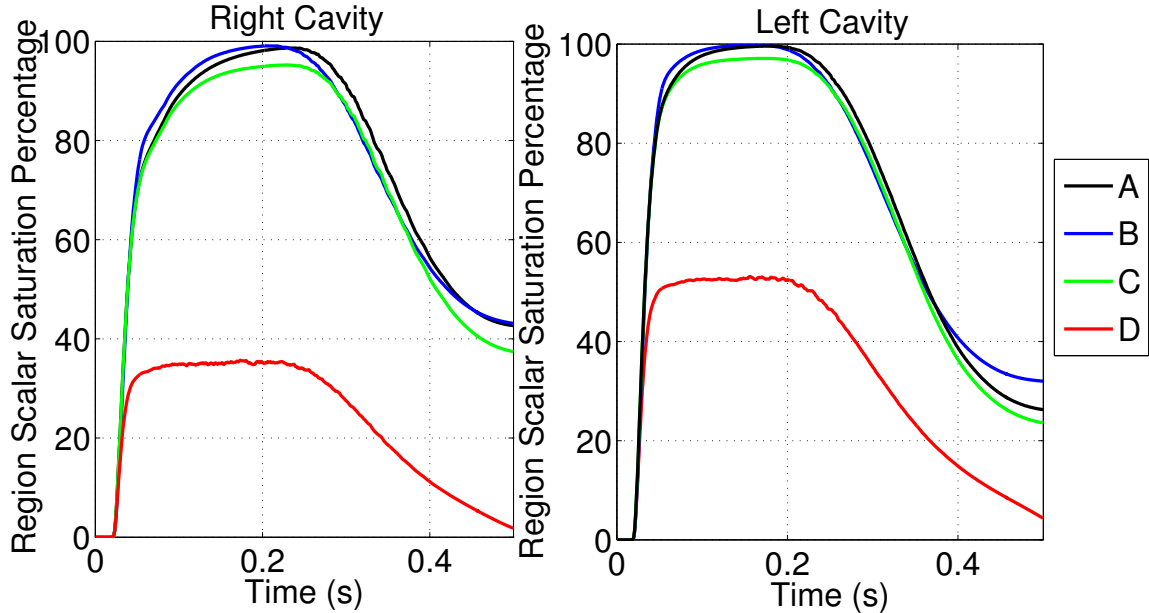


Figure 5.14: Volumetric saturation of the superior part of the nasal cavity shown in figure 5.8 for scalars A-D to defined in table 5.1. (A - low diffusion, non-absorbing, B - high diffusion, non-absorbing, C - low diffusion, absorbing, D - high diffusion, absorbing.)

The fluxes entering and exiting this upper region are shown in figure 5.15. No discernible differences are visible between scalars A, B and C, as the incoming flow is close to saturated, meaning the velocity field which convects the scalar dominates over slight

changes in concentration distribution. The recirculation in the anterior aspect of the right cavity is visible with little flux there in comparison with the left. This region takes longer to saturate with scalar. Scalar D is different, however. In the posterior aspect, the fluxes leaving the upper region (blue in the figure) are much less than in the other scalars. The velocity field is the same for all cases, so this difference is evidence of scalar depletion. The similarities in the anterior aspect show similar amounts entering the region, but much of this scalar must be absorbed at the wall in this upper region. This upper region is where the olfactory sensors are most densely located, so high absorption here increases the chance of scent detection.

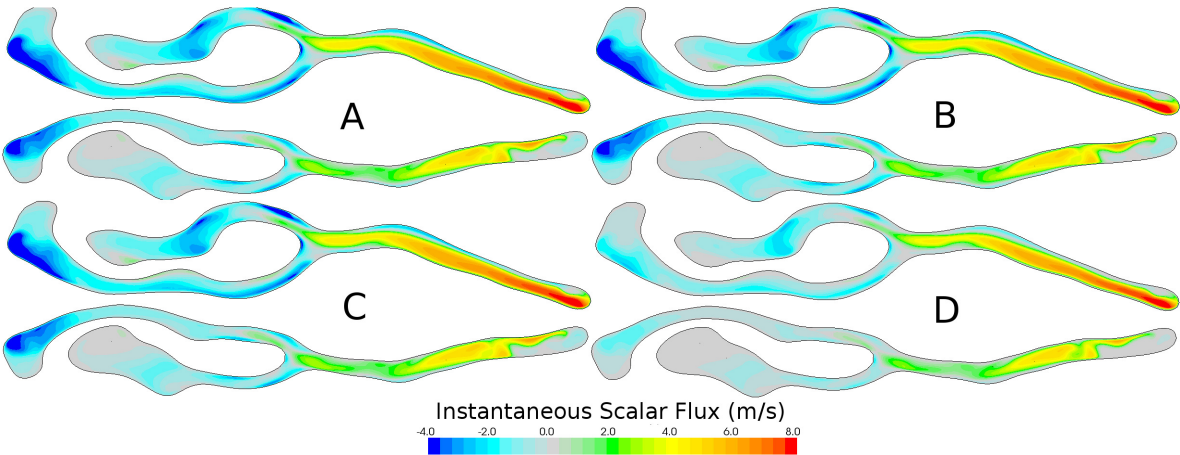


Figure 5.15: Instantaneous contours of scalar flux normal to the upper axial plane marked on figure 4.3 at 0.1 s ( $(\phi \mathbf{u} + D \nabla \phi) \cdot \mathbf{n}$ ). Positive values indicate upwards flux into the superior nasal region, whilst negative values indicate downwards flux out of this region. Grey values indicate no flux.

Figure 5.16 shows the fluxes of scalars C and D on plane 4 (figure 4.2) at 0.1 s. The first and third images represent the advection of the scalars ( $\mathbf{u}\phi$ ), whilst the second and fourth images illustrate their diffusion ( $D\nabla\phi$ ). The advective rates of the two scalars are reasonably similar, both in terms of patterns of flux and magnitude, although the flux of scalar D is a little lower here as it is depleted due to increased absorption. The scales on the diffusive plots are much lower (one million times lower for scalar C and two hundred times for scalar D), illustrating the contribution of each mechanism. Scalar D does diffuse relatively quickly at the boundaries, where there are large concentration gradients (the images depict total flux, not flux through the plane). Scalar C diffuses most rapidly in areas where the mixing of the flow generates high concentration gradients.

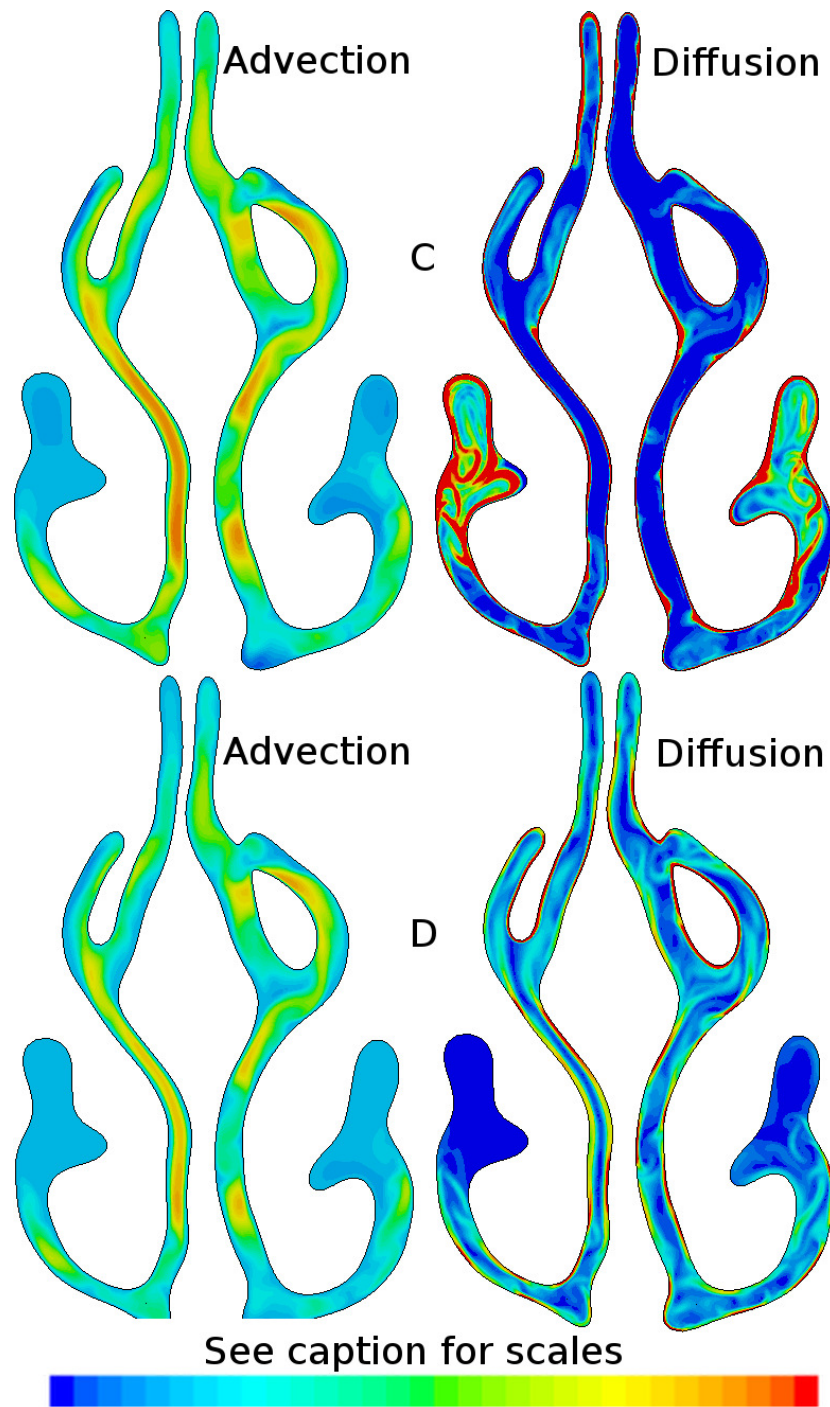


Figure 5.16: Comparison of scalar fluxes and mechanisms on plane 4 (figure 4.2) at 0.1 s. Clockwise from top left  $\mathbf{u}\phi_C$ , scale -2 to 10,  $D\nabla\phi_C$ , scale 0 to  $1 \times 10^{-5}$ ,  $D\nabla\phi_D$ , scale 0 to 0.05 and  $\mathbf{u}\phi_D$ , scale -2 to 10. (C - low diffusion, absorbing, D - high diffusion, absorbing.)

### 5.3 Absorption at the Wall

The surface fluxes of scalar D show where on the nasal wall the highest instantaneous absorption rates occur (figure 5.17). There is no flux in the nasal vestibule, as this region is not lined with mucosal cells and is more like the exterior dermis. This abrupt change in boundary condition is not realistic as the change in tissue is more gradual. Therefore, the initial high flux regions at the nasal valve may be exaggerated. Both cavities exhibit higher fluxes in the anterior aspect of the cavity with absorption peaks on both sides of each cavity, particularly at the head of the inferior turbinate and on the septal wall opposite. The highest fluxes are shown at the head of both middle turbinates, where the fast moving flow from the nasal valve impacts on the surface. Further peaks are visible in regions where the geometry protrudes into the flow.

Comparison with the surface flux of scalar C (figure 5.18) reveals much lower fluxes in the low diffusion case (note the scale on figure 5.18 is 100 times lower than that in figure 5.17). Some similarities exist between the pattern of fluxes however, with peaks visible at the head of both the middle and inferior turbinates and in the region of the nasal valve. In contrast to scalar D, the fluxes of scalar C remain at a more constant level throughout the cavity; less scalar is absorbed so more remains downstream.

Both scalar flux patterns in figures 5.17 and 5.18 can be compared to the patterns of wall shear stress in the nasal cavity (figure 5.19). The pattern on the anterior aspect of the right lateral wall is very similar in all three cases (upper left image). The separated flow region is apparent with low fluxes and shear stress, whilst below this the jet emanating from the nasal valve towards the head of the middle turbinate exhibits high flux and shear stress, with localised peaks in the same place for each measure. Superior to the middle turbinate, downstream of the recirculation region, the wall shear stress is relatively high compared to the flux of either scalar, suggesting that scalar has not penetrated this region at this time in the sniff profile. The low concentrations visible in figure 5.6 at this time support this finding. This reduced correlation between the surface patterns of scalar fluxes and wall shear stress is found throughout the posterior aspect of the cavities, particularly in the nasopharynx, where the wall shear stress increases as the geometry constricts.

The absorption of scalar at the wall has a significant affect on the concentration profile across the geometry. These profiles are plotted across plane 4 (figure 4.2) on lines extending from the inferior turbinate to the septum for each scalar, with the velocity

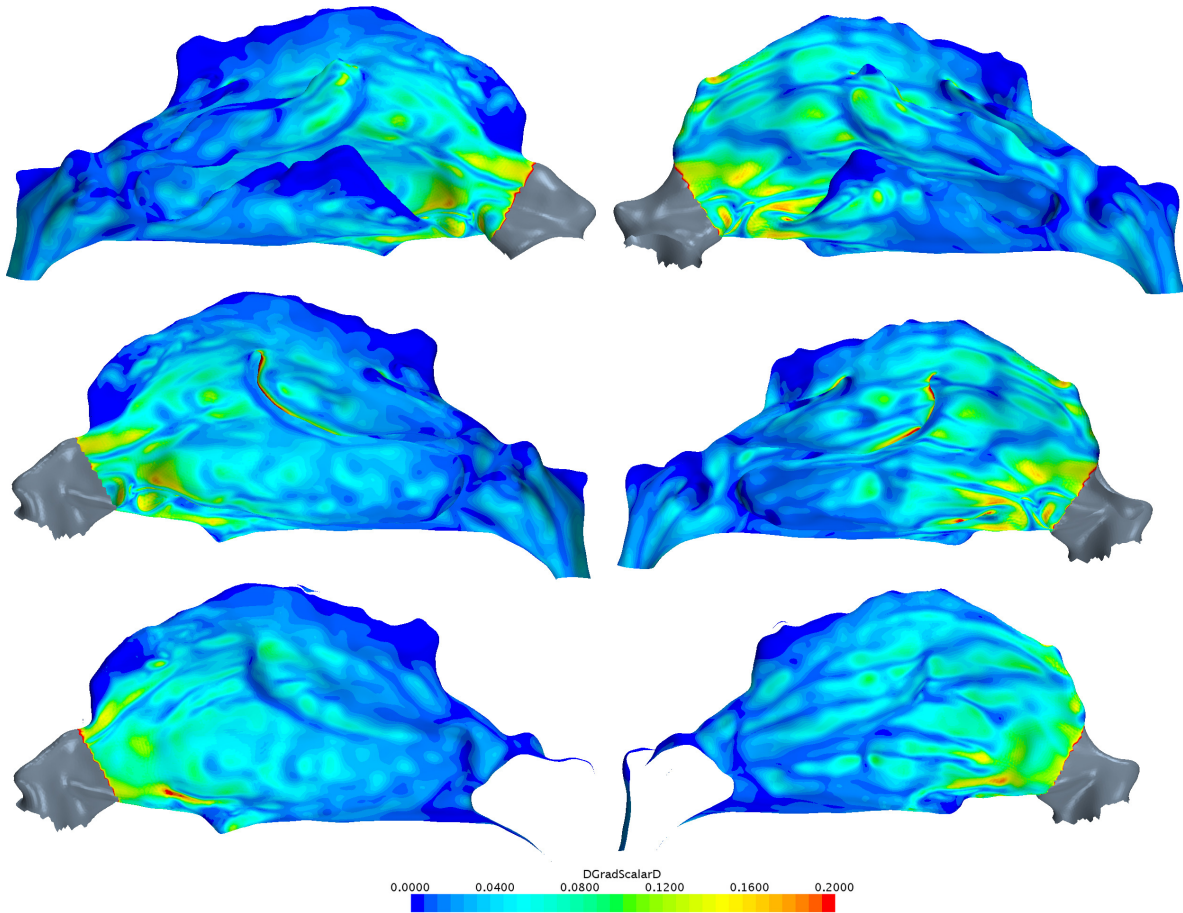


Figure 5.17: The flux of scalar D through the nasal wall ( $(D\nabla\phi_D) \cdot \hat{\mathbf{n}}$ ) at 0.1 s. Left column: right nasal cavity. Right column: Left nasal cavity. Top row: The lateral side viewed from the the outside of the nose. Middle row: The lateral side viewed from inside the cavities (highlighting the turbinates). Bottom row: The septal wall viewed from outside the cavities.

profile for comparison (figure 5.20). Scalars A and B are not absorbed at the wall and therefore are not expected to diminish in concentration there assuming that the scalar is able to fill the available geometry. On the right hand side of the graph representing the left nasal cavity, scalar A is not fully saturated, whilst scalar B is. This difference is due to the higher diffusion of scalar B allowing it to penetrate into a region where scalar A is unable to reach through advection. Both scalars C and D are absorbed at the wall, but the higher diffusion of scalar D means the boundary layer is much larger and the peak is reduced due to upstream depletion.

Comparison of the boundary layer thicknesses of these latter two scalar with the velocity profile is revealing. If laminar flow is assumed, the boundary layer thickness of the

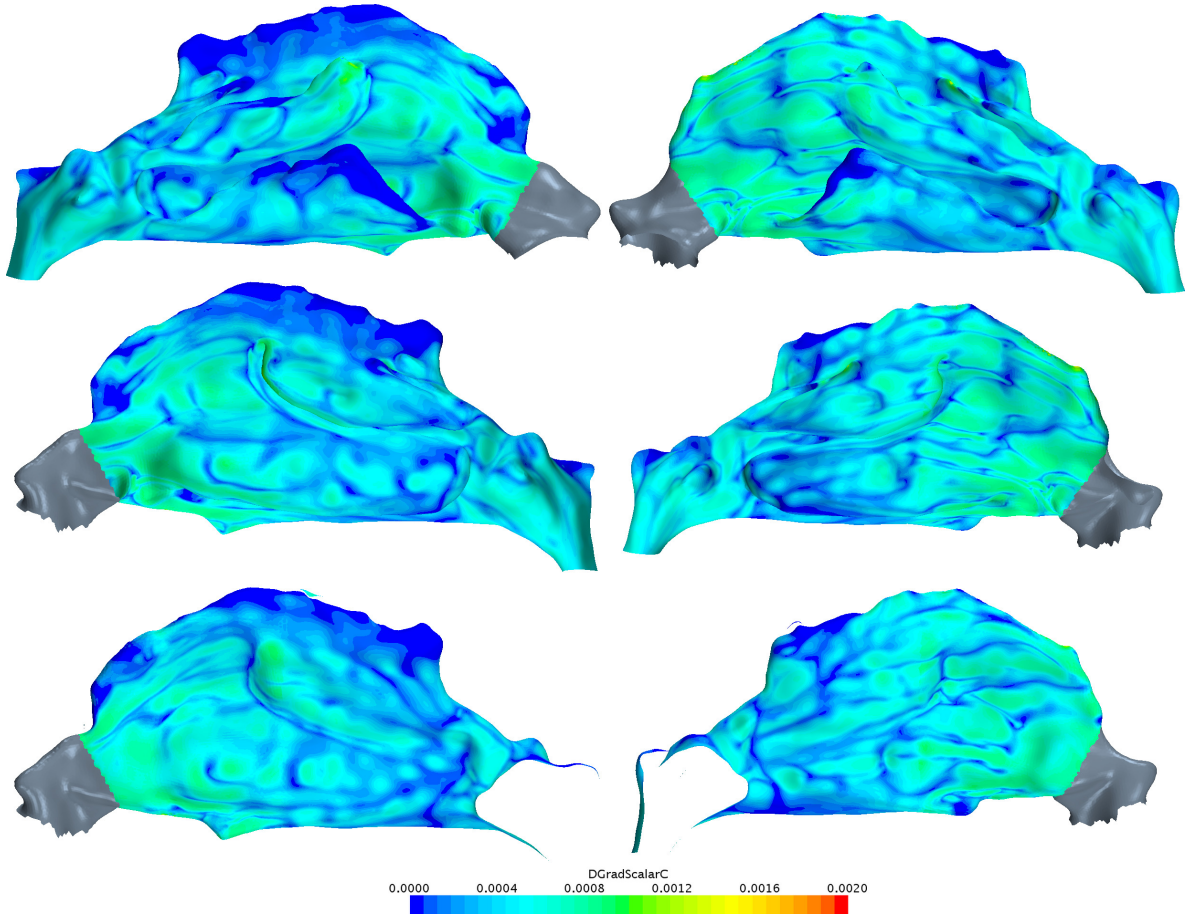


Figure 5.18: The flux of scalar C through the nasal wall  $((D\nabla\phi_C) \cdot \hat{\mathbf{n}})$  at 0.1 s. Left column: right nasal cavity. Right column: Left nasal cavity. Top row: The lateral side viewed from the the outside of the nose. Middle row: The lateral side viewed from inside the cavities (highlighting the turbinates). Bottom row: The septal wall viewed from outside the cavities.

scalars,  $\delta_\phi$  and velocity,  $\delta_U$ , should be related by the equation [98],

$$\frac{\delta_U}{\delta_\phi} = Sc^{\frac{1}{3}} \quad (5.1)$$

where  $Sc$  is the Schmidt number. This equation reveals that the boundary layer thickness should be similar for scalar D and the velocity, whereas scalar C's boundary layer thickness should be ten times smaller. This relationship is shown in figure 5.20, as the profiles for scalar D and the velocity are very similar, whilst scalar C's profile is much blunter.

The velocity boundary layer size is similar to that which analysis of a laminar flow

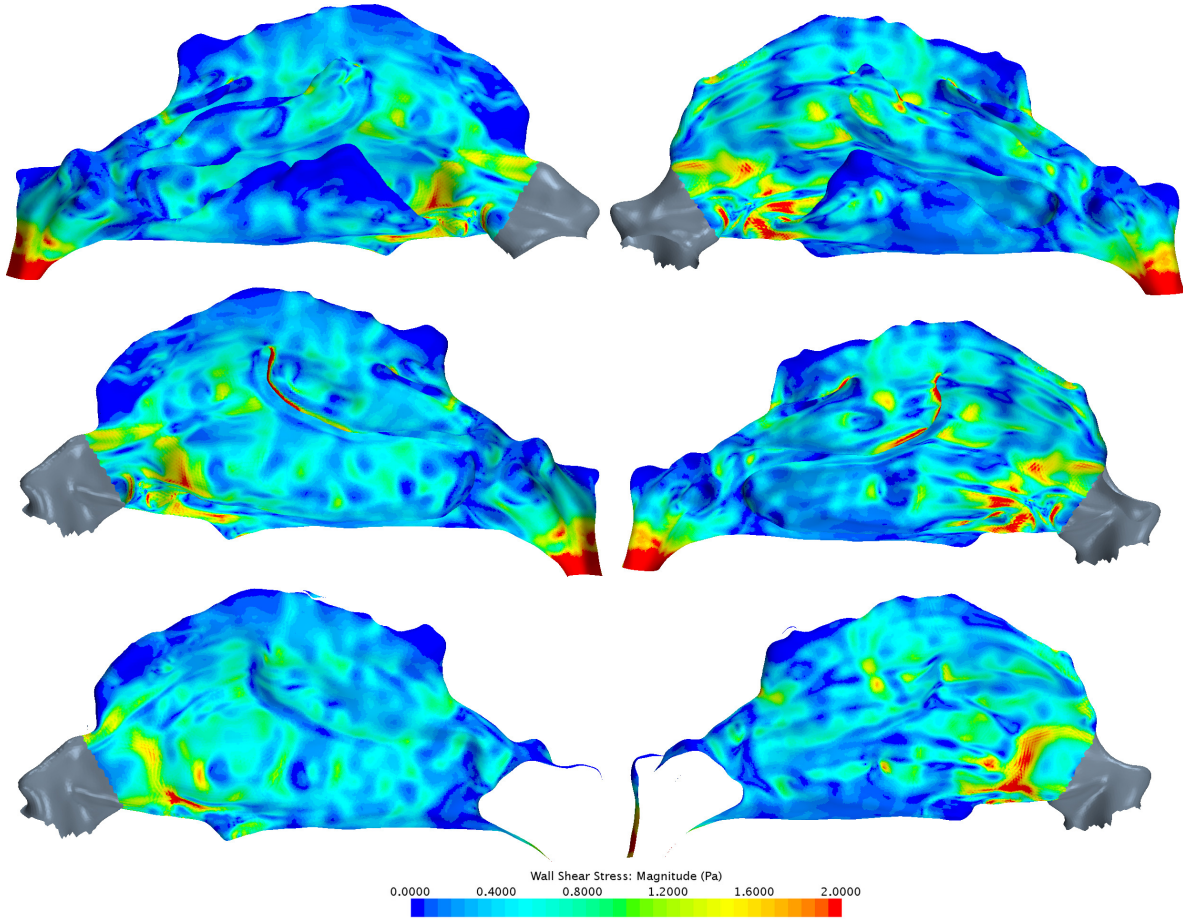


Figure 5.19: Wall shear stress on the nasal wall at 0.1 s. Left column: right nasal cavity. Right column: Left nasal cavity. Top row: The lateral side viewed from the the outside of the nose. Middle row: The lateral side viewed from inside the cavities (highlighting the turbinates). Bottom row: The septal wall viewed from outside the cavities.

across a flat plate would indicate, as given by Schlichting [98],

$$\delta_U \approx \frac{5x}{\sqrt{Re_x}} \quad (5.2)$$

where  $x$  is the distance over which the flow has been developing and  $Re_x$  is the Reynolds number calculated with  $x$  as the length scale. This equation gives an estimate for boundary layer thickness of approximately 0.65 mm in the right cavity, assuming the boundary layers were established at the head of the inferior turbinate. However, this model is less accurate in the left cavity, predicting a boundary layer thickness of 0.9 mm, where figure 5.20 shows the velocity profile to be blunter in the left cavity, with

smaller boundary layers than on the right, perhaps demonstrating that the flow is far from fully developed.

High resolution images of the scalar transport in this region are given in appendix C, figure C.1, with the mesh superimposed, showing the mesh resolution across the various boundary layers.

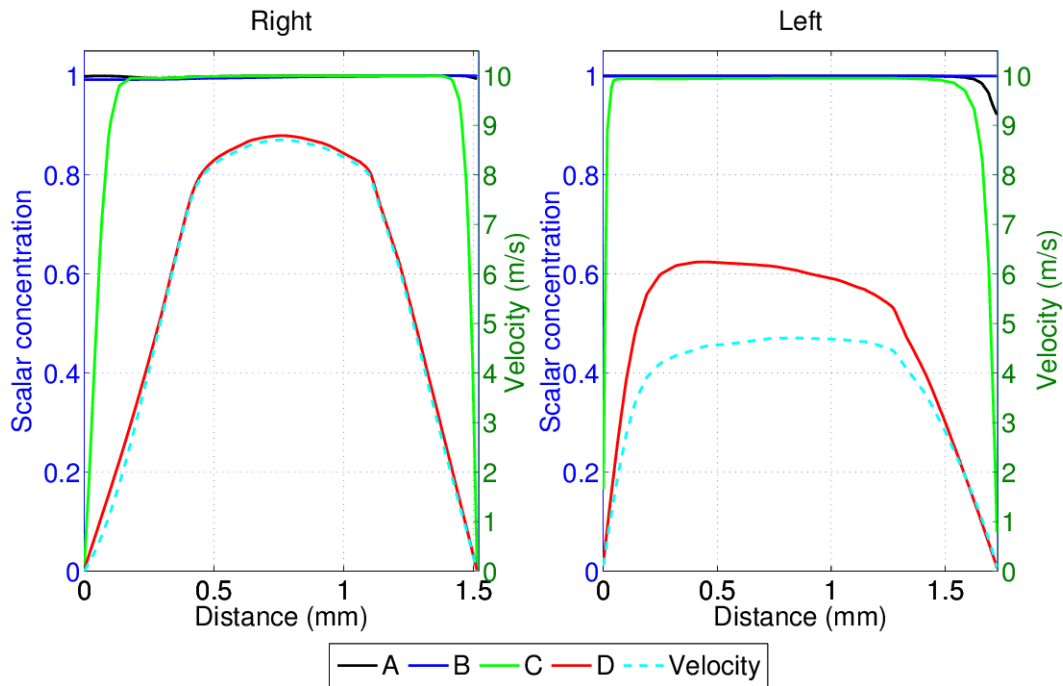


Figure 5.20: Concentration profiles of scalars A-D and the velocity profile on a line extending from the inferior turbinate to the septal wall on plane 4 (figure 4.2) at 0.1 s. (A - low diffusion, non-absorbing, B - high diffusion, non-absorbing, C - low diffusion, absorbing, D - high diffusion, absorbing.)

The scalar and velocity profiles in the glottis (figure 5.21) are rather different. The flow is not laminar in this region so the boundary layers are smaller. No scalar is fully saturated in this region at the three instances shown, as mixing with clean air originating inside the nose at 0.1 s and clean air rushing in from outside at 0.4 s reduce the concentration. Scalar D has also depleted to just 20% saturation at this point. The velocity profile is far more chaotic and is markedly different at the three instances shown and is therefore less similar to the profile of scalar D.

The scalar fluxes in the nose, pharynx and larynx are shown in figure 5.22. Scalar C exhibits similar levels of absorption in the descending airways as it does in the anterior aspect of the nose, due to the high velocities and therefore high wall shear stress values

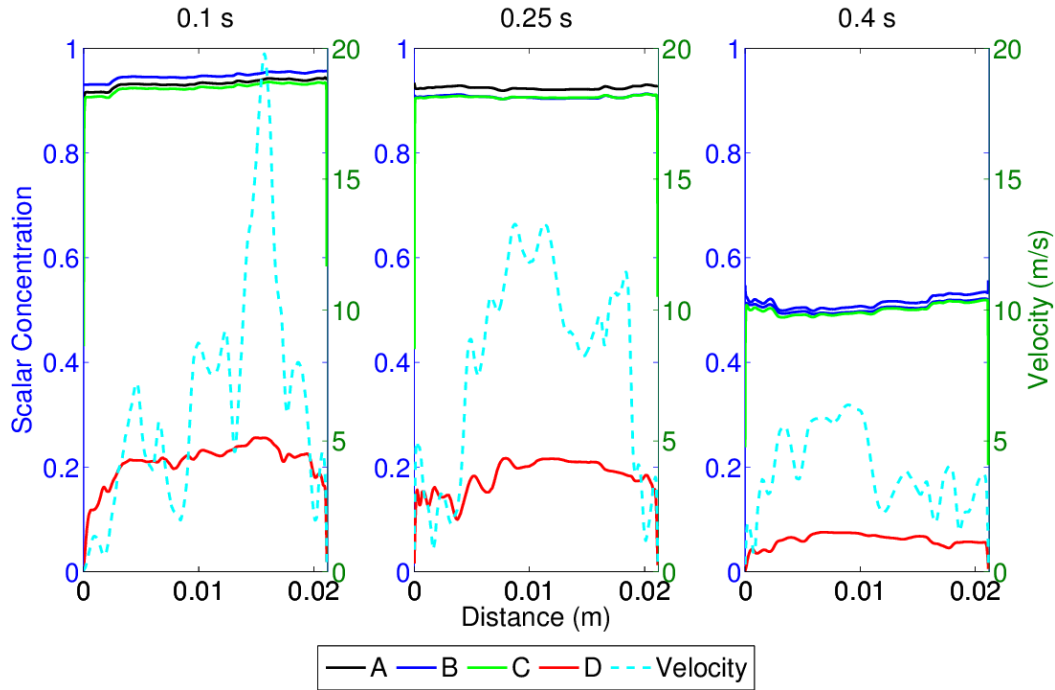


Figure 5.21: Concentration profiles of scalars A-D and the velocity profile on a line running in the anterior-posterior direction across the glottis plane 10 (figure 4.2) at three instants in the sniff. (A - low diffusion, non-absorbing, B - high diffusion, non-absorbing, C - low diffusion, absorbing, D - high diffusion, absorbing.)

in this region. Particularly high values are found at the superior side of the epiglottis which protrudes into fast moving flow. The high deposition rates on the epiglottis have been previously reported in larger particles by Sandeau et al. [97]. Scalar D is absorbed quickly, so less is available for absorption in the descending airways. However, a peak at the epiglottis is still observed as well as further patches of high absorption in the constriction above the glottis.

The images representing scalar C reveal the sensitivity of flux calculations to grid refinement. Scalar C has a much smaller boundary layer than the velocity or scalar D, as described by equation 5.1. It therefore requires higher resolution at the wall to resolve the scalar's boundary layer profile. The discontinuity in flux concentration in the trachea is due to a change in mesh refinement at this point (the lower trachea is less well refined than the upper airway). The same change is much less apparent in scalar D, which has a large and therefore less sensitive boundary layer.

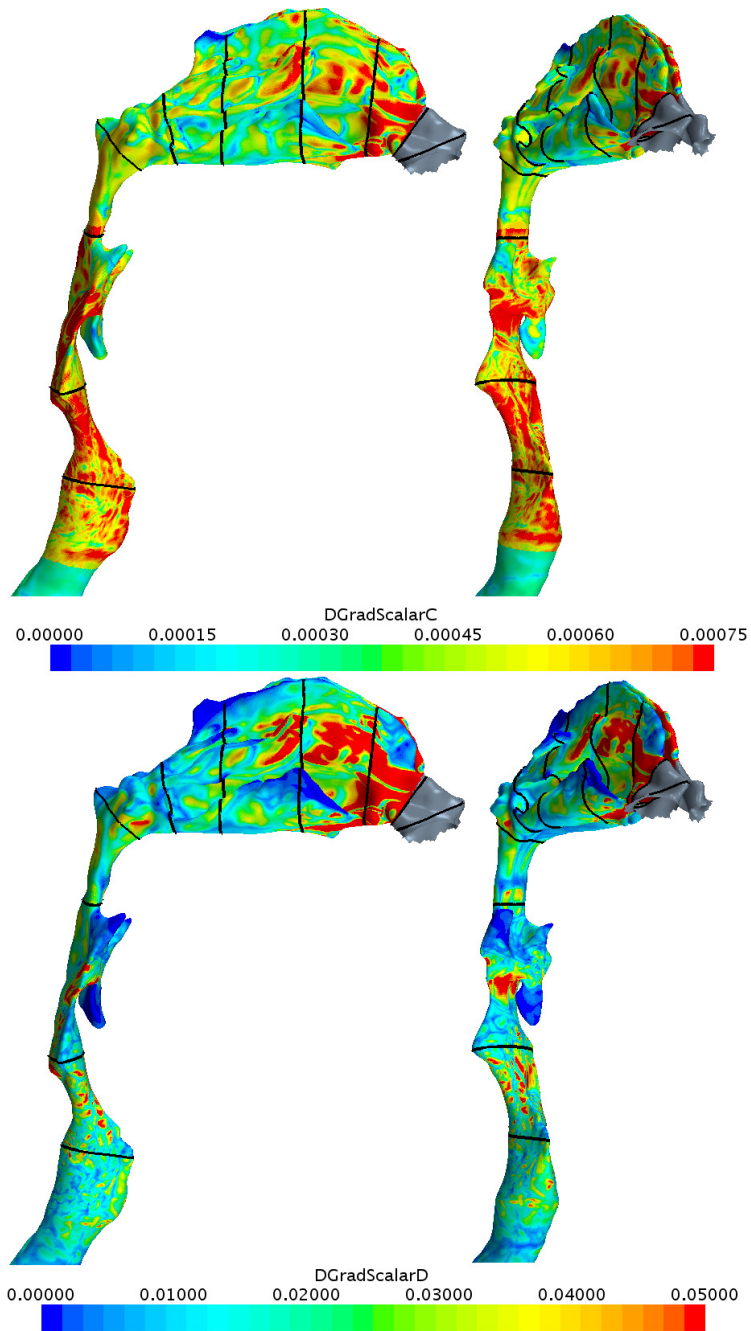


Figure 5.22: Surface fluxes of scalars C (top) and D (bottom) at the airway wall  $((D\nabla\phi_C) \cdot \hat{\mathbf{n}})$  and  $((D\nabla\phi_D) \cdot \hat{\mathbf{n}})$  at 0.25 s. The black lines represent the planes defined in figure 4.2.

## 5.4 Summary

The transport of four scalar species, originating outside the airways was analysed throughout the rapid inhalation manoeuvre described in chapter 4. Firstly, the transport of a non-absorbing and low diffusive scalar species was analysed. As its transport is dominated by advection, it allows analysis of the flow dynamics. Secondly, three additional scalar species were investigated, covering the extremes of absorption and diffusion and allowing the effect of each parameter to be analysed. Of these, three scalars (A, B and C) were found to behave very similarly, as the large difference in diffusivity made little difference in the non-absorbing scalars (A and B) and absorption was found to be limited in the low diffusion case (C). The scalar with high diffusion and absorption (D) was absorbed much more rapidly than the low diffusion case. Therefore, the concentration of this scalar was quickly depleted and absorption reduced in the downstream regions of the airways compared to the anterior nasal cavities.

The specific findings are:

- Transport of the scalar to the carina by the flow was achieved rapidly. Near saturation of scalar concentration at the carina was attained approximately 100 ms later than at a mid point in the nasal cavity.
- Local flow patterns are capable of significantly affecting scalar transport, as shown by the emergence of a prominent anterior recirculation in the right nasal cavity, which acted to delay the scalar advance in that area by 0.1s (figures 5.3 and 5.9).
- In the final 100 ms, during the decay period, a 15% greater concentration of scalar was retained in the upper right nasal cavity than in the left, indicating slower clearance from the right side (figure 5.9).
- Most absorption (>35% of flux into this region) occurs in the region of the nasal cavity into which both the inferior and middle turbinates protrude. This region has the highest surface area to volume ratio.
- In the descending airways, most absorption occurs in the superior half of the trachea (23% of flux into this region is absorbed); a region in which there is a great deal of mixing following the breakdown of the upstream jets.
- Boundary layer sizes are only well predicted by models based on flow over a flat plate where the flow is not influenced by separated regions, reattachments

and converging-diverging regions. However, the relationship between species and velocity boundary layers, based on  $(Sc)^{\frac{1}{3}}$  was found to accurately predict the relative sizes of the boundary layers.

The complexity of the detailed flow properties observed in this study is of significance to modelling and quantification of the transport of both gaseous and particulate reactive and passive species within the nose.

## 6 Characterisation of Airflow in Pathological Tracheas

The previous two chapters have characterised and quantified flow in a healthy anatomy. It is clinically important to understand the effects of pathologies on flow. In section 4.6, the uneven distribution of flow through the airways is explored. How do measures such as this change in pathological anatomies? How do additional constrictions impact the work of breathing? Does the flow become more disturbed? This chapter presents an analysis of flow in tracheas with goitres in order to investigate these questions.

The physics of inspiration in a normal airway anatomy consists of a confined jet issuing through the glottis and its subsequent dissipation. Pathological geometries may be constricted, deviated or a combination of both. This is the case with goitres, an enlargement of the thyroid gland which in compressive cases impinges on surrounding structures such as the trachea. The purpose of this study is to investigate how the flow pattern in the trachea is altered by deviation and constriction as exemplified by goitres and the consequences for metrics such as energy, pressure losses and turbulence. Geometric analysis is performed on several cases in order to characterise how the pathology has affected the anatomy. CFD simulations, using LES were performed on four pathological geometries along with a normal anatomy for comparative purposes. The simulated results were then analysed to quantify how the flow is affected in terms of the metrics discussed above and the novel metric ‘utilised area’, a measure which characterises how a flow uses the area available to it.

Quasi-steady simulations were employed in this study. To verify that this would produce accurate results, a constant inlet flow rate was instantaneously applied to the geometry investigated in the previous chapters, equal to that of the sniff profile at 0.13 s. After only  $\sim 0.02$ s, airway resistance and flow partitioning metrics throughout approached an equilibrium level of fluctuation. An instantaneous flow start shortens the initial transient and whilst unphysiological, is useful as a procedure to predict peak flow characteristics at lower computational cost.

### 6.1 Specific Geometry Capture

Anonymised CT scans of the neck and chest were obtained retrospectively from an image database. Ethical approval from local joint research compliance office was waived

and research and development approval was granted. Only scans containing the necessary anatomy and reported by a consultant radiologist as displaying a compressive goitre distorting tracheal anatomy from the first tracheal ring to below the carina were selected. Furthermore, only scans with a suitable slice thickness were chosen, to aid accurate surface extraction. All scans were segmented by a trainee ENT surgeon using Mimics (Materialise). This procedure produced 3D surfaces of the geometry which were then smoothed using Taubin's [113] algorithm (with parameters set to achieve bilaplacian smoothing) in VMTK (Vascular Modelling Toolkit 1.2).

All geometries were extruded at both the inlet (above the glottis) and at the outlets (below the carina) to ensure well defined boundary conditions. Flow measurements were only taken below the constriction at the glottis, to ensure that natural flow characteristics had developed [11].

## 6.2 Geometry Analysis

Five geometries were chosen for CFD simulation. One normal, labelled A, and four pathological cases, labelled B-E. These tracheas are shown in coronal and sagittal views in figure 6.1. Seven further tracheas underwent geometric analysis in order to quantify how representative the chosen geometries were of pathological cases. These are labelled Ia-d and IIa-c.

There is some variation in normal tracheal geometries, and those with goitres exhibit further variation due to the pathology: table 6.1 gives the means and extremes for a number of the relevant geometric quantities.

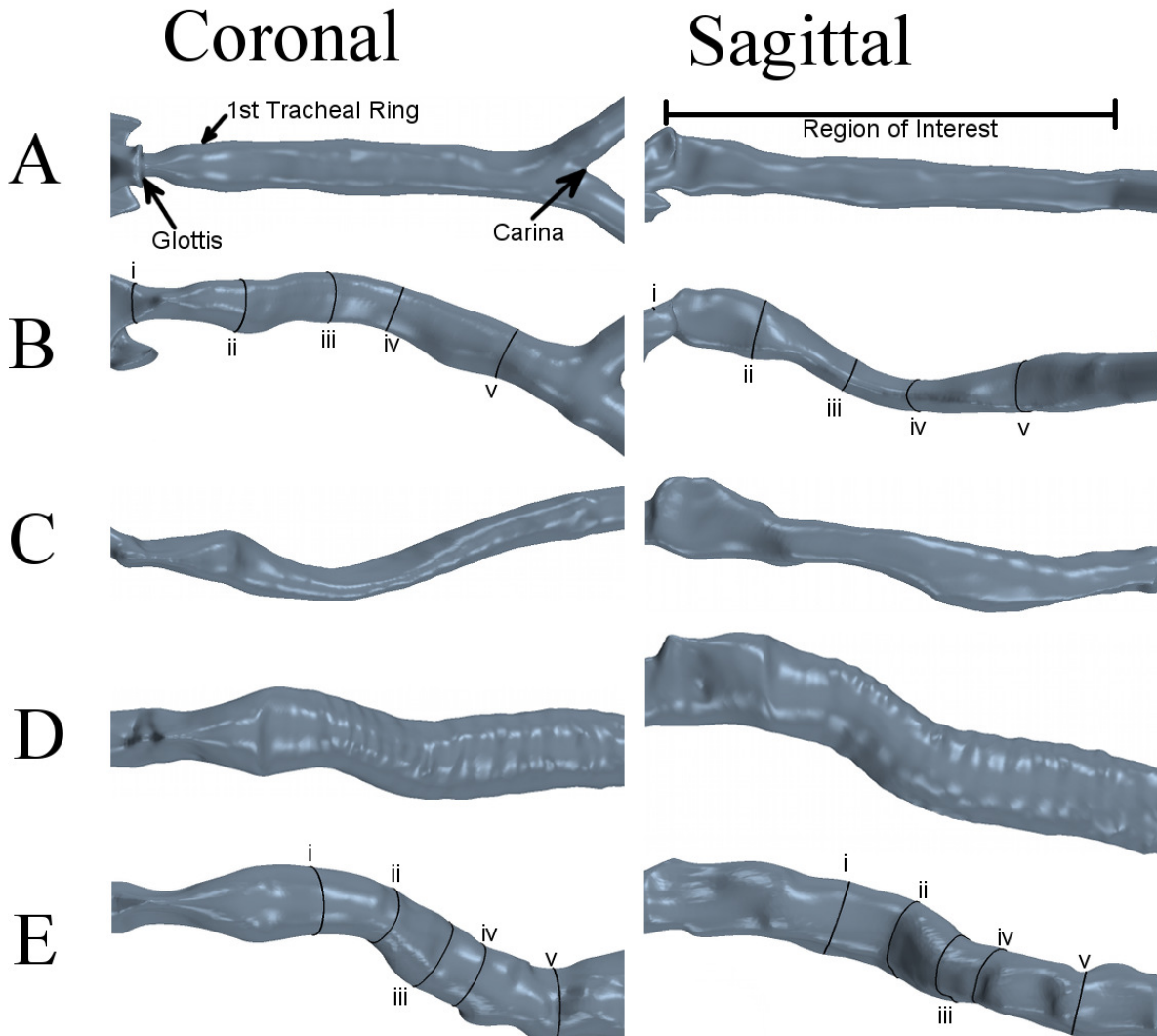


Figure 6.1: Sagittal and coronal views of tracheal geometries. A was described as normal, B and C show constriction, whilst D and E show large curvature. Each geometry extends above the glottal region shown here to ensure that natural inflow conditions have developed across the area of interest. Labels  $i$  to  $v$  illustrate the locations of planes discussed in figures 6.7 and 6.8.

The variation in curvature in two geometries is shown in figure 6.2 along with Frenet normal vectors along the centreline. The variations in these vectors show that the constriction caused by the goitre leads to multiple planes of inner curvature and are indicated by changes in direction of the Frenet normal vectors which point towards the centre of curvature. This variation is a measure of torsion. Despite geometry E having no appreciable constriction (table 6.1) the goitre alters the geometry in such a way that

Geometry	Mean $A$ mm <sup>2</sup>	Min $A$ mm <sup>2</sup>	Mean $\kappa$ m <sup>-1</sup>	Max $\kappa$ m <sup>-1</sup>	Mean $R$	Max $R$	Mean $r_{smax}$ mm	Min $r_{smax}$ mm	$L_C$ %
A	211	169	7	13	1.27	1.47	7.3	6.1	0
B	117	81	15	36	1.41	1.65	5.1	4.2	56
C	69	42	19	55	1.57	2.46	3.8	2.6	39
D	286	266	17	39	1.23	1.35	8.6	8.1	0
E	168	140	23	54	1.34	1.72	6.3	5.7	0
Ia	214	134	14	30	1.34	1.71	7.2	5.0	33
Ib	85	29	34	84	1.73	3.44	4.1	2.0	36
Ic	147	19	17	47	1.91	4.52	5.4	1.3	23
Id	91	21	31	65	1.71	2.91	4.0	2.4	33
IIa	208	173	15	41	1.18	1.42	7.5	6.3	0
IIb	178	151	20	34	1.25	1.54	6.8	5.9	0
IIc	254	209	10	25	1.75	2.33	6.9	5.6	0

Table 6.1: Mean and extreme geometric statistics for the considered tracheal geometries. Definitions are given in section 2.7. Featured geometries are labelled A-E. Additional geometries (not analysed in depth here) are shown for comparative purposes. Constricted geometries are labelled as Ia-Id and unconstricted as IIa-IIc.

the flow path is tortuous. Similar observations can be made about geometry D, whilst geometry C exhibits similar characteristics to B, figure 6.1.

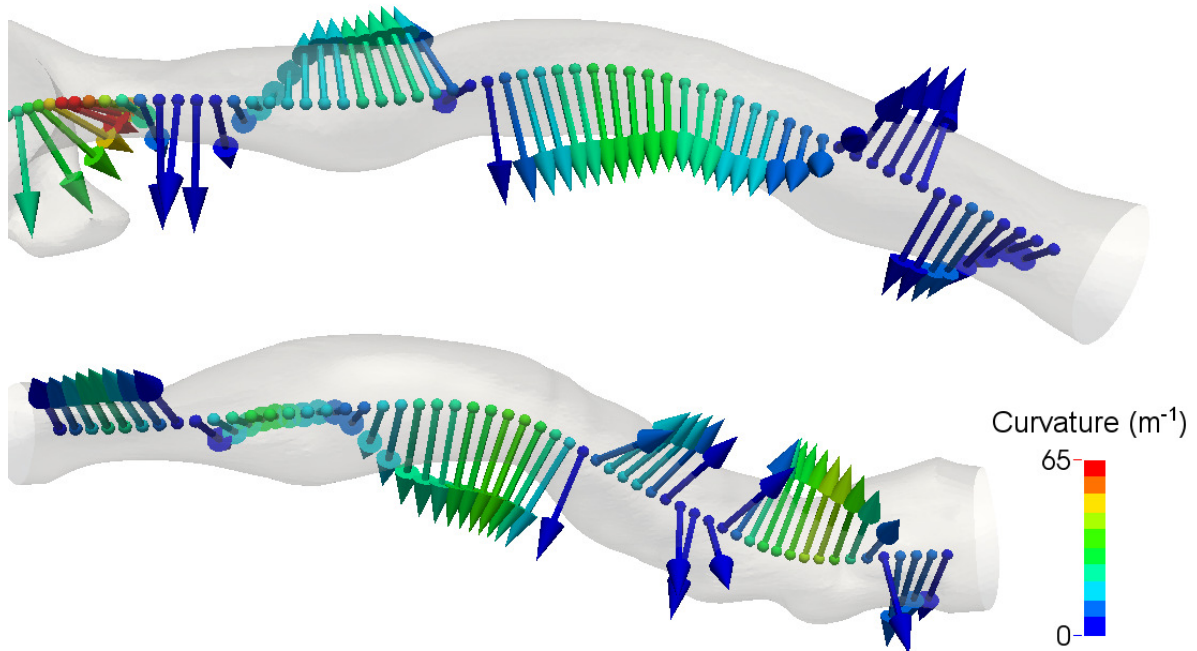


Figure 6.2: Frenet normal vectors along the centerlines of geometry B (top) and Geometry E (bottom) coloured by curvature,  $\kappa$ , which is related to these vectors by  $\mathbf{n} = \frac{1}{\kappa} \frac{d\mathbf{T}}{ds}$ , where  $\mathbf{n}$  is the normal vector at each point on the centerline,  $\mathbf{T}$  the tangent and  $s$  the arc length.

Figure 6.3 shows the variation of cross-sectional area along the length of all the considered tracheas. These areas are normalised by that at the first tracheal ring, which is also the site from which axial lengths are measured. Two clear groups emerge, those that include a constriction of more than 65% of the first tracheal ring area and those that only exhibit area variation within a similar range to that of the normal geometry. Of these classes, two of each type (B and C in the constricted case and D and E in the non-constricted case) were chosen for flow simulation and analysis, along with the normal geometry A. These selected geometries can be seen in sagittal and coronal views in figure 6.1.

The roundness, defined in section 2.7, is plotted along the length of each trachea in figure 6.4 and follows a similar pattern for four of the five geometries analysed. Each

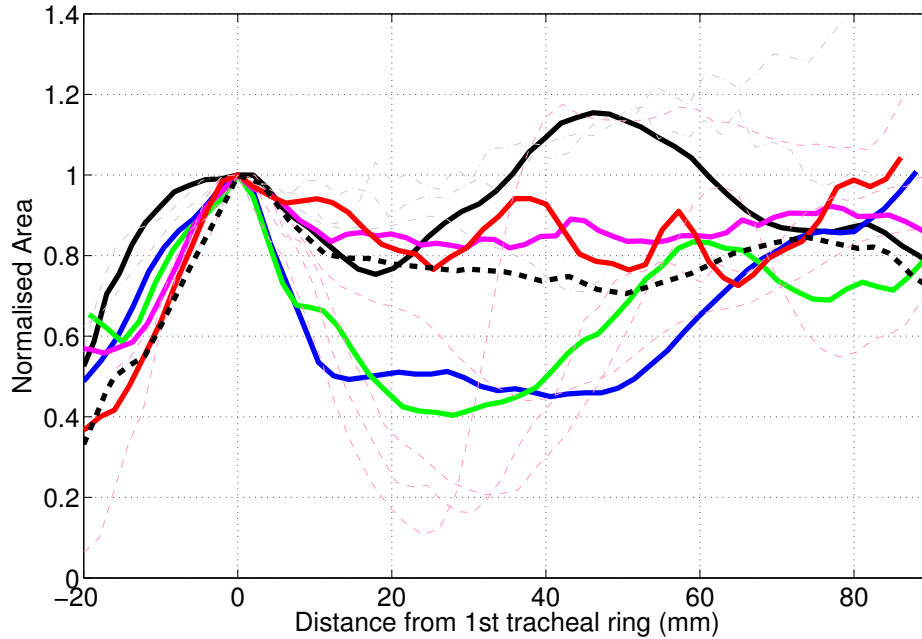


Figure 6.3: Cross-sectional area along the length of the trachea, normalised by the area at the first tracheal ring. The solid lines represent the 5 geometries A-E, whilst the dashed lines represent other geometries from the chosen database; geometries that exhibit a constriction, shown in pink and those whose area variation is within the normal range, shown in grey. The dashed black line represents the trachea analysed in chapter 4, another normal anatomy.

is far from circular through the glottis, but tends towards a circular cross-section at the first tracheal ring. From this point, the sections become less round through the subsequent tracheal rings, with even the normal case reaching 1.5, before tending back towards a circular cross-section through the mid tracheal region. Geometry B is the least round of those following the same trends as the normal case whilst the significant outlier, geometry C, demonstrates the deformations which take place as the goitre compresses the trachea.

Table 6.2 shows the percentage of each trachea’s length that is below a certain proportion of the first tracheal ring area. For the considered geometries, the same division into classes would be achieved with a proportion ranging anywhere from 50 to 70%. However, the severity of constriction reported would change considerably. For example, geometry Ic exhibits the most severe constriction of the dataset, but the constriction is very short. Only 23% of its length has an area less than 65% of the first tracheal ring, the shortest amount of those considered constricted. However, the constricted

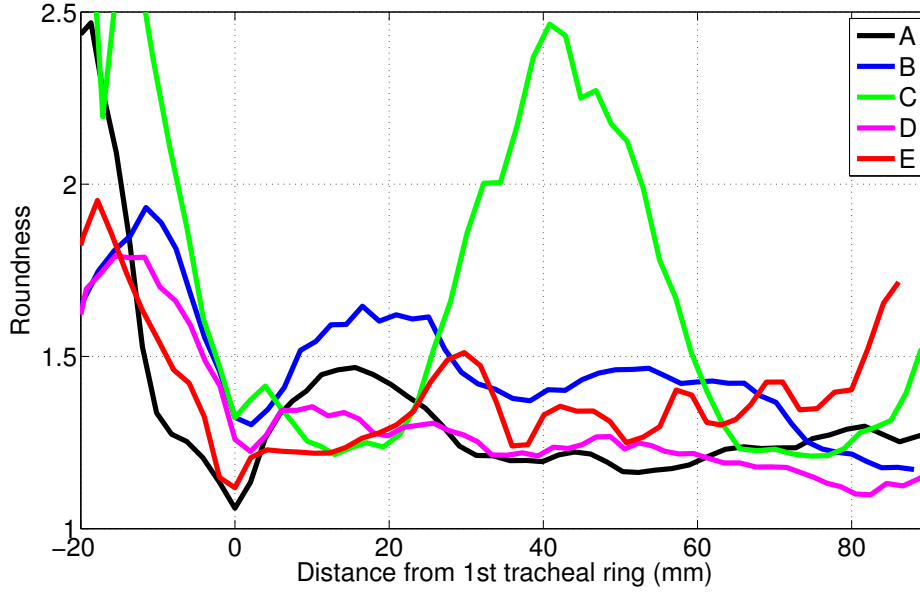


Figure 6.4: Cross-sectional roundness,  $R$ , along the length of the tracheas.

area is less than 15% of the first tracheal ring area, showing that both measures must be considered in assessing the severity of tracheal pathologies.

Eight of the twelve geometries had 85% or more of their length below that of the first tracheal ring. In the normal case A, it is just 34%, showing the need for analysis of a larger set of geometries to determine the normal proportions of tracheal anatomy.

### 6.3 Flow Patterns

Various metrics are important in quantifying the effects of goitre pathologies on breathing, for example, energy and pressure loss and turbulent quantities. In order to understand the mechanisms by which the geometry affects the flow and consequently these measures, detailed flow analysis is performed on three cases, representative of each class of deformity and a normal.

Figure 6.5 shows the mean and instantaneous velocities in geometries A, B and E. Each is scaled by the flow rate divided by the cross sectional area at the first tracheal ring. Geometry A (normal anatomy) exhibits a glottal jet emerging from the constriction at the glottis (a confined jet). The orientation of the “throat” of the glottis directs the jet towards the anterior wall where it impinges. The impingement of the jet onto the wall creates secondary flow vortices in the downstream region. Below this, the flow detached

	1	0.95	0.9	0.85	0.8	0.75	0.7	0.65	0.6	0.55	0.5	0.45	0.4	0.35	0.3	0.25	0.2	0.15
A	34	29	27	12	4	4	0	0	0	0	0	0	0	0	0	0	0	0
B	95	90	88	77	70	65	61	56	51	49	23	0	0	0	0	0	0	0
C	98	98	96	96	51	49	45	39	32	26	21	14	0	0	0	0	0	0
D	98	94	58	17	0	0	0	0	0	0	0	0	0	0	0	0	0	0
E	95	83	18	11	7	2	0	0	0	0	0	0	0	0	0	0	0	0
Ia	98	96	93	71	66	60	49	33	24	20	13	2	0	0	0	0	0	0
Ib	98	56	51	51	45	40	38	36	34	31	31	27	25	20	14	9	0	0
Ic	39	39	34	34	31	29	29	23	23	21	21	21	15	15	13	13	8	5
Id	88	75	66	62	58	37	35	33	31	29	27	24	22	18	14	12	6	0
IIa	95	91	77	34	20	15	0	0	0	0	0	0	0	0	0	0	0	0
IIb	14	8	3	0	0	0	0	0	0	0	0	0	0	0	0	0	0	0
IIc	43	6	0	0	0	0	0	0	0	0	0	0	0	0	0	0	0	0

Table 6.2: Constriction length ( $L_C$ ) percentages taken at different ratios of the first tracheal ring's area for all geometries A-E. Further geometries, not analysed in depth here are divided into two groups, those found to be constricted at 65% (Ia-Id) and those unconstricted at 65% (IIa-IIc).

and mixed, accompanied by decay of the secondary vortices. These observations are in agreement with previous work (e.g. Johnstone et al. [47], Ma and Lutchen [70], Lin et al. [64], Choi et al. [11]). Further velocity variations were small and depend on the local cross-sectional area. The instantaneous velocity shows some high velocity regions downstream of the glottis, which come from quickly rotating vortices shed from the glottal jet. The spacing of these suggest the oscillations of the jet are approximately regular.

In figure 6.5, Geometry B shows higher scaled velocities than A through the glottis, as the area at the first tracheal ring is smaller. The jet impinges on the anterior tracheal wall and adheres to it as the geometry curves and constricts. This results in a high velocity region extending further downstream than in the normal case. A similar flow pattern is observed in Geometry E, although the glottal jet impinges on the anterior wall of the trachea further downstream with the high velocity flow remaining biased to this side (due to the domination of centrifugal forces through the curve). Recirculation regions can be seen either side of the glottal jet and at the locations of high curvature, where the flow cannot remain attached. These post-glottal recirculations merge in the posterior of the lumen, forming a large separation region which prevents the jet from redistributing the high velocity flow. Therefore, the jet formed in the glottis travels much further downstream in geometry E than the other cases, which exhibit better redistribution of high velocity across the lumen.

The instantaneous flow pattern is broken up into several regions of high velocity, indicating high spatio-temporal fluctuations in the impingement and recirculation regions in all geometries and the additional separations in the pathological cases.

The local Reynolds and Dean numbers along the length of the tracheas are shown in figures 6.6a and 6.6b respectively for a flow rate of  $60 \text{ lmin}^{-1}$ . The Reynolds number curves scale with flow rate and their individual shapes depend only on the inverse of perimeter. At the lowest flow rate simulated,  $15 \text{ lmin}^{-1}$ , which is representative of normal breathing [56], all three geometries have Reynolds numbers of less than 2000 throughout their lengths and the mean of the normal case is 1450. Steady, circular-section pipe flow with a Reynolds number below 2000 is considered laminar. However, this value is based on steady flow and is not valid in the trachea as is seen in similar findings in arteries, where turbulent flow has been found at Reynolds numbers as low as 300 [60]. At the highest flow rate simulated,  $240 \text{ lmin}^{-1}$ , geometry B reached a Reynolds number of 32,000. Geometry B has the smallest perimeter of the three and hence the

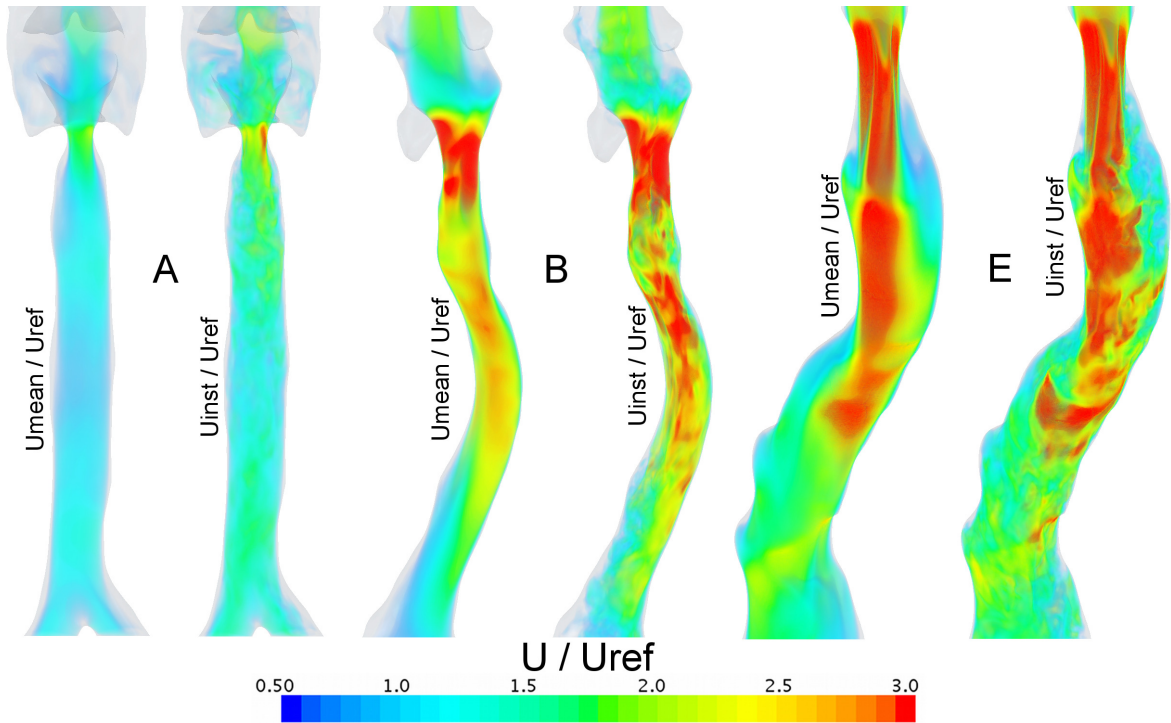
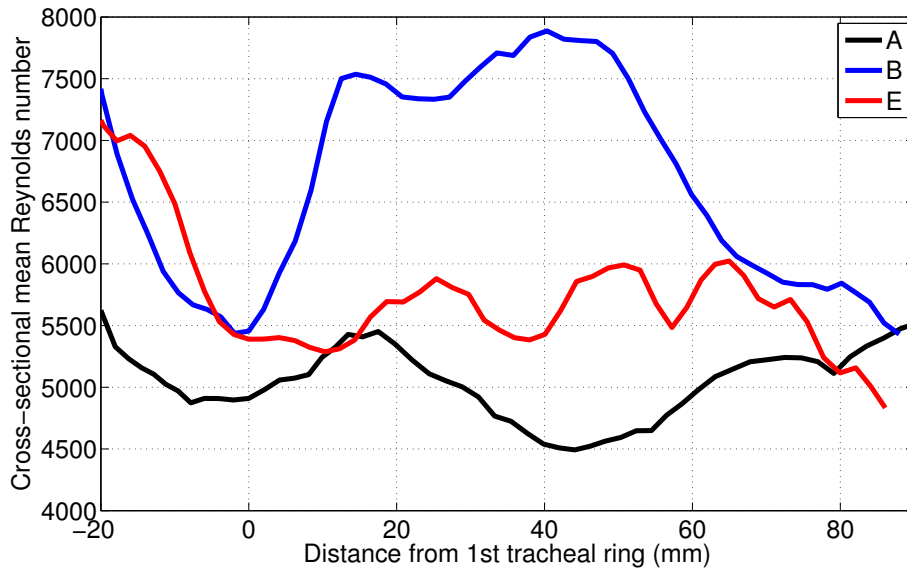


Figure 6.5: Volume renderings of mean and instantaneous velocities scaled by geometry specific reference velocities,  $U_{\text{ref}}$ , in geometries A, B and E at  $30 \text{ lmin}^{-1}$ .  $U_{\text{ref}}$  is the flow rate divided by the cross sectional area at the first tracheal ring in each geometry.  $U_{\text{ref, A}} = 2.19 \text{ ms}^{-1}$ ,  $U_{\text{ref, B}} = 2.78 \text{ ms}^{-1}$ ,  $U_{\text{ref, E}} = 2.59 \text{ ms}^{-1}$ . Geometries A and B are shown from the level of the tongue to the carina, whilst geometry E is shown from the glottis to the carina.

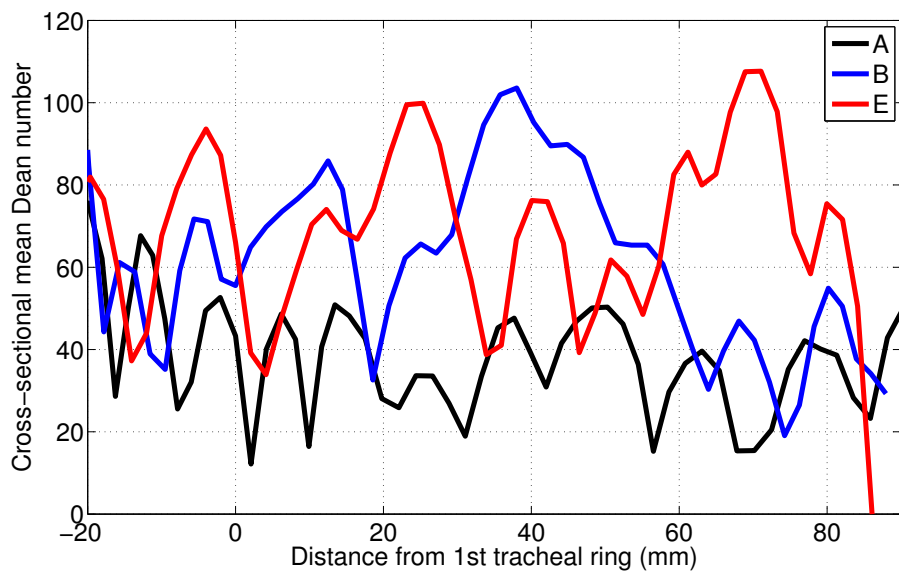
highest Reynolds number at any particular flow rate. The region of the geometry with the highest Reynolds number matches the constricted region apparent in figure 6.3.

The Dean number, figure 6.6b, provides a means to examine the relative impact of curvature on the flow. The effect of this measure is to highlight the increased curvature of geometries B and E compared with A, as the high curvature seen through the constriction in geometry B and the deviation in geometry E lead to peak values of Dean number double that found in the normal case, A. Geometry E exhibits three peaks in Dean number, each correlating to a section with high curvature. Therefore, although Dean number assumes a fully developed steady flow at the entrance to the curved region [23], it provides a measure of geometric influence not captured by the Reynolds number.

Figures 6.7 and 6.8 show mean static pressure contours on five planes (locations given in figure 6.1) for Geometry B and E with mean secondary flow streamlines overlaid. These



(a)



(b)

Figure 6.6: Cross sectional mean Reynolds number (a) and Cross sectional mean Dean number (b) along the lengths of tracheas A, B and E at  $60 \text{ lmin}^{-1}$ . The values scale linearly with flow rate.

streamlines indicate that the curved and constricted geometries lead to flow mechanics that are influenced by the confined jet, curvature and torsion. Curvature is responsible

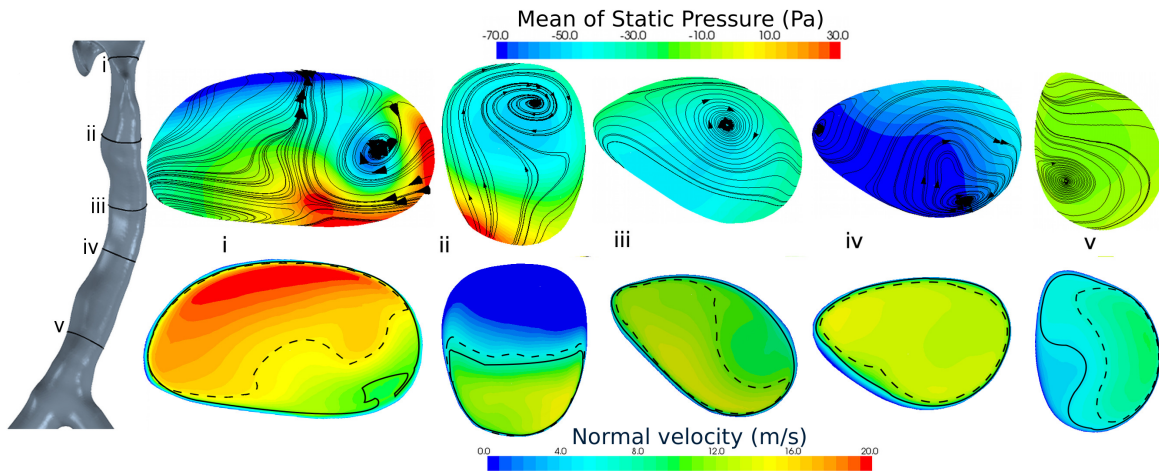


Figure 6.7: Upper: Contours of static pressure on cross-sections through geometry B. Secondary flow streamlines are overlaid in black. Lower: Planes coloured by normal velocity. The areas representing  $UA_{\max}$  are bounded in solid black lines and  $UA_{\text{mean}}$  with dashed lines. The anterior side of the tracheas is at the bottom of each image. The positions of the planes are shown in figure 6.1 and are not drawn to scale.

for the Dean-like vortices and torsion is responsible for the translation of these vortices out of the plane of symmetry. Pressure minima typically correspond to the centre of the vortices, indicating the location of cores.

In geometry B, plane *i* is above the glottis. In this region there are multiple sites of flow separation due to the complex geometry with openings into cavities such as the back of the mouth. From here the geometry constricts rapidly into the glottis, downstream of which is plane *ii*. Here, a single vortex within the recirculation zone on the posterior side corresponds with a pressure minima suggesting a strong vortical flow. The pressure field outside of the recirculation zone reflects the velocity field shown in figure 6.7. This vortex is still apparent in plane *iii*, forcing the high velocity flow to remain biased towards the anterior tracheal wall and redistribute in the azimuthal direction, resulting in the crescent shaped velocity profile visible on this plane. Plane *iv* is in the expansion region immediately downstream of the constriction. Two counter rotating vortices are formed as the flow separates. By plane *v* a single vortex remains, which again causes redistribution of flow in the azimuthal direction.

The region of jet impingement for Geometry B can be seen in plane *ii* of figure 6.7; the lower image shows a high velocity region along the anterior wall of the trachea. The goitre deforms the trachea laterally and anterior to the trachea's normal location. This causes the jet to impinge further upstream (0.8 times the glottal hydraulic diameter as

opposed to 2.1 times in the normal case) and at an angle almost normal to the wall. Posterior to the jet, the large low velocity region is observed. The curvature imposed on the trachea forces the jet to adhere to the inside of this curve, with some circumferential redistribution of the high velocity regions, as is apparent in plane *iii*, where the characteristic asymmetry of the flow in a curving and twisting geometry[18]. Plane *iv* shows the velocity more evenly distributed across the lumen, but as the trachea curves back towards the carina, a high velocity region is forced to the outer (posterior) wall and a second recirculation region forms, visible in plane *v*, which again demonstrates a horse-shoe like profile.

A different flow pattern is observed in geometry E, figure 6.2, which is deviated but is not constricted. In plane *i*, two counter-rotating vortices form (in the recirculation zone) as the jet is skewed towards the anterior wall. These vortices are centred at pressure minima. The vortex on the right (as viewed) is stronger and dominates by plane *ii*. Both vortices translate in the anticlockwise direction due to the torsional force (see changes in the Frenet normal vector of figure 6.2). This causes the high velocity region to redistribute in the azimuthal direction (figure 6.8). The vortex continues to translate in the anticlockwise direction and the velocity field moves with it (figure 6.8). By plane *iv* the vortex engulfs the entire cross-section as is also observed in plane *v*.

Geometry E demonstrates a glottal jet more closely aligned to the axis of the trachea than in the previous case. This change results in the jet progressing further downstream (impingement at 3.5 times the glottal diameter) and the impingement occurring more tangentially to the tracheal wall. Two counter-rotating vortices form posterior to the jet and merge into the large recirculation region seen on the left of plane *iv*. The abrupt curvature seen in the plot of Dean number (figure 6.6b) 25 mm below the first tracheal ring causes this glottal jet to recirculate in the posterior aspect of the tracheal lumen. This large recirculation acts as a pneumatic block, essentially narrowing the lumen available to the main flow.

Throughout both geometries the secondary velocities are much smaller than the axial velocities (at the location of maximum curvature 12.8% of the axial velocity).

The torsion is significantly larger than curvature (mean curvature and torsion for geometry B is 15.3 and 122.7 respectively); however curvature has a much greater influence on the flow mechanics (e.g. figure 6.8 where the high velocity region is forced away from the centre of curvature). This observation is backed up by previous studies that reported torsion to be of secondary importance compared to curvature in helical pipes

[36, 33, 1]. In particular, Alastruey et al. [1] determined that the torsional force on the flow is significantly smaller than the centrifugal force, since the latter depends directly on secondary flow velocities.

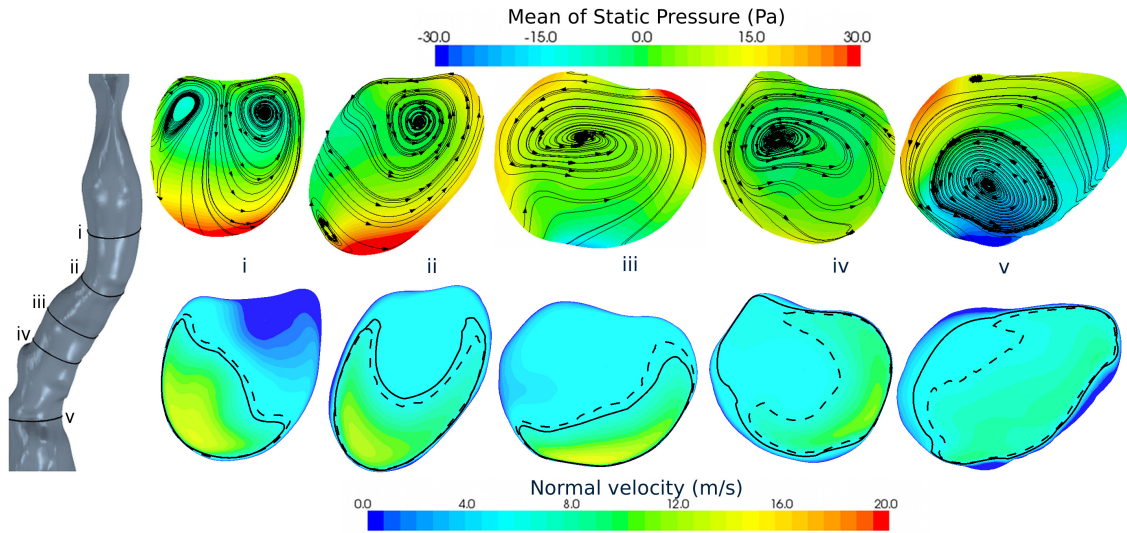


Figure 6.8: Upper: Contours of static pressure on cross-sections through geometry E. Secondary flow streamlines are overlaid in black. Lower: Planes coloured by normal velocity. The areas representing  $UA_{\max}$  are bounded in solid black lines and  $UA_{\text{mean}}$  with dashed lines. The anterior side of the tracheas is at the bottom of each image. The positions of the planes are shown in figure 6.1 and are not drawn to scale.

Figure 6.9 shows the percentage of the total area that  $UA_{\max}$  and  $UA_{\text{mean}}$  occupy along the length of each trachea. Each geometry shows a minima in both measures at or around the first tracheal ring, due to the glottal jet flowing into the expansion in the superior trachea. From this point in geometry A, both measures quickly increase and plateau, as the jet impingement causes mixing of the flow and redistribution of high velocity flow throughout the cross-section, confirming that the primary flow pattern in a normal trachea consists of mixing of the glottal jet.

Initially, a similar pattern is seen for geometry B, however  $UA_{\text{mean}}$  takes considerably longer to rise in the expansion region than in geometry A as the jet impinges on the wall and remains biased to that side as shown in figure 6.7. Through the post constriction expansion (50 mm to 65 mm), both measures can be seen to reduce, as the flow separates for a second time, forcing the bulk of the flow to bias the right side of the geometry (plane *iii* in figure 6.7).

The axial variation in  $UA_{\text{mean}}$  and  $UA_{\max}$  differs with flow rate.  $UA_{\text{mean}}$  responds more

slowly (i.e. further downstream) to changes in geometry as the flow rate increases, due to the increased inertia in faster moving flows.

The utilised area graph (figure 6.9) for case E has a low plateau through the first tracheal ring that remains 40 mm downstream where it reaches a minimum value. The cause of this behaviour is the extended glottal jet and posterior recirculation region, which force the glottal jet to travel further down the trachea than in the normal case. The large curvature seen in the Dean number plot (figure 6.6b) at around 70 mm below the first tracheal ring causes another separation and the utilised area decreases again above the carina. Hence, despite this geometry being relatively large and unconstricted, the geometry available to the flow is considerably reduced. Normal area utilisation is only achieved for approximately 18% of its length.

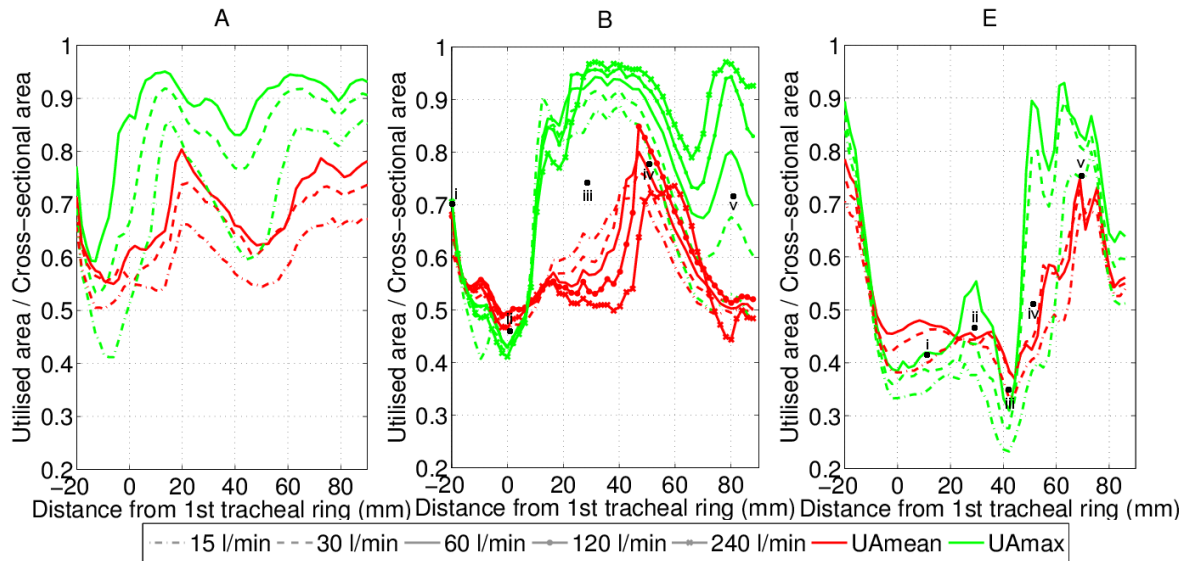


Figure 6.9: Utilised area ratios along the lengths of tracheas A, B and E

## 6.4 Flow Metrics

Integration of the energy flux through each plane indicates the total energy loss caused by driving flow through the tracheas. Figure 6.10, at a flow rate of  $60 \text{ lmin}^{-1}$  shows that the total losses in geometries B and E are approximately three times larger than in the normal case A. There is minimal loss in the normal case downstream of the first tracheal ring, whereas much of the losses in geometries B and E occur after this location and reasonably uniformly from the first tracheal ring to the carina. However,

there is an increase in the gradient of energy flux in geometry B in the region where the trachea expands after the constriction (around 50 to 60 mm), in geometry E the gradient increases at or just downstream of each peak in curvature. These increases in energy flux gradient indicate regions with higher losses and correlate to regions of high curvature and subsequent separation. Figure 6.5 shows several separations in the downstream region of geometry E, supporting the data here.

It is revealing to compare the work required to drive through the trachea to the total work of breathing, as this may indicate at what severity pathologies start to cause symptoms such as breathlessness. The work of breathing is made up of two components: elastic and resistive. In this study only the resistive component is considered, as it is the key contribution for obstructive airway diseases [7]. Milic-Emili and Petit [74] and Mancebo et al. [72] both independently found an average work of breathing in healthy subjects at an instantaneous flow rate of  $60 \text{ lmin}^{-1}$  to equal 0.35 W, whilst Loring et al. [69] report 0.25 W. Therefore, the work required to drive flow from the glottis to the carina accounts for approximately 10-15% of the total work of breathing. As this resistive work required increases threefold in the two pathological cases, it is apparent that the work of breathing will also have to increase significantly for the same flow rate of air.

? ] reported the resistance of their geometry to be four times higher in the region extending from the nasopharynx to carina than in the nose, whilst in the downstream airways, Pedley et al. [84] show the most significant resistances in the tracheobronchial tree to be in the trachea and the first few generations of bronchi. Therefore, the work necessary to overcome the tracheal resistance is likely to represent a significant proportion of the total work of breathing.

The logarithmic pressure-flow relationship for each tracheal geometry is plotted in figure 6.11. The mean total pressure loss is the difference between the average on planes across the glottis and above the carina. Each geometry exhibits a straight line demonstrating the power law relationship between the variables, however the exponents vary, as tabulated in table 6.3. Scaling the pressure values by either the glottal area or the square of the glottal area does not influence this result, indicating that this behaviour is not merely a function of the constriction at the glottis.

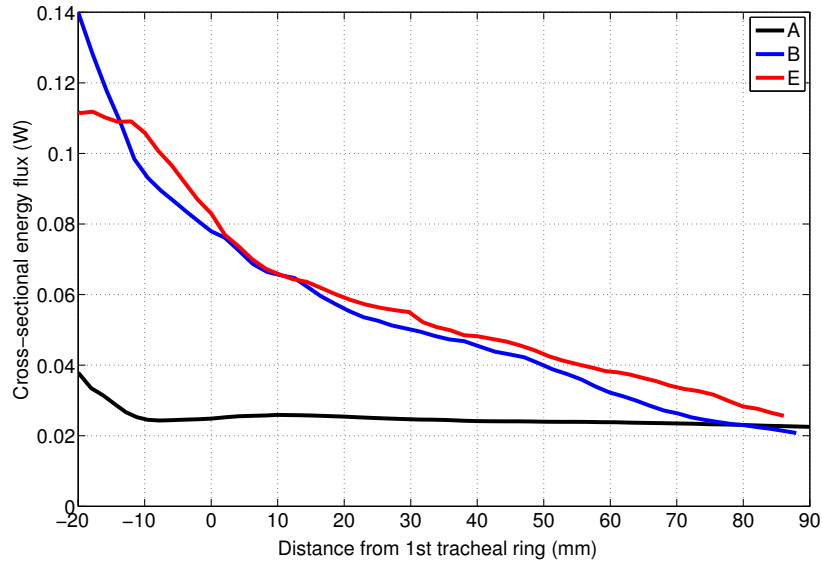


Figure 6.10: Energy flux through cross-sectional planes along the lengths of tracheas A, B and E at  $60 \text{ lmin}^{-1}$ .

Geometry	A	B	C	D	E
Exponent	1.77	1.85	1.86	1.97	1.86

Table 6.3: Exponents of pressure flow relationships for all geometries on which simulations were performed.

Both geometries that are curved, but not constricted (D and E) have high exponents, but low pressure loss at low flow rates, indicating that losses due to curvature increase more quickly with flow rate than those related to constriction. Geometry B, C and E all have similar exponents, despite different initial values and pathologies. Geometries B and E show very similar pressure losses at each flow rate, despite E not being constricted. This similarity shows different loss causing mechanisms are at work. Analysis of the exponents is considered more useful than quoting the coefficients of a  $\Delta p = aQ^2 + bQ$  curve as this provides limited insight into the fluid mechanics [119].

None of the geometric measures considered accurately predict these results, although Dean number, shows some correlation. The fixed relationship exhibited between pressure loss and flow rate in these geometries indicates that all flow rates are within the same flow regime, despite the Reynolds number values at  $15 \text{ lmin}^{-1}$  indicating a laminar regime, with the other flow rates transitional or turbulent.

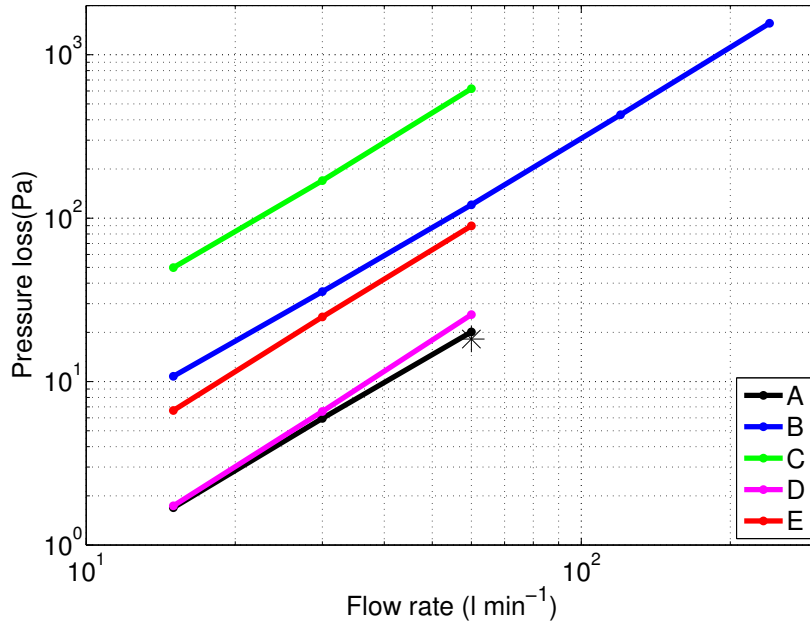


Figure 6.11: Pressure loss calculated as the difference in mean total pressure on cross sectional planes across the glottis and above the carina for five geometries. The black star represents the pressure loss found in the geometry analysed in section 4, between the glottis (plane 10, figure 4.2) and carina (plane 12, figure 4.2). Note: This value is lower than the pressure loss shown in figure 4.10a, which is measured from planes 7-12.

Flow rate	A	B	C	D	E
15 l min <sup>-1</sup>	0.007	0.043	0.199	0.007	0.027
30 l min <sup>-1</sup>	0.012	0.071	0.340	0.013	0.050
60 l min <sup>-1</sup>	0.020	0.120	0.620	0.026	0.090
120 l min <sup>-1</sup>	-	0.215	-	-	-
240 l min <sup>-1</sup>	-	0.390	-	-	-

Table 6.4: Resistances in Pa s ml<sup>-1</sup> recorded from the glottis to above the carina.

Table 6.4 shows the resistance values from the glottis to the carina for each geometry. These values are calculated by dividing the pressure loss and flow rates shown in figure 6.11. Both McRae et al. [73] and Smitheran and Hixon [105] report resting breathing rate resistances in the region of 0.006 Pa ml s<sup>-1</sup> for normal subjects, which match the value for the normal case at the lowest flow rate here. Comparison between the cases shows geometry C exhibits a resistance over 30 times higher than found in the normal anatomy, with B and E six and 4.5 times higher, whilst geometry D shows only a 30% increase in resistance.

The pressure loss from the glottis along the lengths of tracheas A, B and E are shown in figure 6.12 to highlight which geometric features cause significant pressure losses. Each geometry exhibits a large pressure loss after the glottis, peaking at or just upstream of the first tracheal ring due to the glottal jet and its impingement. There is then a pressure recovery, with the largest occurring in geometry B. The recovery is due to the redistribution of the high velocity flow to form a blunter velocity profile, as seen between planes *ii* and *iii* in figure 6.7 and the graph in figure 6.9. This pressure recovery and high velocity flow redistribution is also apparent in geometry E, however it happens over a longer length of the trachea, and hence the pressure recovery is reduced. In geometry B, the constriction dominates the downstream pressure losses, with steep gradients in the converging region at the head of the constriction (15 mm) and through the expansion downstream of the constriction (60 mm), as here a jet forms again and the flow is biased to one side, figure 6.9. Through the middle of the constricted region, the pressure gradient is elevated compared to the unconstricted sections, but not as highly as at its ends. Downstream of the expansion region, the pressure gradient approach similar values to the normal case, once redistribution of high velocity flow is achieved. Geometry E has several peaks in pressure gradient, each one correlating with a region of high curvature, as apparent in the Dean number, figure 6.6b. The pressure losses are shown at three flow rates for each geometry, the difference between the flow rates scales the curves by the exponents shown in table 6.3. Only subtle differences in the shapes of the curves are apparent, indicating the same flow regime throughout the range of flow rates studied.

The Poiseuille estimate for pressure drop at each flow rate was calculated along the length of the trachea. The incremental pressure drop between each cross-sectional plane  $dp$  depends on their areas,  $A$ , the flow rate,  $Q$  and the distance between them  $dx$ ;  $-dp = \frac{8Q\pi\mu}{A^2}dx$ . However, these Poiseuille estimates underestimate the pressure losses by more than an order of magnitude through each trachea at all flow rates of interest. This discrepancy is exacerbated in the two pathological geometries, B and E, as the Poiseuille estimate does not take into account the affects of curvature, such as separation, nor the losses due to jet formation in constricted regions and their subsequent impingements. Furthermore, no subglottal pressure recovery is found in the Poiseuille estimates, which is seen in all simulated cases. A correction term to the Poiseuille estimate for curved pipes was suggested by White [120] which increased the Poiseuille estimates by a mean factor of 1.2 across the geometries, but not significantly

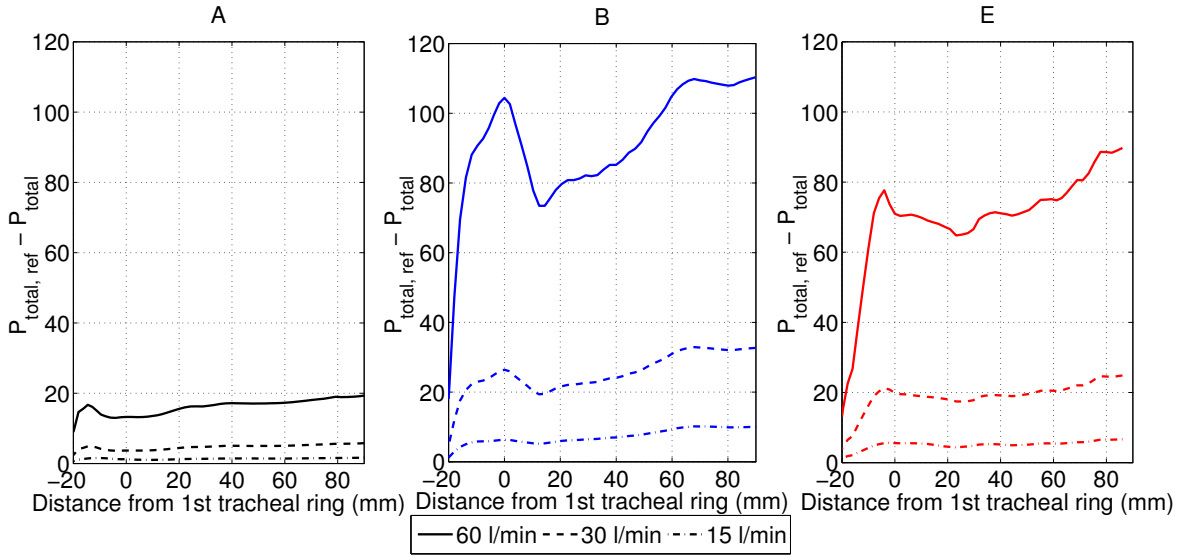


Figure 6.12: Total pressure loss along the length of the trachea.  $P_{\text{total,ref}}$  is the mean total pressure on a cross sectional plane in the glottis. Each plot shows three curves representing flow rates of 15, 30 and 60  $\text{lmin}^{-1}$ .

enough to allow accurate prediction of pressure losses.

Comparison with the pressure drops reported by Choi et al. [11] show a general agreement in the range of values reported, although there is some difference in the locations chosen to measure reference pressures from. The pressure losses simulated by Brouns et al. [6] in an idealised and unconstricted tracheal geometries compare well with the normal geometry, A, again allowing for the different measurement locations. Their 75% stenotic geometry gave a similar pressure loss to that of Geometry B, which is only constricted to 50% by area. Brouns found 50% stenosis produced a similar pressure loss to that of an unconstricted geometry. However, these idealised stenoses are not representative of the extrinsic compressions caused by goitres. Some discrepancies originate in the idealised nature of the stenoses, which do not incorporate curvature.

## 6.5 Turbulence & Unsteadiness

The variance of velocity is used to identify unsteady regions in the flow. Volume renderings of this quantity are shown in figure 6.13. Each geometry exhibits regions of high velocity variance downstream of the glottis and these represent the region over which the glottal jet wanders. There is a further region of unsteadiness in Geometry

A around the jet impingement region, but downstream of this zone the values remain low.

A similar pattern is observed in geometry B, with high values in the shear layers surrounding the jet and through the glottal jet impact zone, albeit with higher magnitudes. However, the flow does not then become steady. As the geometry curves, the flow separates and a recirculation is observed on the subject's left side. Through the most highly constricted region, there is a band of low variance, as here the flow is forced to fill the available area with a relatively blunt velocity profile and there is little scope for this to vary over time. A second recirculation zone occurs as the flow separates on the other side in the region where the trachea's deviation decreases.

Geometry E exhibits further regions of high variance through two regions of high curvature, both as it deviates away from its straight path and as it returns to the vertical. In the region downstream of the main bend in the geometry the tortuous geometry induces bands of elevated variance as the flow continuously detaches and reattaches to the luminal wall. The unsteadiness shown is not purely a function of the strength of the jet, as comparison of plots of variance of velocity taken at the same Reynolds number at the glottis display the same pattern.

The insets on the right of figure 6.13 show  $\frac{\sqrt{Var(\mathbf{U})}}{\bar{\mathbf{U}}}$ , the ratio of fluctuating to mean velocities. High value regions occur downstream of the jet impingement zone in the normal case, but are confined purely to boundary regions. In the two pathological cases, high values of this ratio exist across the bulk of the flow. Peaks above the glottis are caused by low mean velocities rather than high fluctuations.

Flow structures are shown in figure 6.14 through instantaneous  $\lambda_2$ . Through the glottis in geometry A, flow-wise structures are visible, as previously reported by Choi et al. [11]. However as the geometry expands to the first tracheal ring, the visible structures become normal to the flow direction and some horse-shoe features are apparent. These diminish in intensity as the flow moves downstream, until very little structure is visible in the flow above the carina before it bifurcates. An isosurface at normalised  $\lambda_2 = -10$  shows no structures are visible at this value further than two tracheal diameters downstream of the glottis.

Comparison between geometries A and B reveals the latter has a far richer pattern of flow structures. The shear layers surrounding the jet are picked out in regions of high vorticity. This is particularly evident at the throat of the glottis where there is a ring

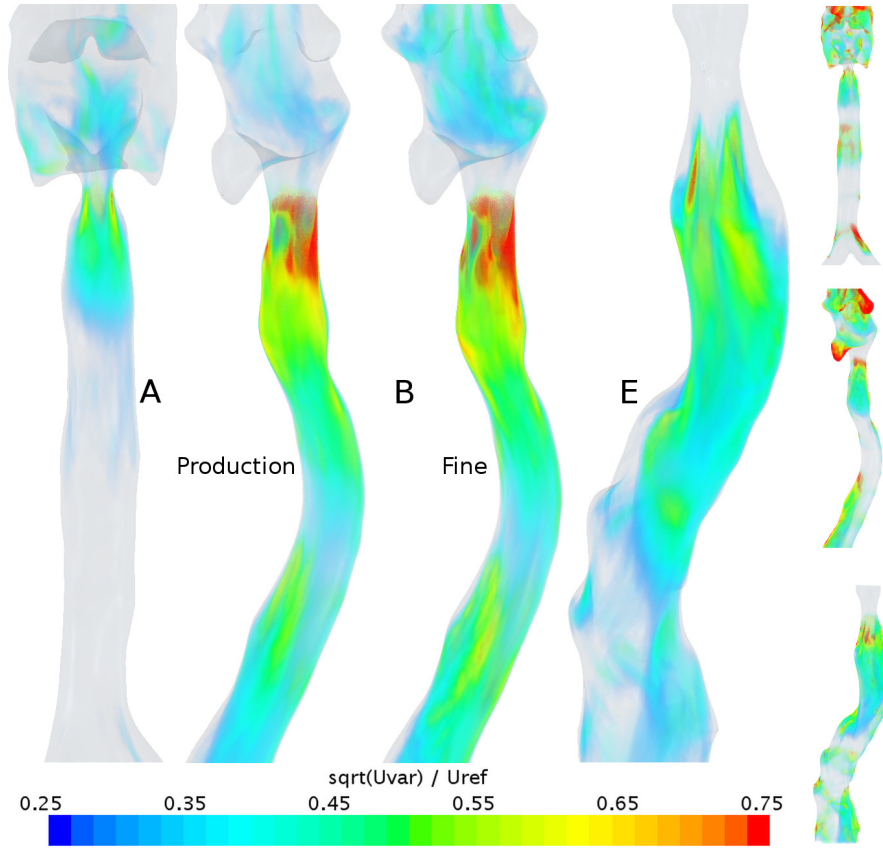


Figure 6.13: Volume renderings of the square root of the variance of velocity scaled by  $U_{\text{ref}}$  ( $\frac{\sqrt{\text{Var}(U)}}{U_{\text{ref}}}$ ) in geometries A, B and E at  $30 \text{ lmin}^{-1}$ . Geometry B is shown at two mesh and time step resolutions, production and fine, as described in section 3.1.2. The small insets show  $\frac{\sqrt{\text{Var}(U)}}{\bar{U}}$ , where  $\bar{U}$  is the local mean velocity.

like vortex. Similar structures have previously been seen for turbulent stenotic flows [116, 102]. The stream-wise structures through the glottis are visible again, although these break up quickly through the jet impingement zone, resulting in smaller hairpin like vortices oriented either transverse to or aligned with the flow.

Most significantly however, is the reappearance of flow structures downstream of the constricted section, as the flow cannot remain attached through the expansion and re-straightening of the trachea.

Geometry E does not exhibit the flow wise structures through the glottis seen in the other cases at this isosurface value as it is wider. However, a rich pattern of flow structures throughout the remainder of the geometry shows the complexity of the flow in this case. Large partial rings are visible downstream of the main curvature in regions

of high vorticity and these correlate with the regions of high velocity shown in the instantaneous velocity plot in figure 6.5. These features are caused by a perturbation in the geometry.

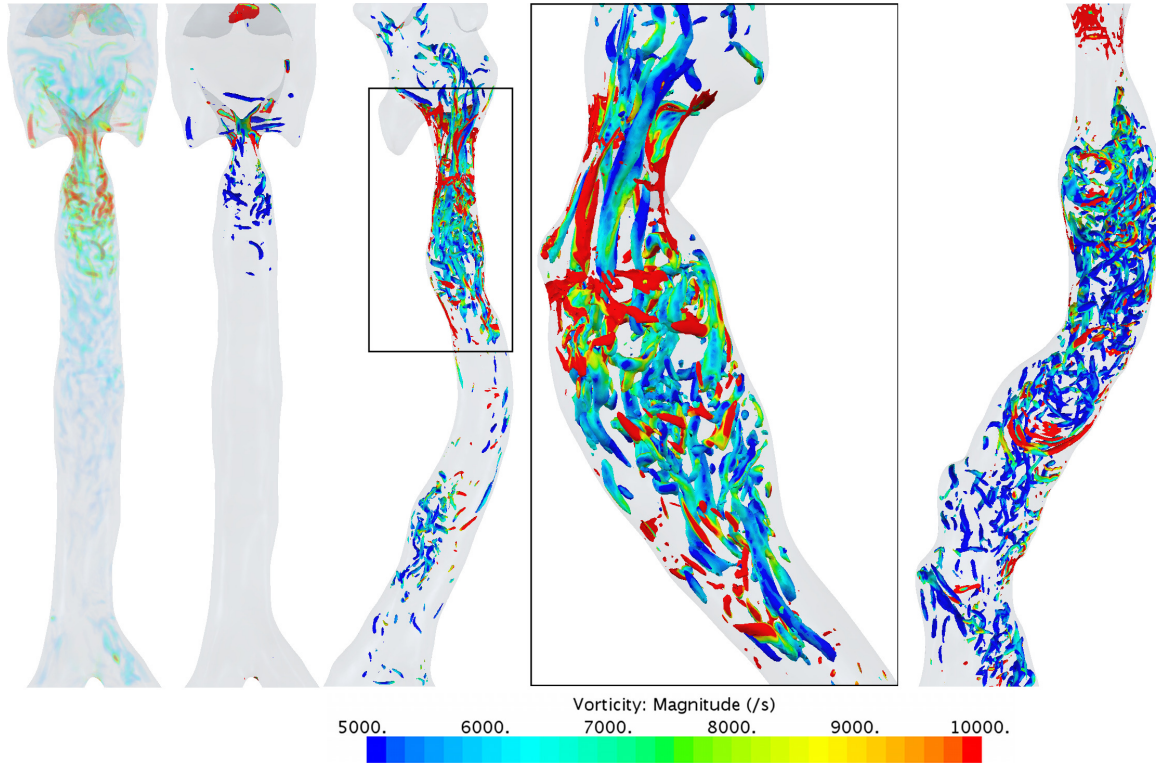


Figure 6.14: Left: Volume rendering of negative  $\lambda_2$  in geometry A. Others: isosurfaces of  $\lambda_2$  normalised by  $\frac{U_{ref}^2}{d^2}$  equal to -10 in geometries A, B, a detail of geometry B (rotated) and E. This isosurface is the same value as the red structures in the volume rendering (left), but this is included to highlight the weaker structures downstream. Isosurfaces are coloured by vorticity.

## 6.6 Summary

In this study flow mechanics analysis has identified two key mechanisms by which goitres affect the work of breathing. Four cases representing the range of pathologies and a normal case were subjected to detailed flow analysis. Both pathologies lead to significantly altered flow patterns when compared to the normal case. In particular, the following observations have been made:

- Both curvature and constriction strongly influence the flow.

- Pathological geometry leads to an increase in the work of breathing and a more disturbed flow.
- Predictions or estimations based on simple models such as orifice plates or Poiseuille flow miss certain features.
- Utilised area of the flow was found to be markedly different and lower in pathological geometries.

All subjects exhibit curvature and some are also constricted. The degree of constriction allows subjects to be classified into two groups: those with significant constriction, where the narrowest cross-sectional area along the trachea is less than 65% that of the first tracheal ring and those where the cross-sectional area variation is within the normal range. In severely constricted cases the minimum cross sectional area can be less than 10% of the mean area of the normal case. These additional stenoses produce jetting lower in the trachea.

The curvature in all the pathological cases is always higher than in the normal case (table 6.1). Curvature causes changes to the position and angle of the glottal jet impingement as well as additional separations downstream. Higher pressure losses occur in the vicinity of the location of maximum curvature.

Tracheal flow patterns are dominated by jet impingements and are therefore far from fully developed. The proposed measure “Utilised Area” quantifies the effects of pathologies on flow distribution, figure 6.9. The metric is lower in pathological cases due to flow separation downstream of curved and constricted regions, which causes higher frictional losses.

Goitre induced constriction is not axisymmetric and this renders orifice plate loss equations to only order of magnitude accuracy for the following reasons: glottal jets are directed onto the wall and this angle varies with pathology; the trachea exhibits curvature which induces further losses downstream; orifice plate predictions assume a sharp constriction, however the previous analysis has identified goitre induced stenoses to cover 23-56% of the trachea. The pressure-flow relationship shown in figure 6.11 does not correlate with either glottal or minimal area as would be expected in orifice predictions. Curvature has an important effect on pressure drop shown by the similarity shown in figure 6.12. The additional influence of Reynolds number is shown in the

elevated losses in the constricted geometry B. These observations are well characterised by the Dean number, which incorporates both Reynolds number and curvature.

An important consequence of these findings is that these pathologies to increase the work of breathing. This is evident in the increased pressure loss compared to the normal case and approximately three-fold increase in energy required to drive flow through them (figures 6.11, 6.12 and 6.10).

Pathological cases also exhibit increased disturbance shown in the instantaneous and variance of velocity plots (figures 6.5 and 6.13) and in the increased complexity of the flow structures in figure 6.14. Comparison of simulations at the same glottal Reynolds number show this to be a function of the deformation, rather than the strength of the glottal jet.

Use of an LES approach has demonstrated the capture of essential flow features seen in a highly resolved simulation without recourse to turbulence modelling and at an acceptable computational expense. However, increased computational power will render patient specific assessment feasible or pattern matching to a large database where the characteristic measures are incorporated. The clinical impact of this would be to enable surgeons to approximate the increased work of breathing in pathological cases and therefore to assess the likely result of any surgery to remove the goitre. At present, symptoms can be masked by lower lung issues such as COPD, making the effect of goitres difficult to assess. Goitre patients often tend to be high risk patients for surgery, as it mainly affects the elderly. Therefore a clear approximation of the impact of the goitre would aid the surgical decision making process.

Future work could focus on how variation in the parameters discussed is correlated with patient symptoms. For example, the increase in the work of breathing that subjects are able to compensate for could be quantified, highlighting at what point the removal of the goitre would improve respiratory compressive symptoms.

## 7 Conclusions

This work presents an investigation of the dynamics of airflow during inspiration in the human airways. Computational simulations were performed at high spatial and temporal resolutions in two related studies. The first study comprised an investigation of the evolution of airflow and transport of an inhaled scalar in the whole of the airways, from the nose to the carina, during a rapid, short inhalation. The second study considered the effect on the airflow of significant alterations in tracheal geometry associated with compressive goitre.

Previous studies have generally considered airflow to be steady and have not attempted to characterise the nature of the transitional or turbulent flows that occur in the different regions. The objectives of this work were twofold. Firstly the purpose was to apply highly resolved simulations to chart the overall course of the flow in a single, realistic anatomy of the airways from outside the nose to the trachea, to probe the appearance and nature of the spontaneous fluctuations associated with turbulence that arise in different parts of the airway and to find out how these influence flow efficiency and transport.

The purpose of the second part was to apply similar methods to probe the nature of flow in the trachea. Flow disturbances are normally most vigorous in this region, and pathological alterations in geometry can seriously compromise the efficiency of the trachea as a conduit of airflow to the lungs. A number of patient specific tracheal airways were investigated to illustrate how curvature and area restriction affects the nature of the flow and the mechanisms responsible for the losses in efficiency.

Both investigations considered flow rates that may be described as elevated significantly above the state of quiet, restful breathing, but below those corresponding to vigorous exercise. The motivation for this choice has been to consider manoeuvres more closely linked to those associated with inhaling medication on one hand and assessing resistance to flow on the other.

The investigations considering the whole airway revealed the time scales over which distinct flow patterns occurred and how these were associated with the different phases of the inhalation. The emergence of spontaneous flow disturbances and the nature of those fluctuations in different anatomical geometries were characterised. Several scalar species were introduced to determine the dynamics of transport. A non-absorbing and low diffusion scalar was used to map purely convective transport to various locations

within the airways. Among the notable findings was that transport to the carina was achieved in approximately 70 ms. This time is significantly less than would have been expected if the entire airways flooded with scalar (75%), revealing the non-uniform filling process. The other scalars considered either absorbing conditions or had a Schmidt number comparable to oxygen or nitrous oxide. For significant absorption, high diffusion is necessary.

A significant finding from the first part was that the flow regime in the trachea was established very rapidly. This allowed the dynamics of airflow in the trachea during the established flow phase to be investigated after the transients associated with an impulsive start have decayed. It was found that both curvature and constriction increase the effort necessary to inhale a certain volume of air and the level of disturbance in the flow.

Overall the key findings can be summarised as follows:

1. The time scales over which the patterns of flow develop have been identified in the airways, from outside the face to the carina using a highly resolved simulation. Three phases of inhalation, characterised as initiation, quasi-equilibrium and decay were found. Whilst all the variables of interest exhibit these same stages of flow, the duration of each varies for different quantities. For example, a constant regional distribution of flow within the nasal airways was found to depend on the establishment of local separations and was achieved significantly before the flow rate had reached its peak value. The asymmetric nasal cavities investigated allowed analysis of two forms of nasal flow commonly reported in the literature, as flow remains attached in the left cavity and separates in the right. This difference is a result of slight geometric variation in expansion after the nasal valve.
2. Flow in the nose is transitional in nature with mean cross-sectional turbulence intensity values reaching 9% in plane 4, figure 4.2, just posterior to the head of the middle turbinate. Local values can be much higher and depend on local flow patterns. For example, the separated flow in the right cavity led to a higher turbulence intensity than in the left cavity, where the flow remained attached (table 4.1). Flow in the descending airways was turbulent, with a mean turbulence intensity value of 25% in the glottis. Furthermore, characterisation of the frequency spectrum of fluctuating velocity revealed an energy distribution consistent with

turbulent flows, exhibiting both inertial and dissipative ranges (figures 3.3, 4.25 and 4.26).

3. Analysis of flow distribution within the airways revealed significant biasing of various regions and little flow in others. Cross-sections of the airways, such as those obtained through medical imaging were not found to be good indicators of the area available to the bulk of the flow. In the nose, little flow was found along the inferior meatus, with the bulk moving along the septal wall, although whether it biased the region around the middle or inferior turbinate depended on the upstream flow, particularly whether the flow separated at the expansion inferior to the nasal valve (figure 4.13). In the trachea, the flow was dominated by the glottal jet in the healthy case and the redistribution of high velocity flow across the lumen was reduced in pathological cases. The novel metric, ‘Utilised Area’ was employed to quantify this effect (figures 6.7, 6.8 and 6.9).
4. The transport of scalar species was used to represent the inhalation and deposition of nanoparticles or gaseous species. Four scalars were investigated, covering a range of diffusion and absorption characteristics. Three of the species were found to behave similarly, with near identical transport times and saturation profiles. The highly diffusive scalar was found to saturate specific volumes more quickly, as it filled slow moving regions through diffusion rather than advection (figure 5.14). Two scalars were absorbed at the airway walls, as would be the case for many inhaled species *in vivo*. However, they exhibited markedly different absorption characteristics due to their differing diffusion parameters. Only the highly diffusive scalar was significantly absorbed, as the low diffusion case was unable to diffuse across boundary layers to the surface. Only 10% of the highly diffusive species which was inhaled reached the carina.
5. Many large airway pathologies involve geometric changes to the airspace. One such pathology is the goitre. In compressive cases, this was found to curve tracheas and in some constrict them. Both types of geometric change were found to increase the pressure loss along the tracheas (figure 6.11), the work of inhaling a specific volume (figure 6.10) and led to more disturbed flows (figure 6.13 and 6.14). Regions of increased pressure gradient were found to correlate with high values of Dean number, which incorporates both cross-sectional and curvature values.

This work has established a benchmark of highly resolved simulations in the large airways. Future studies can use these results to test computationally cheaper and quicker simulations, such as that described in chapter 6 or using RANS methods to allow simulations to be performed on statistically significant populations or in clinically useful time scales. This would allow investigation of a wider variety of anatomies as well as different flow profiles such as the effects of repetitive sniffs and scalar transport in combined inspiratory and expiratory flow manoeuvres.

There is significant variation in normal nasal anatomy across the population. The ability to perform simulations in many geometries would allow the variation in normal flow patterns to be established and the sensitivity of different anatomical features quantified. A range of pathological nasal anatomies could be similarly analysed, providing a comparison of the effects each pathology has on several variables; the work of breathing, olfaction, particle deposition and filtration. Understanding of the latter two parameters across the range of anatomical variation would allow far more accurate dosing of nasally administered drugs than is currently possible. Modelling of the heating and humidification of the nose would also allow the regional burdens of these functions to be quantified in both normal and pathological cases and could potentially be used as an indicator for future diseases. Knowledge of the variation in flow patterns with geometric variations would provide surgeons with indicators of the effects airway surgery will have on the above functions in both critical and cosmetic surgery.

Similar possibilities exist in the trachea, as an extension of the work presented in chapter 6. As more anatomies are simulated and analysed, the geometric features which most significantly affect the flow can be identified, allowing patients to be assessed for surgical procedures based on geometric measures without the need for CFD simulations.

In addition, the current model lacks several aspects found in the *in vivo* case. Movement is not considered in the present study. Motion could be incorporated in two ways. Firstly, the prescribed motion of the chest during breathing affects the trachea. The motion could be measured in 4D medical imaging and then prescribed to the simulation with a moving mesh. Secondly the flow applies pressure forces on the airway which, in certain places, can collapse. This is particularly apparent at the nostril and the soft tissues of the pharynx. The effects of both these types of motion on the various measures of airway function could be quantified.

Additionally, advances in 3D printing allow further validation and comparison with experimental models. These models can be printed with surface accuracy of 5  $\mu\text{m}$  and

with build in pressure taps, avoiding some of the problems discussed in section 3.3. More pressure taps would allow surface maps of pressure to be recorded which can then be compared to the CFD simulation of the same geometry. Furthermore, a range of flow profiles can be quickly simulated by driving flow with a pump controlled by a stepper motor. The ability to open up these printed models and apply various lining to them also allows particle deposition studies to be validated.

## References

- [1] J. Alastruey, J. H. Siggers, V. Peiffer, D. J. Doorly, and S. J. Sherwin. Reducing the data: Analysis of the role of vascular geometry on blood flow patterns in curved vessels. *Physics of Fluids (1994-present)*, 24(3):031902, 2012.
- [2] N. Bailie, B. Hanna, J. Watterson, and G. Gallagher. An overview of numerical modelling of nasal airflow. *Rhinology*, 44(1):53, 2006.
- [3] C. G. Ball, M. Uddin, and A. Pollard. High resolution turbulence modelling of airflow in an idealised human extra-thoracic airway. *Computers & Fluids*, 37(8): 943–964, 2008.
- [4] A. J. Bates, D. J. Doorly, R. Cetto, H. Calmet, A. M. Gambaruto, N. S. Tolley, G. Houzeaux, and R. C. Schroter. Dynamics of airflow in a short inhalation. *Journal of The Royal Society Interface*, 12(102):20140880, 2015.
- [5] S. Berger, L. Talbot, and L. Yao. Flow in curved pipes. *Annual Review of Fluid Mechanics*, 15(1):461–512, 1983.
- [6] M. Brouns, S. T. Jayaraju, C. Lacor, J. De Mey, M. Noppen, W. Vincken, and S. Verbanck. Tracheal stenosis: a flow dynamics study. *Journal of Applied Physiology*, 102(3):1178–1184, 2007.
- [7] R. G. Carroll. *Elsevier’s integrated physiology*. Mosby Elsevier, 2007.
- [8] *Star-CCM+ User’s Guide*. CD-adapco, 8.04.007 edition, 2013.
- [9] X. B. Chen, H. P. Lee, V. F. Chong, and D. Y. Wang. Assessment of septal deviation effects on nasal air flow: a computational fluid dynamics model. *Laryngoscope*, 119(9):1730–1736, Sep 2009.
- [10] X. B. Chen, H. P. Lee, V. F. H. Chong, and D. Y. Wang. Impact of inferior turbinate hypertrophy on the aerodynamic pattern and physiological functions of the turbulent airflow; a cfd simulation model. *Rhinology*, 48(2):163, 2010.
- [11] J. Choi, M. H. Tawhai, E. A. Hoffman, and C.-L. Lin. On intra-and intersubject variabilities of airflow in the human lungs. *Physics of Fluids*, 21(10):101901, 2009.
- [12] J. Choi, G. Xia, M. Tawhai, E. Hoffman, and C. Lin. Numerical study of high-frequency oscillatory air flow and convective mixing in a CT-based human airway model. *Annals of Biomedical Engineering*, 38(12):3550–3571, 2010.

- [13] V. Chong and Y. Fan. Comparison of CT and MRI features in sinusitis. *European Journal of Radiology*, 29(1):47–54, 1998.
- [14] S. Chung and S. Kim. Digital particle image velocimetry studies of nasal airflow. *Respiratory Physiology & Neurobiology*, 163(1):111–120, 2008.
- [15] B. Cohen and B. Asgharian. Deposition of ultrafine particles in the upper airways: an empirical analysis. *Journal of Aerosol Science*, 21(6):789–797, 1990.
- [16] P. Cole, R. Forsyth, and J. Haight. Respiratory resistance of the oral airway. *The American Review of Respiratory Disease*, 125(3):363–365, 1982.
- [17] A. Comerford, V. Gravemeier, and W. Wall. An algebraic variational multiscale–multigrid method for large-eddy simulation of turbulent pulsatile flows in complex geometries with detailed insight into pulmonary airway flow. *International Journal for Numerical Methods in Fluids*, 71(10):1207–1225, 2013.
- [18] A. N. Cookson, D. J. Doorly, and S. J. Sherwin. Mixing through stirring of steady flow in small amplitude helical tubes. *Annals of Biomedical Engineering*, 37(4):710–721, 2009.
- [19] C. Croce, R. Fodil, M. Durand, G. Sbirlea-Apiou, G. Caillibotte, J.-F. Papon, J.-R. Blondeau, A. Coste, D. Isabey, and B. Louis. In vitro experiments and numerical simulations of airflow in realistic nasal airway geometry. *Annals of Biomedical Engineering*, 34(6):997–1007, 2006.
- [20] X. Cui and E. Gutheil. Large eddy simulation of the unsteady flow-field in an idealized human mouth–throat configuration. *Journal of Biomechanics*, 44(16):2768–2774, 2011.
- [21] C. Davies. Definitive equations for the fluid resistance of spheres. *Proceedings of the Physical Society*, 57(4):259, 1945.
- [22] A. Delafosse, M. Collignon, M. Crine, and D. Toye. Estimation of the turbulent kinetic energy dissipation rate from 2D-PIV measurements in a vessel stirred by an axial Mixel TTP impeller. *Chemical Engineering Science*, 66(8):1728–1737, 2011.
- [23] D. J. Doorly and S. J. Sherwin. Geometry and flow. In *Cardiovascular mathematics*, pages 177–209. Springer, 2009.
- [24] D. J. Doorly, D. J. Taylor, P. Franke, and R. C. Schroter. Experimental investigation of nasal airflow. *Proceedings of the Institution of Mechanical Engineers, Part H*, 222(4):439–453, May 2008.
- [25] D. J. Doorly, D. J. Taylor, A. M. Gambaruto, R. C. Schroter, and N. S. Tolley. Nasal architecture: form and flow. *Philosophical Transactions. Series A, Mathematical, Physical, and Engineering Sciences*, 366(1879):3225–3246, Sep 2008.

- [26] D. J. Doorly, D. J. Taylor, and R. C. Schroter. Mechanics of airflow in the human nasal airways. *Respiratory Physiology and Neurobiology*, 163(1-3):100–110, Nov 2008.
- [27] R. Eccles. A role for the nasal cycle in respiratory defence. *European Respiratory Journal*, 9(2):371–376, 1996.
- [28] D. Elad, S. Naftali, M. Rosenfeld, and M. Wolf. Physical stresses at the air-wall interface of the human nasal cavity during breathing. *Journal of Applied Physiology*, 100(3):1003–1010, 2006.
- [29] D. Elad, M. Wolf, and T. Keck. Air-conditioning in the human nasal cavity. *Respir Physiol Neurobiol*, 163(1-3):121–127, Nov 2008.
- [30] R. Fodil, L. Brugel-Ribere, C. Croce, G. Sbirlea-Apiou, C. Larger, J. Papon, C. Delclaux, A. Coste, D. Isabey, and B. Louis. Inspiratory flow in the nose: a model coupling flow and vasoerectile tissue distensibility. *Journal of Applied Physiology*, 98(1):288–295, 2005.
- [31] D. Frank, J. Kimbell, D. Cannon, and J. Rhee. Computed intranasal spray penetration: comparisons before and after nasal surgery. *Int Forum Allergy Rhinol*, 3(1):48–55, Jan 2013.
- [32] A. Gambaruto, D. Taylor, and D. Doorly. Modelling nasal airflow using a fourier descriptor representation of geometry. *International Journal for Numerical Methods in Fluids*, 59(11):1259–1283, 2009.
- [33] D. Gammack and P. E. Hydon. Flow in pipes with non-uniform curvature and torsion. *Journal of Fluid Mechanics*, 433:357–382, 2001.
- [34] S. Gane. What we don’t know about olfaction. Part 1: from nostril to receptor. *Rhinology*, 48:131–138, 2010.
- [35] Q. J. Ge, K. Inthavong, and J. Y. Tu. Local deposition fractions of ultrafine particles in a human nasal-sinus cavity cfd model. *Inhalation Toxicology*, 24(8): 492–505, 2012.
- [36] M. Germano. On the effect of torsion on a helical pipe flow. *Journal of Fluid Mechanics*, 125:1–8, 1982.
- [37] E. Ghahramani, O. Abouali, H. Emdad, and G. Ahmadi. Numerical analysis of stochastic dispersion of micro-particles in turbulent flows in a realistic model of human nasal/upper airway. *Journal of Aerosol Science*, 67:188–206, 2014.
- [38] M. Girardin, E. Bilgen, and P. Arbour. Experimental study of velocity fields in a human nasal fossa by laser anemometry. *The Annals of Otology, Rhinology, and Laryngology*, 92(3 Pt 1):231–236, 1982.

- [39] I. Hahn, P. Scherer, and M. Mozell. Velocity profiles measured for airflow through a large-scale model of the human nasal cavity. *Journal of Applied Physiology*, 75: 2273–2273, 1993.
- [40] A. Heenan, E. Matida, A. Pollard, and W. Finlay. Experimental measurements and computational modeling of the flow field in an idealized human oropharynx. *Exp. Fluids*, 35(1):70–84, 2003.
- [41] A. Heenan, E. Matida, A. Pollard, and W. Finlay. Experimental measurements and computational modeling of the flow field in an idealized human oropharynx. *Experiments in Fluids*, 35(1):70–84, 2003.
- [42] I. Hörschler, W. Schröder, and M. Meinke. On the assumption of steadiness of nasal cavity flow. *Journal of Biomechanics*, 43(6):1081–1085, 2010.
- [43] K. Inthavong, K. Zhang, and J. Tu. Numerical modelling of nanoparticle deposition in the nasal cavity and the tracheobronchial airway. *Computer Methods in Biomechanics and Biomedical Engineering*, 14(7):633–643, 2011.
- [44] S. Ishikawa, T. Nakayama, M. Watanabe, and T. Matsuzawa. Visualization of flow resistance in physiological nasal respiration: analysis of velocity and vorticities using numerical simulation. *Arch. Otolaryngol. Head Neck Surg.*, 132(11): 1203–1209, Nov 2006.
- [45] S. Ishikawa, T. Nakayama, M. Watanabe, and T. Matsuzawa. Flow mechanisms in the human olfactory groove: numerical simulation of nasal physiological respiration during inspiration, expiration, and sniffing. *Arch. Otolaryngol. Head Neck Surg.*, 135(2):156–162, Feb 2009.
- [46] J. Jeong and F. Hussain. On the identification of a vortex. *Journal of Fluid Mechanics*, 285:69–94, 1995.
- [47] A. Johnstone, M. Uddin, A. Pollard, A. Heenan, and W. Finlay. The flow inside an idealised form of the human extra-thoracic airway. *Exp. Fluids*, 37(5):673–689, 2004.
- [48] P. Karakosta, A. H. Alexopoulos, and C. Kiparissides. Computational model of particle deposition in the nasal cavity under steady and dynamic flow. *Computer Methods in Biomechanics and Biomedical Engineering*, 0(0):1–13, 2013.
- [49] J. Kasperbauer and E. Kern. Nasal valve physiology. implications in nasal surgery. *Otolaryngologic Clinics of North America*, 20(4):699–719, 1987.
- [50] T. Keck, R. Leiacker, A. Heinrich, S. Kühnemann, and G. Rettinger. Humidity and temperature profile in the nasal cavity. *Rhinology*, 38(4):167–171, 2000.

- [51] J. Kelly, A. Prasad, and A. Wexler. Detailed flow patterns in the nasal cavity. *Journal of Applied Physiology*, 89(1):323–337, 2000.
- [52] K. Keyhani, P. Scherer, and M. Mozell. Numerical simulation of airflow in the human nasal cavity. *Journal of Biomechanical Engineering*, 117(4):429–441, 1995.
- [53] K. Keyhani, P. Scherer, and M. Mozell. A numerical model of nasal odorant transport for the analysis of human olfaction. *Journal of Theoretical Biology*, 186(3):279–301, 1997.
- [54] J. Kimbell, D. Frank, P. Laud, G. Garcia, and J. Rhee. Changes in nasal airflow and heat transfer correlate with symptom improvement after surgery for nasal obstruction. *Journal of Biomechanics*, 46(15):2634–2643, 2013.
- [55] J. S. Kimbell, G. J. Garcia, D. O. Frank, D. E. Cannon, S. S. Pawar, and J. S. Rhee. Computed nasal resistance compared with patient-reported symptoms in surgically treated nasal airway passages: A preliminary report. *American Journal of Rhinology & Allergy*, 26(3):e94, 2012.
- [56] C. Kleinstreuer and Z. Zhang. Airflow and particle transport in the human respiratory system. *Annual Review of Fluid Mechanics*, 42:301–334, 2010.
- [57] A. V. Kolanjiyil and C. Kleinstreuer. Nanoparticle mass transfer from lung airways to systemic regions. Part II: Multi-compartmental modeling. *Journal of Biomechanical Engineering*, 135(12):121004, 2013.
- [58] A. V. Kolanjiyil and C. Kleinstreuer. Nanoparticle mass transfer from lung airways to systemic regions. Part I: Whole-lung aerosol dynamics. *Journal of Biomechanical Engineering*, 135(12):121003, 2013.
- [59] F. Krause, A. Wenk, C. Lacor, W. G. Kreyling, W. Möller, and S. Verbanck. Numerical and experimental study on the deposition of nanoparticles in an extrathoracic oral airway model. *Journal of Aerosol Science*, 57:131–143, 2013.
- [60] D. N. Ku. Blood flow in arteries. *Annual Review of Fluid Mechanics*, 29(1):399–434, 1997.
- [61] J.-H. Lee, Y. Na, S.-K. Kim, and S.-K. Chung. Unsteady flow characteristics through a human nasal airway. *Respiratory Physiology & Neurobiology*, 172(3):136–146, 2010.
- [62] H. Lewis, editor. *Gray’s Anatomy*. Lea & Febiger, 20th U.S. edition, 1918.
- [63] C. Lin, M. Tawhai, G. McLennan, and E. Hoffman. Characteristics of the turbulent laryngeal jet and its effect on airflow in the human intra-thoracic airways. *Respiratory physiology & neurobiology*, 157(2):295–309, 2007.

- [64] C.-L. Lin, M. H. Tawhai, G. McLennan, and E. A. Hoffman. Characteristics of the turbulent laryngeal jet and its effect on airflow in the human intra-thoracic airways. *Respiratory Physiology & Neurobiology*, 157(2):295–309, 2007.
- [65] P. Longest and M. J. Oldham. Numerical and experimental deposition of fine respiratory aerosols: development of a two-phase drift flux model with near-wall velocity corrections. *Journal of Aerosol Science*, 39(1):48–70, 2008.
- [66] P. Longest and S. Vinchurkar. Effects of mesh style and grid convergence on particle deposition in bifurcating airway models with comparisons to experimental data. *Medical Engineering & Physics*, 29(3):350–366, 2007.
- [67] P. Longest and J. Xi. Computational investigation of particle inertia effects on submicron aerosol deposition in the respiratory tract. *Journal of Aerosol Science*, 38(1):111–130, 2007.
- [68] P. W. Longest and J. Xi. Effectiveness of direct lagrangian tracking models for simulating nanoparticle deposition in the upper airways. *Aerosol Science and Technology*, 41(4):380–397, 2007.
- [69] S. H. Loring, M. Garcia-Jacques, and A. Malhotra. Pulmonary characteristics in copd and mechanisms of increased work of breathing. *Journal of Applied Physiology*, 107(1):309–314, 2009.
- [70] B. Ma and K. R. Lutchen. An anatomically based hybrid computational model of the human lung and its application to low frequency oscillatory mechanics. *Annals of Biomedical Engineering*, 34(11):1691–1704, 2006.
- [71] M. Malvè, A. P. del Palomar, S. Chandra, J. L. López-Villalobos, A. Mena, E. A. Finol, A. Ginel, and M. Doblaré. Fsi analysis of a healthy and a stenotic human trachea under impedance-based boundary conditions. *Journal of biomechanical engineering*, 133(2):021001, 2011.
- [72] J. Mancebo, D. Isabey, H. Lorino, F. Lofaso, F. Lemaire, and L. Brochard. Comparative effects of pressure support ventilation and intermittent positive pressure breathing (IPPB) in non-intubated healthy subjects. *European Respiratory Journal*, 8(11):1901–1909, 1995.
- [73] R. McRae, A. Jones, P. Young, and J. Hamilton. Resistance, humidity and temperature of the tracheal airway. *Clinical Otolaryngology & Allied Sciences*, 20(4):355–356, 1995.
- [74] G. Milic-Emili and J. M. Petit. Mechanical efficiency of breathing. *Journal of Applied Physiology*, 15:359–362, 1960.

- [75] O. Mimouni-Benabu, L. Meister, J. Giordano, P. Fayoux, N. Loundon, J. M. Triglia, and R. Nicollas. A preliminary study of computer assisted evaluation of congenital tracheal stenosis: A new tool for surgical decision-making. *International Journal of Pediatric Otorhinolaryngology*, 76(11):1552–1557, 2012.
- [76] G. Mylavaram, S. Murugappan, M. Mihaescu, M. Kalra, S. Khosla, and E. Gutmark. Validation of computational fluid dynamics methodology used for human upper airway flow simulations. *Journal of Biomechanics*, 42(10):1553–1559, 2009.
- [77] S. Naftali, M. Rosenfeld, M. Wolf, and D. Elad. The air-conditioning capacity of the human nose. *Annals of Biomedical Engineering*, 33(4):545–553, Apr 2005.
- [78] W. Nichols and M. O’Rourke. *McDonald’s Blood Flow in Arteries*. Hodder-Arnold, 5th edition, 2005.
- [79] L. Nicolaou and T. Zaki. Direct numerical simulations of flow in realistic mouth-throat geometries. *Journal of Aerosol Science*, 57:71–87, 2013.
- [80] F. Nicoud and F. Ducros. Subgrid-scale stress modelling based on the square of the velocity gradient tensor. *Flow, Turbulence and Combustion*, 62(3):183–200, 1999.
- [81] P. Nithiarasu, O. Hassan, K. Morgan, N. Weatherill, C. Fielder, H. Whittet, P. Ebdon, and K. Lewis. Steady flow through a realistic human upper airway geometry. *International Journal for Numerical Methods in Fluids*, 57(5):631–651, 2008.
- [82] Y. Ohtake, A. G. Belyaev, and I. A. Bogaevski. Polyhedral surface smoothing with simultaneous mesh regularization. In *Geometric Modeling and Processing 2000. Theory and Applications. Proceedings*, pages 229–237. IEEE, 2000.
- [83] E.-K. Pae, A. A. Lowe, K. Sasaki, C. Price, M. Tsuchiya, and J. A. Fleetham. A cephalometric and electromyographic study of upper airway structures in the upright and supine positions. *American Journal of Orthodontics and Dentofacial Orthopedics*, 106(1):52–59, 1994.
- [84] T. J. Pedley, R. C. Schroter, and M. F. Sudlow. The prediction of pressure drop and variation of resistance within the human bronchial airways. *Respiration Physiology*, 9(3):387–405, 1970.
- [85] T. J. Pedley, R. Schroter, and M. Sudlow. Gas flow and mixing in the airways. *Bioengineering Aspects of the Lung*, 3:163–265, 1977.
- [86] M. Peric. Flow simulation using control volumes of arbitrary polyhedral shape. *ERCRAFTAC bulletin*, 62:25–29, 2004.

- [87] M. Piccinelli, A. Veneziani, D. A. Steinman, A. Remuzzi, and L. Antiga. A framework for geometric analysis of vascular structures: application to cerebral aneurysms. *IEEE Transactions on Medical Imaging*, 28(8):1141–1155, 2009.
- [88] D. Poetker, J. Rhee, B. Mocan, and M. Michel. Computed tomography technique for evaluation of the nasal valve. *Archives of Facial Plastic Surgery*, 6(4):240–243, 2004.
- [89] A. Pollard, M. Uddin, A.-M. Shinneeb, and C. Ball. Recent advances and key challenges in investigations of the flow inside human oro-pharyngeal-laryngeal airway. *International Journal of Computational Fluid Dynamics*, 26(6-8):363–381, 2012.
- [90] S. Pope. *Turbulent Flows*. Cambridge University Press, 2000.
- [91] C. Rennie, K. Gouder, D. Taylor, N. Tolley, R. Schroter, and D. Doorly. Nasal inspiratory flow: at rest and sniffing. *International Forum of Allergy & Rhinology*, 1(2):128–135, 2011.
- [92] C. Rhie and W. Chow. Numerical study of the turbulent flow past an airfoil with trailing edge separation. *AIAA journal*, 21(11):1525–1532, 1983.
- [93] G. P. Russo. *Aerodynamic Measurements: From Physical Principles to Turnkey Instrumentation*. Woodhead Publishing, 2011.
- [94] S. Saddoughi and S. Veeravalli. Local isotropy in turbulent boundary layers at high reynolds number. *Journal of Fluid Mechanics*, 268:333–372, 1994.
- [95] P. Saksono, P. Nithiarasu, I. Sazonov, and S. Yeo. Computational flow studies in a subject-specific human upper airway using a one-equation turbulence model. influence of the nasal cavity. *International Journal for Numerical Methods in Engineering*, 87(1-5):96–114, 2011.
- [96] P. H. Saksono, P. Nithiarasu, and I. Sazonov. Numerical prediction of heat transfer patterns in a subject-specific human upper airway. *Journal of Heat Transfer*, 134(3):031022, 2012.
- [97] J. Sandeau, I. Katz, R. Fodil, B. Louis, G. Apiou-Sbirlea, G. Caillibotte, and D. Isabey. Cfd simulation of particle deposition in a reconstructed human oral extrathoracic airway for air and helium–oxygen mixtures. *Journal of aerosol science*, 41(3):281–294, 2010.
- [98] H. Schlichting. *Boundary-Layer Theory*. McGraw-Hill, 7th edition, 1979.
- [99] S. Schreck, K. Sullivan, C. Ho, and H. Chang. Correlations between flow resistance and geometry in a model of the human nose. *Journal of Applied Physiology*, 75: 1767–1767, 1993.

- [100] P. R. Sears, K. Thompson, M. R. Knowles, and C. W. Davis. Human airway ciliary dynamics. *American Journal of Physiology-Lung Cellular and Molecular Physiology*, 304(3):L170–L183, 2013.
- [101] R. Segal, G. Kepler, and J. Kimbell. Effects of differences in nasal anatomy on airflow distribution: a comparison of four individuals at rest. *Annals of Biomedical Engineering*, 36(11):1870–1882, 2008.
- [102] S. J. Sherwin and H. M. Blackburn. Three-dimensional instabilities and transition of steady and pulsatile axisymmetric stenotic flows. *Journal of Fluid Mechanics*, 533:297–327, 2005.
- [103] H. Shi, C. Kleinstreuer, and Z. Zhang. Laminar airflow and nanoparticle or vapor deposition in a human nasal cavity model. *J Biomech Eng*, 128(5):697–706, Oct 2006.
- [104] X. A. Si, J. Xi, J. Kim, Y. Zhou, and H. Zhong. Modeling of release position and ventilation effects on olfactory aerosol drug delivery. *Respiratory Physiology & Neurobiology*, 186(1):22–32, 2013.
- [105] J. R. Smitheran and T. J. Hixon. A clinical method for estimating laryngeal airway resistance during vowel production. *Journal of Speech and Hearing Disorders*, 46(2):138–146, 1981.
- [106] I. J. Sobey. Oscillatory flows at intermediate Strouhal number in asymmetric channels. *Journal of Fluid Mechanics*, 125:359–373, 1982.
- [107] C. Spence, N. Buchmann, and M. Jermy. Unsteady flow in the nasal cavity with high flow therapy measured by stereoscopic PIV. *Experiments in fluids*, 52(3):569–579, 2012.
- [108] M. T. Stang, M. J. Armstrong, J. B. Ogilvie, L. Yip, K. L. McCoy, C. N. Faber, and S. E. Carty. Positional dyspnea and tracheal compression as indications for goiter resection. *Archives of Surgery*, 147(7):621–626, 2012.
- [109] R. Subramaniam, R. Richardson, K. Morgan, J. Kimbell, and R. Guilmette. Computational fluid dynamics simulations of inspiratory airflow in the human nose and nasopharynx. *Inhalation Toxicology*, 10(2):91–120, 1998.
- [110] J. Tan, D. Han, J. Wang, T. Liu, T. Wang, H. Zang, Y. Li, and X. Wang. Numerical simulation of normal nasal cavity airflow in chinese adult: a computational flow dynamics model. *European Archives of Oto-Rhino-Laryngology*, 269(3):881–889, 2012.
- [111] G. Tanaka, T. Ogata, K. Oka, and K. Tanishita. Spatial and temporal variation of secondary flow during oscillatory flow in model human central airways. *Journal of Biomechanical Engineering*, 121(6):565–573, 1999.

- [112] Y. Tang and B. Guo. Computational fluid dynamics simulation of aerosol transport and deposition. *Frontiers of Environmental Science & Engineering in China*, 5(3):362–377, 2011.
- [113] G. Taubin. Curve and surface smoothing without shrinkage. In *Computer Vision, 1995. Proceedings., Fifth International Conference on*, pages 852–857. IEEE, 1995.
- [114] D. Taylor, D. Doorly, and R. Schroter. Inflow boundary profile prescription for numerical simulation of nasal airflow. *Journal of the Royal Society Interface*, 7(44):515–527, Mar 2010.
- [115] J. Tu, K. Inthavong, and G. Ahmadi. *Computational Fluid and Particle Dynamics in the Human Respiratory System*. Springer, 2012.
- [116] S. S. Varghese, S. H. Frankel, and P. F. Fischer. Direct numerical simulation of stenotic flows. part 1. steady flow. *Journal of Fluid Mechanics*, 582:253–280, 2007.
- [117] I. Weinhold and G. Mlynski. Numerical simulation of airflow in the human nose. *European Archives of Oto-Rhino-Laryngology and Head & Neck*, 261(8):452–455, 2004.
- [118] D. Wexler, R. Segal, and J. Kimbell. Aerodynamic effects of inferior turbinate reduction: computational fluid dynamics simulation. *Archives of Otolaryngology–Head & Neck Surgery*, 131(12):1102–1107, 2005.
- [119] J. Wheatley, T. Amis, L. Engel, et al. Nasal and oral airway pressure-flow relationships. *J Appl Physiol*, 71(6):2317–2324, 1991.
- [120] C. White. Streamline flow through curved pipes. *Proceedings of the Royal Society of London. Series A*, 123(792):645–663, 1929.
- [121] M. Wolf, S. Naftali, R. C. Schroter, and D. Elad. Air-conditioning characteristics of the human nose. *The Journal of Laryngology & Otology*, 118(02):87–92, 2004.
- [122] J. Xi and P. Longest. Numerical predictions of submicrometer aerosol deposition in the nasal cavity using a novel drift flux approach. *International Journal of Heat and Mass Transfer*, 51(23):5562–5577, 2008.
- [123] J. Xi and P. W. Longest. Characterization of submicrometer aerosol deposition in extrathoracic airways during nasal exhalation. *Aerosol Science and Technology*, 43(8):808–827, 2009.
- [124] G. Xiong, J. Zhan, K. Zuo, J. Li, L. Rong, and G. Xu. Numerical flow simulation in the post-endoscopic sinus surgery nasal cavity. *Medical & Biological Engineering & Computing*, 46(11):1161–1167, 2008.

- [125] C. Xu, S. Sin, J. M. McDonough, J. K. Udupa, A. Guez, R. Arens, and D. M. Wootton. Computational fluid dynamics modeling of the upper airway of children with obstructive sleep apnea syndrome in steady flow. *Journal of Biomechanics*, 39(11):2043–2054, 2006.
- [126] S. Zachow, P. Muigg, T. Hildebrandt, H. Doleisch, and H. Hege. Visual exploration of nasal airflow. *IEEE Trans Vis Comput Graph*, 15(6):1407–1414, 2009.
- [127] Z. Zhang and C. Kleinstreuer. Laminar-to-turbulent fluid–nanoparticle dynamics simulations: Model comparisons and nanoparticle-deposition applications. *International Journal for Numerical Methods in Biomedical Engineering*, 27(12):1930–1950, 2011.
- [128] K. Zhao and J. Jianj. What is normal nasal airflow? A computational study of 22 healthy adults. *International Forum of Allergy & Rhinology*, 4:435–446, 2014.
- [129] K. Zhao, P. W. Scherer, S. A. Hajiloo, and P. Dalton. Effect of anatomy on human nasal air flow and odorant transport patterns: implications for olfaction. *Chemical Senses*, 29(5):365–379, 2004.
- [130] K. Zhao, P. Dalton, G. Yang, and P. Scherer. Numerical modeling of turbulent and laminar airflow and odorant transport during sniffing in the human and rat nose. *Chemical Senses*, 31(2):107–118, 2006.
- [131] X. Zheng and Z. Silber-Li. The influence of Saffman lift force on nanoparticle concentration distribution near a wall. *Applied Physics Letters*, 95(12):124105–124105, 2009.
- [132] J. Zhu, H. Lee, K. Lim, S. Lee, and D. Wang. Evaluation and comparison of nasal airway flow patterns among three subjects from caucasian, chinese and indian ethnic groups using computational fluid dynamics simulation. *Respiratory Physiology & Neurobiology*, 175(1):62–69, 2011.

## A Geometric Values of Considered Airways

Plane	Area (mm <sup>2</sup> )	Perimeter (mm)	Hydraulic Diameter (mm)
1 (L - R)	122 - 100	50 - 49	9.7 - 8.2
2 (L - R)	108 - 92	44 - 44	9.8 - 8.3
3 (L - R)	91 - 91	72 - 75	5.0 - 4.9
4 (L - R)	188 - 144	171 - 162	4.4 - 3.5
5 (L - R)	171 - 130	154 - 154	4.4 - 3.4
6 (L - R)	187 - 175	53 - 62	14.1 - 11.2
7	215	60	14.4
8	57	31	7.5
9	171	54	12.6
10	143	51	11.2
11	204	53	15.5
12	198	52	15.2

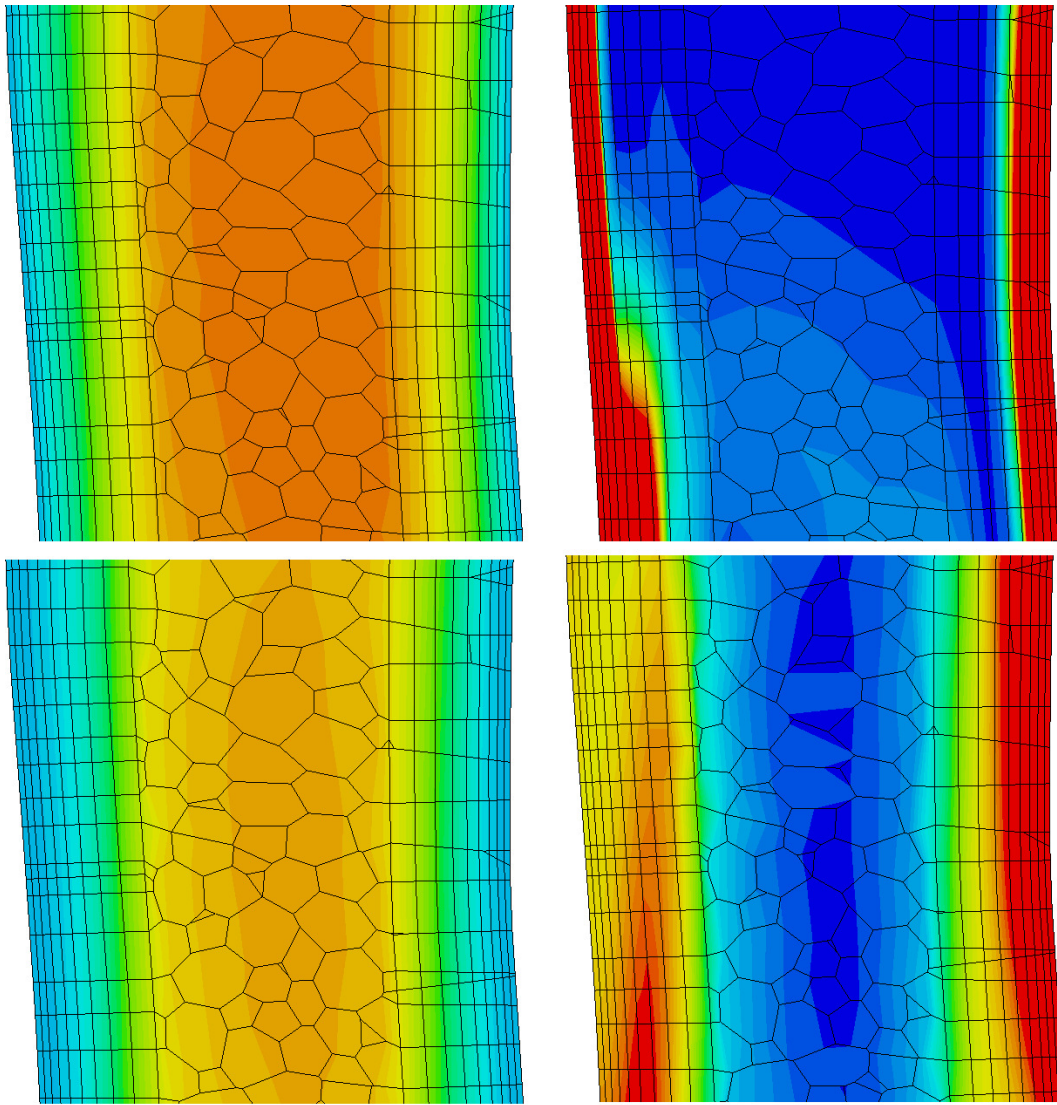
Table A.1: Geometric values for the planes defined in figure 4.2 for the large airway geometry described in section 4.1.

## B The Utilised Area Ratios of Analytic Flows

	Poiseuille	Turbulent Re=4000 [98]	Turbulent Re=23,000	De=50[23]	De=100	De=150	De=200
UA <sub>max</sub> /A	0.500	0.970	0.980	0.498	0.462	0.367	0.292
UA <sub>mean</sub> /A	0.500	0.568	0.571	0.499	0.489	0.451	0.419

Table B.1: Comparison of utilised area ratios for several analytical flow profiles.

## C Resolution of Scalar Boundary Layers



See figure caption for scales



Figure C.1: Section of the images shown in figure 5.16 with the outline of the mesh superimposed. Clockwise from top left  $\mathbf{u}\phi_C$  (scale -2 to 10),  $D\nabla\phi_C$  (scale 0 to  $1 \times 10^{-5}$ ),  $D\nabla\phi_D$  (scale 0 to 0.05) and  $\mathbf{u}\phi_D$  (scale -2 to 10). The section is taken between the inferior turbinate and the septum on plane 4 (figure 4.2) and covers the region from which the data for figure 5.20 is taken.